UNIVERSITÉ CATHOLIQUE DE LOUVAIN
ICTEAM ELECTRICAL ENGINEERING

Experimental Channel Characterization for Vehicle-to-Vehicle Communication Systems

PAR

Olivier RENAUDIN

THÈSE PRÉSENTÉE EN VUE DE L'OBTENTION DU GRADE DE DOCTEUR EN SCIENCES DE L'INGÉNIEUR

Composition du Jury

1. Claude Oestges (UCL)	Promoteur
2. Luc Vandendorpe (UCL)	Co-promoteur
3. Danielle Vanhoenacker (UCL)	Présidente du jury
4. Jérôme Louveaux (UCL)	Secrétaire
5. Philippe De Doncker (ULB)	
6. Christoph Mecklenbräucker (TU Wien)	
7. Katsuyuki Haneda (Aalto University)	

Abstract

In inter-vehicular environments, the scattering environment can change very rapidly, due to *(i):* the mobility of the vehicles, *(ii):* the relatively low height of the antennas (with no elevated base stations) and *(iii):* the potentially large number of scatterers located in the environment surrounding the Transmitter (Tx) and Receiver (Rx) vehicles.

As a result, the underlying fading process is intrinsically time-, frequency- and space-varying, i.e. its statistical properties do remain constant only over short (bounded) time, frequency and angular intervals, respectively. In other words, inter-vehicular radio propagation channels are significantly different from the (already well-known) ones of other wireless cellular networks, such that dedicated measurement campaigns and realistic radio propagation channel models are required in order to exploit fully all their potentialities.

The main contributions and findings of this thesis can be summarized as follows:

- Two measurement campaigns of Vehicle-to-Vehicle (V2V) radio propagation channels were carried out in collaboration with Aalto University (Helsinki, Finland). For that purpose, Multiple-Input Multiple-Output (MIMO) communication systems (with dimensions $N_\mathrm{r} \times N_\mathrm{t} = 30 \times 30$ and $N_\mathrm{r} \times N_\mathrm{t} = 30 \times 4$, respectively) were extensively investigated at a carrier frequency of 5.3 GHz, in several environments and scenarios very specific to Intelligent Transportation Systems (ITS),

- The validity of both the Wide-Sense Stationarity (WSS) and Uncorrelated Scattering (US) assumptions is assessed by means of the Correlation Matrix Distance (CMD), in order to characterize the amount of change (over time and frequency, respectively) in the spatial structure of either narrowband or wideband MIMO radio propagation channels. Typical stationarity distances and frequency bandwidths are in both cases approximately 10 to 40 m long and 40 to 50 MHz wide, respectively, depending on the variability and richness of the scattering environment that is surrounding the Tx and Rx vehicles. In other words, the non-stationary behavior of vehicular radio propagation channels is much more critical in over time than over frequency.

- The non-stationary fading statistics of vehicular radio propagation channels are characterized stochastically, over the so-identified stationarity intervals (for the first time in the literature, to the author's best knowledge). The time- and space-dependent behavior of the Ricean K-factor

and the Root-Mean Square (RMS) delay spread is strongly related to changes in the richness of the surrounding scattering environment as well as on the presence (or not) of a strong Line-of-Sight (LoS) component between the Tx and Rx vehicles,

- A vehicular Geometry-based Stochastic Channel Model (GSCM) is proposed. Such an approach is indeed particularly well-suited for the modeling of non-stationary radio propagation channels since each discrete scatterer is defined and characterized separately: the radio wave propagation is in that case modeled with very simplified ray-tracing methods and the scattering aspects with a classical fading model. A purely stochastic description of the diffuse scattering is also included in the GSCM. The proposed GSCM is completely parameterized and validated for Single-Input Single-Output (SISO) systems.

Keywords: Radio wave propagation, MIMO channel measurements, MIMO channel modeling, Non-stationarity, Channel characterization, GSCM.

Contents

List of Figures

List of Tables

List of Acronyms

AGC	Automatic Gain Control
AoA	Angle-of-Arrival
AoD	Angle-of-Departure
APS	Angular Power Spectrum
BER	Bit Error Rate
CDF	Cumulative Density Function
CMD	Correlation Matrix Distance
DSRC	Dedicated Short Range Communication
FRS	Family Radio Service
GSCM	Geometry-based Stochastic Channel Model
GSM	Global System for Mobile Communications
H	Homogeneous
IR	Impulse Response
ITS	Intelligent Transportation Systems
ITU	International Telecommunication Union
LCR	Level Crossing Rate
LSF	Local Scattering Function
LoS	Line-of-Sight
MSE	Mean Square Error
MIMO	Multiple-Input Multiple-Output
NLoS	Non-Line-of-Sight
OFDM	Orthogonal Frequency Division Multiplexing
PDF	Probability Density Function

PDP	Power-Delay Profile
PN	Pseudo-Noise
PSD	Power-Spectral Density
RF	Radio-Frequency
Rx	Receiver
RMS	Root Mean Square
RMSE	Root Mean Square Error
SISO	Single-Input Single-Output
SIMO	Single-Input Multiple-Output
SNR	Signal to Noise Ratio
TDL	Tapped-Delay Line
TF	Transfer Function
Tx	Transmitter
ULA	Uniform Linear Array
US	Uncorrelated Scattering
V2V	Vehicle-to-Vehicle
WAVE	Wireless Access in Vehicular Environments
WLAN	Wireless Local Area Network
WSS	Wide Sense Stationarity

CHAPTER 1

Introduction to non-stationary radio propagation channels

In recent years, mobility has become more and more crucial in our society. The number of vehicles driving on the roads has indeed exploded all over the world, either for domestic and social usage or freight transport. Unfortunately, this need in mobility has also some negative sides, which can be either

- Societal, since it has brought an increase of deaths and injuries in road accidents [1]. In 2004, the number of road deaths was hence estimated to more than 3000 every day around the world. On current trends and if nothing changes, the total number of deaths and injuries in road accidents worldwide is expected to grow by approximately 65% (and up to 80% in low- and medium-income countries),

- Ecological, since abrupt car driving and traffic congestions have led to a significant increase of fuel consumption and $\mathrm{CO_2}$ emissions [2]. In 2010, road transport was responsible for 17% of worldwide $\mathrm{CO_2}$ emissions from fuel combustion (22.7% for OCDE countries) and 15% of overall greenhouse gas emissions. Light-duty (passenger) vehicles account for up to 65% to 70% of the overall road sector $\mathrm{CO_2}$ emissions, which are forecast to rise by approximately 40% within 2030.

Hence, simultaneous efforts at the social, economical and technological levels have to be considered so as to address these challenges.

One possible solution consists in the development of Vehicle-to-Vehicle (V2V) wireless communication systems as an important part of more global architectures dedicated to Intelligent Transportation Systems (ITS). Each vehicle would then act as a node in a peer-to-peer distributed network, exchanging warning notifications (regarding traffic conditions, road accidents ahead, the passing of vehicles with high priority as firetrucks or ambulances, etc.) or driving assistance (e.g. for collision avoidance, wrong-way driving, lane changing, etc.) in order to make the driving experience safer and more efficient (and hence more friendly) for the users. Such active road safety applications require highly reliable transmission of data within short bounded delay intervals (i.e. with no retransmission of lost or corrupted data), at low data rates. Besides these road safety applications, vehicular wireless communication systems are also intended to support more commercial ones, dedicated to entertainment (e.g. social networking, movie or music streaming, multimedia services, etc.) or services (e.g. automatic payment, map updating, etc.), which would require higher data rates.

For that purpose, car manufacturers, road and infrastructure operators are collaborating since 2006 to the development of the Wireless Access in Vehicular Environments (WAVE) initiative, which aims at providing a reliable low-latency vehicular connectivity for ITS. For that purpose, an international standard, IEEE 802.11p [3], has been developed for vehicular communication systems and has gained an increasing importance all over the world (e.g. in North America [4], in Europe [5, 6, 7], in Japan [8], etc.). This standard is based on the well-known WiFi technology and operates in the 5.9 GHz band.

The development and the deployment of a reliable vehicular wireless communication system require a deep understanding of the underlying radio propagation channels. However, they differ significantly from those of other cellular wireless networks, which have already been widely explored in the literature, as they are intrinsically strongly time-varying (and therefore non-stationary). Such differences can be explained by *(i):* the mobility of the Transmitter (Tx) and Receiver (Rx) vehicles with possible high velocities, *(ii):* the relatively low height positions of the Tx and Rx antennas (with no base station) and *(iii):* the potentially large number of scatterers located in the environment surrounding the Tx and Rx vehicles. As a consequence, dedicated measurement campaigns as well as realistic radio propagation channel models are required in order to deeply understand vehicular radio propagation channels and to exploit all their potentialities. These different tasks have been addressed since 2006 in a large number of papers, stemming from several research groups, and have already been the object of various surveys [9, 10].

The remainder of this Chapter is structured as follows: Section 1.1 describes the radio wave propagation occuring in Multiple-Input Multiple-Output (MIMO) radio propagation channels. Section 1.2 introduces the concept of non-stationarity of the radio propagation channel and different metrics for its characterization in MIMO radio propagation channels. Section 1.3 provides a review of different possible approaches for the modeling of radio propagation channels. Section 1.4 is dedicated to the experimental characterization of inter-vehicular radio propagation channels. Finally, Section 1.5 presents the outline of the thesis and my contributions.

1.1 MIMO radio propagation channels

1.1.1 Multipath propagation aspects

In any wireless communication network, the radio propagation channel is the medium through which a signal is transmitted from the Tx to the Rx side. At the Tx side, electromagnetic waves are emitted in multiple directions. Each wave interacts differently with the surrounding environment, via various physical propagation phenomena. These interactions are assumed to occur only in the far-field of the antennas, such that the transmitted waves can be assumed as being planar and described using ray-optical approximations. The possible interactions consist in specular reflections, waveguiding, diffraction, scattering, absorption or any combination between these [11]. Hence, multiple realizations of the transmitted signal can be observed at the Rx side, with individual amplitudes, propagation delays, directional characteristics, etc.

For a given Tx-Rx antenna link, the instantaneous Impulse Response (IR) of the radio propagation channel is the linear coherent superposition of all these multipath components. This superposition can be either constructive or destructive (as the phase of the multipath components is random), hence yielding fading, and may significantly deteriorate the quality of the received signal. All the frequencies of the transmitted signal being affected by different multipath components, the fading is said to be frequency selective. Moreover, the radio propagation channel varies over time, owing to the possible motion of the Tx, the Rx and the scatterers (especially in vehicular environments). Each multipath component undergoes a different Doppler frequency shift, and the radio propagation channel is said to be time selective.

The Single-Input Single-Output (SISO) radio propagation channel, with a single antenna at the Tx and Rx sides, is completely described by its IR $h(\tau\,;\,t)$, which relates the input signal $x(t)$ at the Tx side and the output signal $y(t)$ at the Rx side through the convolution operation

$$y(t) = h(\tau\,;\,t) * x(t) + n(t), \tag{1.1}$$

where $n(t)$ denotes additive noise at the Rx side. Fig. 1.1 shows an example of measured time-frequency selective IRs.

1.1.2 Narrowband radio propagation channels

For a narrowband radio propagation channel (i.e. when the system has a small bandwidth, such that all the multipath components arrive at the Rx side within

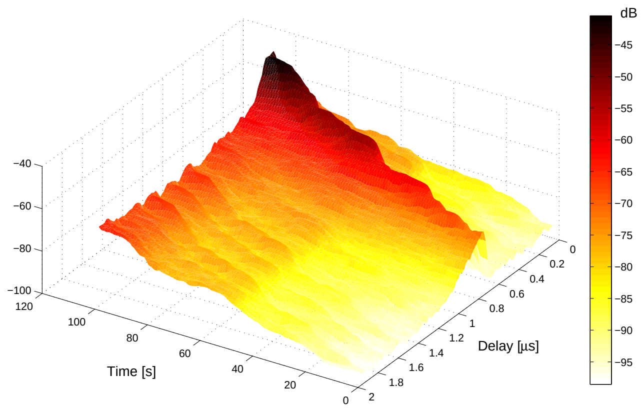

Figure 1.1: Example of measured time-variant IRs.

a single delay tap), the radio propagation channel can be modeled as

$$h = \underbrace{G_0^{1/2}\left(\frac{d}{d_0}\right)^{-n/2}}_{1.} \underbrace{S_{\mathrm{LS}}}_{2.} \underbrace{s_{\mathrm{SS}}}_{3.}, \tag{1.2}$$

where each of these three processes characterizes a different propagation phenomenon, namely

1. Pathloss, which describes the deterministic and (monotonic) decay of the received power as the distance d between the Tx and the Rx increases. It is usually parameterized by an attenuation coefficient, whose value depends on the investigated environment.

   Pathloss exponents around 1.8 - 1.9 were reported on highways with light trafic conditions [12, 13, 14] and in rural environments [14]. These values show good agreement with the two-ray (waveguiding) model, i.e. with a ground reflection, [14, 15].

   In sub-urban environments, a break point model was found to be suitable, with pathloss exponents of 2.3 - 2.7 up to a distance of 100 m, and around 3.8 - 4 beyond that distance [16]. In urban environments, pathloss exponents of 1.6 - 1.9 were typically measured [14, 15, 17],

2. Large-scale fading, which describes the fluctuations of the radio propagation channel gain over large distances, typically hundreds of wavelengths, due to the presence of large obstacles shadowing the propagation of multipath components.

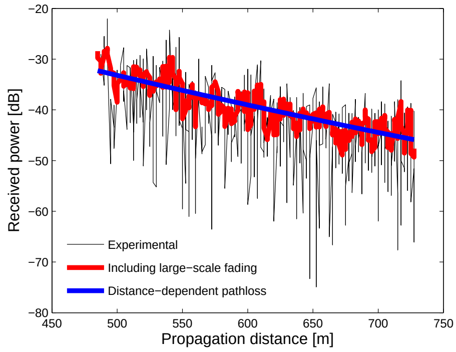

Figure 1.2: Variations of the received power level in a highway scenario. The distance decay and the low-pass filtered signal are also provided.

It is usually modeled as a lognormal random variable, which accounts for the large-scale variations of the received power around the pathloss curve, with Probability Density Function (PDF) given by

$$f(x\,;\,\mu_{\mathrm{LS}},\sigma_{\mathrm{LS}}) = \frac{1}{\sqrt{2\pi}\sigma_{\mathrm{LS}}x} e^{-\frac{(\ln x-\mu_{\mathrm{LS}})^2}{2\sigma_{\mathrm{LS}}^2}}, \tag{1.3}$$

where μ_{LS} and σ_{LS}^2 are the mean and variance of the corresponding normal random variable, respectively. Moreover, the large-scale fading is usally correlated, with autocorrelation function decaying exponentially with the distance.

The variance is usually found to be relatively low whatever the environment, with typical values around 1.5 - 3.3 dB in Line-of-Sight (LoS) conditions [13, 14, 15] and around 6.1 - 6.7 dB in non-LoS conditions [18]. Typical decorrelation distances of approximately 5 m are reported in urban environments and of 23 m (resp. 32 m) on highways in LoS (resp. non-LoS) conditions [18],

3. Small-scale fading, which describes the fluctuations of the radio propagation channel gain over short distances, typically a few wavelengths, due to constructive or destructive interferences between the multipath components at the Rx side. Assuming a large number of isotropic multipath components, the central limit theorem yields that the small-scale fading is a zero-mean complex-normal random variable with variance

σ_{ss}^2. Its envelope thus follows a Rayleigh distribution with PDF

$$f(x\,;\,\sigma_{\text{ss}}) = \frac{x}{\sigma_{\text{ss}}^2} e^{-\frac{x^2}{2\sigma_{\text{ss}}^2}}, \quad x \geq 0. \tag{1.4}$$

Note that $\sigma_{\text{ss}}^2 = 0.5$ when the small-scale fading has unit average power. If now a strong coherent (non-fading) component dominates the others, then the small-scale fading has non-zero mean complex-normal samples and its envelope follows a Rice distribution with PDF given by

$$f(x\,;\,\sigma_{\text{ss}}, K) = \frac{x}{\sigma_{\text{ss}}^2} e^{-\left(K+\frac{x^2}{2\sigma_{\text{ss}}^2}\right)} I_0\left(\frac{\sqrt{2K}}{\sigma_{\text{ss}}} x\right), \quad x \geq 0. \tag{1.5}$$

where the K-factor describes the ratio between the average power of the specular and the diffuse components of the signal. Note that $2\sigma_{\text{ss}}^2 = 1/(K+1)$ when the small-scale fading has unit power. A Ricean K-factor close to 0 indicates strong fading conditions (i.e. it reduces to the Rayleigh case), while larger values imply less fading variations. Though the Ricean distribution is often associated with the presence of a LoS component [19], it can also arise in presence of a strong coherent specular reflection, e.g. on a static scatterer located in the vincinity of the Tx or Rx vehicles [11].

Alternatively, the envelope of the small-scale fading can be described by the flexible Weibull distribution, with PDF given by

$$f(x\,;\,\alpha, \beta) = \frac{\beta}{\alpha}\left(\frac{x}{\alpha}\right)^{\beta-1} e^{-\left(\frac{x}{\alpha}\right)^{\beta}}, \quad x \geq 0, \tag{1.6}$$

where α and β are the scale and shape parameters of the Weibull distribution, respectively. Note that $\alpha = 1/\sqrt{\Gamma\left(1+2/\beta\right)}$ when the small-scale fading has unit power, where $\Gamma\left(\cdot\right)$ denotes the Gamma function. The shape parameter β is often used as an indicator of the fading severity: $\beta = 2$ yields indeed the Rayleigh distribution, while $\beta < 2$ denotes “worse than Rayleigh” fading [20, 21, 22]. However, although the Weibull distribution is mathematically tractable for analytical investigations, it cannot be related to any physical interpretation (unlike the Rayleigh and Ricean distributions).

Note that the model in Eq. (1.2) inherently includes not only the radio propagation channel but also the influence of the Tx and Rx antenna patterns and of the corresponding Radio-Frequency (RF) cables, as shown in Fig. 1.3. Hence, this model is very specific to the antenna arrays that have been used to parameterize the model.

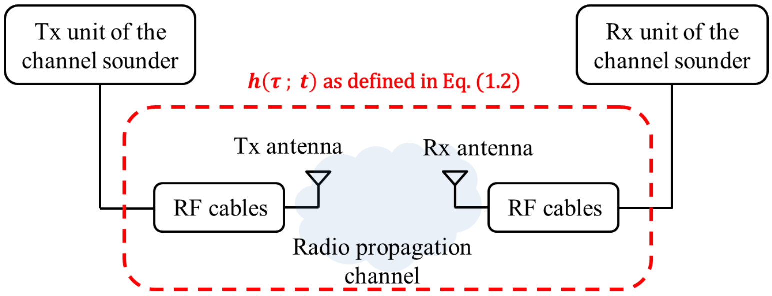

Figure 1.3: Block diagram of the measurement system, including the definition of the radio propagation channel as defined in Eq. (1.2).

1.1.3 Multidimensional radio propagation channels

Double-directional SISO radio propagation channels

In a three-dimensional environment, the directional IR of the radio propagation channel can be expressed as the linear (coherent) time-variant superposition of L multipath components, such that [11, 23, 24]

$$h(\tau\,;\,t\,;\,\mathbf{\Omega}_{\mathrm{Tx}}\,;\,\mathbf{\Omega}_{\mathrm{Rx}}) = \sum_{l=0}^{L-1} e^{j2\pi\nu_l t}\; g_{\mathrm{Rx}}(\mathbf{\Omega}_{\mathrm{Rx},l})\; a_l\; g_{\mathrm{Tx}}(\mathbf{\Omega}_{\mathrm{Tx},l})\; \delta(\tau-\tau_l), \quad (1.7)$$

where τ_l, a_l, ν_l and $\mathbf{\Omega}_{\mathrm{Tx},l}$ and $\mathbf{\Omega}_{\mathrm{Rx},l}$ denote the time-variant delay, complex amplitude, Doppler shift, Angle-of-Departure (AoD) and Angle-of-Arrival (AoA) of the l^{th} multipath component, respectively. The AoD is determined by the azimuth angle $\phi_{\mathrm{Tx},l}$ and the elevation angle $\theta_{\mathrm{Tx},l}$ (the AoA being defined in a similar manner). Moreover, $g_{\mathrm{Tx}}(\mathbf{\Omega}_{\mathrm{Tx},l})$ and $g_{\mathrm{Rx}}(\mathbf{\Omega}_{\mathrm{Rx},l})$ are the complex field patterns of the Tx and Rx antennas in the directions $\mathbf{\Omega}_{\mathrm{Tx},l}$ and $\mathbf{\Omega}_{\mathrm{Rx},l}$, respectively. Hence, the amplitude a_l of the l^{th} multipath component does not depend on the kind of antenna arrays that are used at both link ends. Moreover, the total number L of multipath components can vary over time, as some interactions may appear or disappear owing to the motion of the Tx, Rx or scatterers.

If now linearly dual-polarized antennas are used at both the Tx and Rx sides (which consist of two elements with orthogonal polarizations, e.g. vertical and horizontal, so that low inter-antenna correlation can be achieved), then

Eq. (1.7) can be rewritten as

$$h(\tau\,;\,t\,;\,\mathbf{\Omega}_{\mathrm{Tx}}\,;\,\mathbf{\Omega}_{\mathrm{Rx}}) = \sum_{l=0}^{L-1} e^{j2\pi\nu_l t}\; g_{\mathrm{Rx}}(\mathbf{\Omega}_{\mathrm{Rx},l}) \times \begin{bmatrix} a_{l,vv} & a_{l,vh} \\ a_{l,hv} & a_{l,hh} \end{bmatrix} g_{\mathrm{Tx}}(\mathbf{\Omega}_{\mathrm{Tx},l})\;\delta(\tau-\tau_l), \qquad (1.8)$$

where each multipath component is now associated with a polarization-rotation matrix, which encompasses its amplitude for each pair of Tx-Rx polarization (the subscripts v and h denoting the vertical and horizontal polarizations, respectively). This scattering matrix indicates how much the polarization of the transmitted signal is rotated after it has interacted with the scatterer, i.e.

- $a_{l,vv}$ corresponds to the complex amplitude of the l^{th} multipath component that is experienced by a signal transmitted with a vertical polarization and received with a vertical polarization,

- $a_{l,vh}$ corresponds to the complex amplitude of the l^{th} multipath component that is experienced by a signal transmitted with a horizontal polarization and received with a vertical polarization,

- $a_{l,hv}$ corresponds to the complex amplitude of the l^{th} multipath component that is experienced by a signal transmitted with a vertical polarization and received with a horizontal polarization,

- $a_{l,hh}$ corresponds to the complex amplitude of the l^{th} multipath component that is experienced by a signal transmitted with a horizontal polarization and received with a horizontal polarization.

Multidimensional modeling

The double-directional IR is a function of four different parameters, namely time, delay, AoD and AoA. The radio propagation channel can equivalently be described by several other functions, which are all related one to another through Fourier transforms between

$$\begin{array}{rccll} \text{Time:} & t & \xrightarrow{\mathcal{F}} & \text{Doppler frequency:} & \nu \\ \text{Delay:} & \tau & \xrightarrow{\mathcal{F}} & \text{Frequency:} & f \\ \text{DoD-DoA:} & \mathbf{\Omega}_{\mathrm{Tx/Rx}} & \xrightarrow{\mathcal{F}} & \text{Space:} & \mathbf{l}_{\mathrm{Tx/Rx}} \end{array}$$

where $\mathbf{l}_{\text{Tx/Rx}}$ denotes the vectorized spatial domain (in terms of azimuth and elevation) at the Tx and Rx sides. The so-generated multidimensional functions are all stochastic, owing to the constructive and destructive interferences of the received multipath components. These functions were first introduced as parts of a system for the characterization of wideband time-varying linear radio propagation channels by Bello in his seminal paper [25]. These Bello's system functions were then generalized to the case of double-directional radio propagation channels [11, 26]. These functions are all related one to another through Fourier transforms, so that the knowledge of at least one of them is sufficient for the complete characterization of the double-directional radio propagation channel. For example, the time-varying Tx-Rx angular-resolved Transfer Function (TF) can be expressed as

$$G(f;\, t\,;\, \mathbf{\Omega}_{\text{Tx}}\,;\, \mathbf{\Omega}_{\text{Rx}}) = \text{TF}_{\tau\to f}\left\{h(\tau\,;\, t\,;\, \mathbf{\Omega}_{\text{Tx}}\,;\, \mathbf{\Omega}_{\text{Rx}})\right\}. \tag{1.9}$$

Similarly, $S(\tau\,;\, \nu\,;\, \mathbf{\Omega}_{\text{Tx}}\,;\, \mathbf{\Omega}_{\text{Rx}})$ denotes the Doppler-varying Tx-Rx angular-resolved IR, which can be obtained by taking the one-dimensional Fourier transform of $h(\tau\,;\, t\,;\, \mathbf{\Omega}_{\text{Tx}}\,;\, \mathbf{\Omega}_{\text{Rx}})$ in the time domain.

However, these Bello's system functions can practically not be described statistically, since it would require the exact knowledge (or, at least, an accurate estimate) of their joint multidimensional PDFs. It is indeed unrealistic, given the large number of parameters on which they depend. As a consequence, an often used approximation of these generalized Bello's system functions can be obtained by means of their second order statistics, namely their autocorrelation functions (assuming that they are zero-mean) [11, 25, 26]. For example, the time-varying delay- and Tx-Rx angular-resolved correlation functions can be expressed as

$$\begin{aligned} &R(\tau, \tau'\,;\, t, t'\,; \mathbf{\Omega}_{\text{Tx}}, \mathbf{\Omega}'_{\text{Tx}}\,;\, \mathbf{\Omega}_{\text{Rx}}, \mathbf{\Omega}'_{\text{Rx}}) = \\ &\qquad E\left\{h(\tau\,;\, t\,;\, \mathbf{\Omega}_{\text{Tx}}\,;\, \mathbf{\Omega}_{\text{Rx}})h^*(\tau'\,;\, t'\,;\, \mathbf{\Omega}'_{\text{Tx}}\,;\, \mathbf{\Omega}'_{\text{Rx}})\right\}. \end{aligned} \tag{1.10}$$

These multidimensional correlation functions are all related one to another through double Fourier transforms. As a result, the knowledge of one of these system correlation functions is sufficient for the complete characterization of the double-directional radio propagation channel.

Wide-sense stationarity uncorrelated scattering homogeneity

These multidimensional correlation functions are in practice still very complex to handle. Hence, further simplifications are needed in order to provide simpler models for the correlation functions, e.g. [27]

- The Wide Sense Stationarity (WSS) assumption, stating that the first and second order statistics of the radio propagation channel do not change over time. Hence, its mean is constant, while the time correlation only depends on the time difference $t - t'$. Equivalently, in the frequency domain, multipath components undergoing different Doppler shifts are uncorrelated,

- The Uncorrelated Scattering (US) assumption, stating that the first and second order statistics of the radio propagation channel do not change over frequency. Hence, the frequency correlation only depends on the frequency difference $\Delta f = f' - f$. Equivalently, in the delay domain, multipath components arriving with different delays are uncorrelated,

- The Homogeneous (H) assumption, stating that the first and second order statistics of the radio propagation channel do not change over space at the Tx and Rx sides. Hence, the antenna correlation only depends on the differences in the spatial domain $\Delta l_{\text{Tx/Rx}} = l'_{\text{Tx/Rx}} - l_{\text{Tx/Rx}}$. Equivalently, in the angular domain, multipath components with different AoDs and AoAs are uncorrelated.

The radio propagation channel is therefore said to be WSS-US-H when the three aforementioned assumptions are simultaneously fulfilled. The Doppler-varying delay- and Tx-Rx angular-resolved correlation function of the radio propagation channel is therefore white in all dimensions, such that Eq. (1.10) can be rewritten as

$$\begin{aligned} &R(\tau,\tau' \,;\, \nu,\nu' \,;\, \mathbf{\Omega}_{\text{Tx}},\mathbf{\Omega}'_{\text{Tx}} \,;\, \mathbf{\Omega}_{\text{Rx}},\mathbf{\Omega}'_{\text{Rx}}) = \\ &\qquad R(\Delta\tau \,;\, \Delta\nu \,;\, \Delta\mathbf{\Omega}_{\text{Tx}} \,;\, \Delta\mathbf{\Omega}_{\text{Rx}})\delta(\Delta\tau)\delta(\Delta\nu)\delta(\Delta\mathbf{\Omega}_{\text{Tx}})\delta(\Delta\mathbf{\Omega}_{\text{Rx}}). \end{aligned} \tag{1.11}$$

In other words, the statistics of the radio propagation channel do not change over neither time, nor frequency, nor space.

Time, frequency and space selectivity

The dispersion of the multipath components over time, frequency and space can affect significantly the performances of wireless communication systems. When the WSS-US-H assumption is fulfilled, different metrics have been introduced in order to quantify the frequency, space and time selectivities of the radio propagation channel, namely

- The Root Mean Square (RMS) Doppler spread, as a measure for the time selectivity of the radio propagation channel. Introducing the narrowband

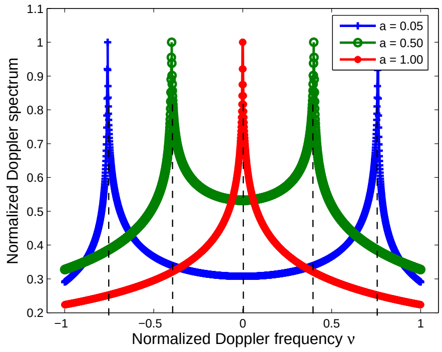

Figure 1.4: Normalized Doppler spectra in vehicular environments, with $\nu_{\mathrm{Rx}} = 0.8$ and $\nu_{\mathrm{Tx}} = a\nu_{\mathrm{Rx}}$. The peaks are found for the Doppler frequencies $\pm(\nu_{\mathrm{Rx}} - \nu_{\mathrm{Tx}})$, respectively.

Doppler Power-Spectral Density (PSD)

$$\mathcal{P}(\nu) = E\left\{ \left| \iiint S(\tau\,;\,\nu\,;\,\boldsymbol{\Omega}_{\mathrm{Tx}}\,;\,\boldsymbol{\Omega}_{\mathrm{Rx}}) d\tau d\boldsymbol{\Omega}_{\mathrm{Tx}} d\boldsymbol{\Omega}_{\mathrm{Rx}} \right|^2 \right\}, \quad (1.12)$$

the mean Doppler frequency $\overline{\nu}$ and RMS Doppler frequency spread ν_{rms} are then defined as [28]

$$\overline{\nu} = \frac{\int \nu \mathcal{P}(\nu) d\nu}{\int \mathcal{P}(\nu) d\nu}, \quad (1.13)$$

$$\nu_{\mathrm{rms}} = \sqrt{\frac{\int (\nu - \overline{\nu})^2 \mathcal{P}(\nu) d\nu}{\int \mathcal{P}(\nu) d\nu}}. \quad (1.14)$$

Fig. 1.4 shows typical Doppler spectra for V2V radio propagation channels, when two-dimensional isotropic scattering is considered. They exhibit peaks at frequencies $\pm f_c(v_{\mathrm{Rx}} - v_{\mathrm{Tx}})/c$, where f_c, v_{Tx} (resp. v_{Rx}) and c are the carrier frequency, the Tx (resp. Rx) velocity and the speed of light, respectively [29, 30, 31]. Note that the well-known Jake's spectrum is included as a special case, when the Tx velocity is set to zero.

RMS Doppler spreads measured in V2V environments are significantly larger (up to four times [10]) than those measured in other cellular radio propagation channels, owing to the high mobility of the Tx, Rx and scatterers. This is especially true on highways and in rural environments, which exhibit large values around 100 Hz [19, 14], but also with possible values up to 760 - 1000 Hz [32]. Smaller values are reported in urban environments, typically between 30 and 90 Hz [19, 14], with maximum values up to 260 - 340 Hz [32]. The average RMS Doppler spread was found to increase linearly with the effective speed $(v_{\text{Tx}}^2 + v_{\text{Rx}}^2)^{1/2}$ [16],

- The RMS delay spread, as a measure of the frequency selectivity of the radio propagation channel. Introducing the Power-Delay Profile (PDP)

$$\mathcal{P}(\tau) = E\left\{\left|\iiint h(\tau\,;\,t\,;\,\mathbf{\Omega}_{\text{Tx}}\,;\,\mathbf{\Omega}_{\text{Rx}})dtd\mathbf{\Omega}_{\text{Tx}}d\mathbf{\Omega}_{\text{Rx}}\right|^2\right\}, \tag{1.15}$$

the mean delay $\overline{\tau}$ and RMS delay spread τ_{rms} are then defined as [28]

$$\overline{\tau} = \frac{\int \tau\mathcal{P}(\tau)d\tau}{\int \mathcal{P}(\tau)d\tau}, \tag{1.16}$$

$$\tau_{\text{rms}} = \sqrt{\frac{\int (\tau - \overline{\tau})^2\,\mathcal{P}(\tau)d\tau}{\int \mathcal{P}(\tau)d\tau}}. \tag{1.17}$$

The RMS delay spread has been extensively investigated in a number of inter-vehicular measurement campaigns. Both rural and sub-urban environments usually exhibit the smallest RMS delay spreads, with average values typically around 20 - 50 ns [14, 32]. Significantly higher values can be observed on highways, between 40 and 400 ns [13, 14, 32, 33] depending on the traffic conditions and increases with the traffic density [33]. On the other hand, urban environments provide similar values in the range of 120 - 370 ns [32, 33], although 50 ns was measured in [14]. The large fluctuations in these measured RMS delay spread values are due to the fact that they strongly depend on the nature of the scattering environment around the Tx and Rx vehicles (e.g. with the presence, or not, of far away strong scatterers),

- The RMS angular spread, as a measure of the spatial selectivity of the radio propagation channel. Introducing, for example, the Angular Power Spectrum (APS) at the Tx side

$$\mathcal{P}(\mathbf{\Omega}_{\text{Tx}}) = E\left\{\left|\iiint h(\tau\,;\,t\,;\,\mathbf{\Omega}_{\text{Tx}}\,;\,\mathbf{\Omega}_{\text{Rx}})d\tau dtd\mathbf{\Omega}_{\text{Rx}}\right|^2\right\}, \tag{1.18}$$

the mean Tx angle $\overline{\mathbf{\Omega}}_{\text{Tx}}$ and RMS Tx angular spread $\mathbf{\Omega}_{\text{Tx, rms}}$ are then defined as [28]

$$\overline{\mathbf{\Omega}}_{\text{Tx}} = \frac{\int \mathbf{\Omega}_{\text{Tx}}\mathcal{P}(\mathbf{\Omega}_{\text{Tx}})d\mathbf{\Omega}_{\text{Tx}}}{\int \mathcal{P}(\mathbf{\Omega}_{\text{Tx}})d\mathbf{\Omega}_{\text{Tx}}}, \tag{1.19}$$

$$\boldsymbol{\Omega}_{\text{Tx, rms}} = \sqrt{\frac{\int \left(\boldsymbol{\Omega}_{\text{Tx}} - \overline{\boldsymbol{\Omega}}_{\text{Tx}}\right)^2 \mathcal{P}(\boldsymbol{\Omega}_{\text{Tx}}) d\boldsymbol{\Omega}_{\text{Tx}}}{\int \mathcal{P}(\boldsymbol{\Omega}_{\text{Tx}}) d\boldsymbol{\Omega}_{\text{Tx}}}}. \tag{1.20}$$

Note that $\overline{\boldsymbol{\Omega}}_{\text{Tx}}$ is a vector with the mean Tx azimuth and elevation angles $\overline{\theta}_{\text{Tx}}$ and $\overline{\phi}_{\text{Tx}}$, respectively. The vector $\boldsymbol{\Omega}_{\text{Tx, rms}}$ contains the corresponding RMS values $\theta_{\text{Tx,rms}}$ and $\phi_{\text{Tx,rms}}$. The angular spread at the Rx side can be characterized in a similar manner.

Though, the RMS angular spread has drawn only little attention in the literature up to now for vehicular radio propagation channels. RMS azimuth spreads in the range of 25 - $35°$ are reported in intersection scenarios, and smaller values between 10 and $20°$ in Non-Line-of-Sight (NLoS) situations or congestion scenarios [34].

These spread parameters are important metrics in the design of communication systems, especially in fast time-varying environments. Indeed, large RMS delay spreads mean that the transmitted signal is smeared over time, owing to interactions with the scattering environment. Hence, different symbols may arrive at the same time at the Rx side, what yields to intersymbol interference [28]. Moreover, large RMS Doppler spreads indicate that the radio propagation channel varies considerably over time, even over one Orthogonal Frequency Division Multiplexing (OFDM) symbol. In that case, orthogonality between the subcarriers is lost, leading therefore to inter-carrier interference [28] and to the degradation of the overall system performance. Finally, the RMS angular spread can be used in adaptive beamforming applications (when considering the Tx and/or Rx antenna directivities). Indeed, large RMS angular spreads imply that the transmitted signal is smeared over a wide angular range (owing to either the Tx and Rx antennas or the scatterers), such that a large spatial diversity gain is possible. On the other hand, low RMS angular spreads indicate that the Tx and/or Rx antenna directivities can be narrowed, yielding therefore possible higher power gains.

1.1.4 From SISO to MIMO radio propagation channels

Double-directional MIMO radio propagation channels

The double-directional structure of the radio propagation channel can be exploited only in MIMO communication systems, with N_t and N_r closely-spaced antennas at the Tx and Rx sides respectively, as shown in Fig. 1.5. For a narrowband radio propagation channel (or, equivalently, for each delay bin of a wideband one), each Tx-Rx antenna link can undergo a different realization of the radio propagation channel. As a consequence, if a link is affected by

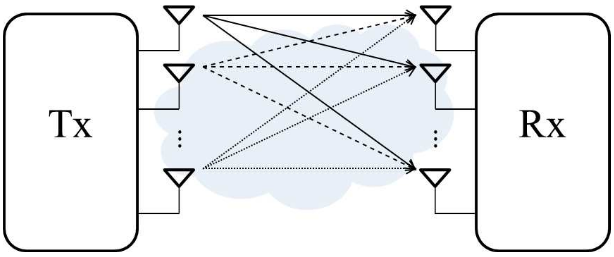

Figure 1.5: Principle of MIMO wireless communication systems.

a deep fade (owing to destructive interferences of the multipath components), then a reliable transmission of the transmit signal is still possible by using the other Tx-Rx antenna links that would not be in the fade (since the effects of fading are very local, they can vary significantly from one element to another for a same antenna array). For a double-directional radio propagation channel, the MIMO channel matrix can be expressed as

$$\mathbf{H}(\tau\,;\,t) = \begin{bmatrix} h_{11}(\tau\,;\,t) & \dots & h_{1N_t}(\tau\,;\,t) \\ \vdots & \ddots & \vdots \\ h_{N_r1}(\tau\,;\,t) & \dots & h_{N_rN_t}(\tau\,;\,t) \end{bmatrix}, \tag{1.21}$$

where each entry corresponds to a given Tx-Rx antenna pair. The input-output relationship as given in Eq. (1.1) can in that case be rewritten as

$$\mathbf{y}(t) = \mathbf{H}(\tau\,;\,t) * \mathbf{x}(t) + \mathbf{n}(t), \tag{1.22}$$

where $\mathbf{x}$ denotes a $N_t \times 1$ vector containing the transmitted samples, while $\mathbf{y}$ and $\mathbf{n}$ are $N_r \times 1$ vectors containing the received samples and the receiver noise, respectively. Combining Eqs. (1.7) and (1.21), the expression of the double-directional MIMO radio propagation channel can then be rewritten as

$$\mathbf{H}(\tau\,;\,t) = \sum_{l=0}^{L-1} e^{j2\pi\nu_l t}\, \mathbf{G}_{\mathrm{Rx}}(\mathbf{\Omega}_{\mathrm{Rx},l})\; a_l\; \mathbf{G}_{\mathrm{Tx}}^{\mathrm{T}}(\mathbf{\Omega}_{\mathrm{Tx},l})\; \delta(\tau - \tau_l), \tag{1.23}$$

where $\mathbf{G}_{\mathrm{Tx}}(\mathbf{\Omega}_{\mathrm{Tx},l})$ and $\mathbf{G}_{\mathrm{Rx}}(\mathbf{\Omega}_{\mathrm{Rx},l})$ are $N_t \times 1$ and $N_r \times 1$ vectors including the antenna pattern effects and the steering vector of the Tx and Rx antenna arrays in directions $\mathbf{\Omega}_{\mathrm{Tx},l}$ and $\mathbf{\Omega}_{\mathrm{Rx},l}$, respectively. Similarly, by extension of Eq. (1.8) to the case of multi-antenna communication systems, the expression of the double-directional MIMO radio propagation channel becomes

$$\mathbf{H}(\tau\,;\,t) = \sum_{l=0}^{L-1} e^{j2\pi\nu_l t}\,\mathbf{G}_{\text{Rx}}(\mathbf{\Omega}_{\text{Rx},l}) \times \begin{bmatrix} a_{l,vv} & a_{l,vh} \\ a_{l,hv} & a_{l,hh} \end{bmatrix} \mathbf{G}_{\text{Tx}}^{\text{T}}(\mathbf{\Omega}_{\text{Tx},l})\;\delta(\tau-\tau_l), \tag{1.24}$$

where $\mathbf{G}_{\text{Tx}}(\mathbf{\Omega}_{\text{Tx},l})$ and $\mathbf{G}_{\text{Rx}}(\mathbf{\Omega}_{\text{Rx},l})$ are $N_t \times 2$ and $N_r \times 2$ vectors including the antenna pattern effects and the steering vector of the Tx and Rx antenna arrays in directions $\mathbf{\Omega}_{\text{Rx},l}$ and $\mathbf{\Omega}_{\text{Tx},l}$, respectively. Each line of these matrices describes the response of one element of the Tx or Rx antenna array to the vertical and horizontal polarizations.

In the following of this thesis, note that polarization aspects of the radio propagation channel will be neglected, so that each pair of Tx-Rx polarization will be considered as a distinct Tx-Rx antenna link.

Space-only characterization of MIMO radio propagation channels

The multidimensional modeling approach in Section 1.1.3 is sufficient for the complete statistical description of MIMO radio propagation channels (assuming that they can be fully characterized by their second-order statistics). Nonetheless, it is difficult to estimate these correlation functions from measurements and to interpret them, owing to the large number of parameters on which they depend. Since MIMO radio communication systems exploit the spatial diversity of the propagation channel, it is then reasonable to consider the space-only characterization of the underlying radio propagation channels. If both the delay and time shifts are set to zero (i.e. $\tau = \tau'$ and $t = t'$), then Eq. (1.10) can be rewritten as the delay-dependent full spatial correlation matrix

$$\mathbf{R}_{\text{full}}(\tau) = \mathrm{E}\left\{\text{vec}\left[\mathbf{H}(\tau\,;\,t)\right]\text{vec}\left[\mathbf{H}(\tau\,;\,t)\right]^{H}\right\}, \tag{1.25}$$

where the operator vec $[\cdot]$ stacks the matrix columns into a single column vector. Its $N_rN_t \times N_rN_t$ elements represent the correlation coefficients between all Tx-Rx antenna links, which can also be classified as

- The Tx correlation coefficients, which are due to interactions at the Tx side. They can be expressed as the $N_t \times N_t$ spatial correlation matrix

$$\mathbf{R}_{\text{Tx}}(\tau) = \mathrm{E}\left\{\mathbf{H}^{T}(\tau\,;\,t)\mathbf{H}(\tau\,;\,t)^{*}\right\}, \tag{1.26}$$

- The Rx correlation coefficients, which are due to interactions at the Rx side. They can be expressed as the $N_r \times N_r$ spatial correlation matrix

$$\mathbf{R}_{\mathrm{Rx}}(\tau) = \mathrm{E}\left\{\mathbf{H}(\tau\,;\,t)\mathbf{H}^{H}(\tau\,;\,t)\right\}, \tag{1.27}$$

- The cross-correlation (off-diagonal) coefficients, which are due to combined interactions at both Tx-Rx sides. Though, a number of these coefficients are difficult to be interpreted physically.

The dimension of the full spatial correlation matrices grows quadratically with the sizes of the MIMO antenna arrays used at the Tx and Rx sides. This draws important issues in terms of complexity (since they can be too large to be used as such in communication schemes) and identifiability (as they may be ill-conditioned if they are estimated from an insufficient number of time instants). Hence, MIMO radio communication systems do not often make use of estimated full spatial correlation matrices. Tx and Rx spatial correlation matrices are indeed often preferred, since they are simplier to estimate and can therefore be used in adaptive processing at the Tx and Rx sides separately, long-e.g. when term time-averaged spatial statistics are evaluated at the Rx side and fed back to the Tx one, so that this latter can optimize its transmission scheme. As a consequence, these spatial correlation matrices provide useful information on changes in the radio propagation channel as seen from one side or another.

Their structures can be analyzed by means of their respective eigenvalue decomposition, which is given by

$$\mathbf{R_{Tx}} = \mathbf{U_{Tx}}\boldsymbol{\Lambda}_{\mathbf{Tx}}\mathbf{U_{Tx}}^{\mathrm{H}}, \tag{1.28}$$

$$\mathbf{R_{Rx}} = \mathbf{U_{Rx}}\boldsymbol{\Lambda}_{\mathbf{Rx}}\mathbf{U_{Rx}}^{\mathrm{H}}, \tag{1.29}$$

where $\mathbf{U_{Tx}}$ (resp. $\mathbf{U_{Rx}}$) is a unitary matrix containing the eigenmodes of $\mathbf{R_{Tx}}$ (resp. $\mathbf{R_{Rx}}$) at their columns, whereas $\boldsymbol{\Lambda}_{\mathbf{Tx}}$ (resp. $\boldsymbol{\Lambda}_{\mathbf{Rx}}$) is a diagonal matrix containing the corresponding eigenvalues sorted in descending order, such that $\lambda_1 \geq \lambda_2 \geq \cdots \geq \lambda_{N_{r/t}}$. The strongest eigenvalues (that exceed a certain threshold, which depends on the measurement system) characterize the signal subspace, i.e. the number of uncorrelated fading processes that contribute to the radio propagation channel (while the remaining ones are too weak and below the noise level, so that they can be associated to the noise subspace). Even though these strongest eigenvalues do not have any physical interpretation in the radio wave propagation (they indeed correspond to weighted sum of multipath components), they characterize the degree of spatial diversity in the radio propagation channel.

1.2 Non-stationary radio propagation channels

1.2.1 Sources of non-stationarity

Unfortunately, the WSS-US-H assumption is really restrictive since it implies that the statistics of the radio propagation channel do never change, whether it be on infinite time, frequency or angular intervals. It is indeed obviously unrealistic, especially for real-world vehicular radio propagation channels that are

- Time-varying, owing to the high mobility of the Tx and Rx vehicles as well as of the scatterers (e.g. other traveling vehicles, etc.). Some scatterers can indeed suddenly appear (or disappear) in the environment surrounding the Tx and Rx vehicles. The LoS component can also be intermittently be obstructed by large obstacles. All these effects result in a non-stationary behavior of the radio propagation channel. In other words, its statistics can fluctuate significantly over time, so that the WSS assumption is no longer fulfilled,

- Frequency-varying, owing to either large obstacles (e.g. buildings, protection walls on roadsides, bridges, etc.) or multiple-bounce interactions with the surrounding environment (e.g. diffuse scattering due to vegetation, waveguiding in tunnel scenarios, etc.). In other words, correlated multipath components can arrive with different delays at the Rx side, so that the US assumption is no longer fulfilled,

- Angular-varying, owing to changes in the AoDs and AoAs, owing to the relative motion of the Tx, the Rx and scatterers, so that the homogeneity assumption is no longer fulfilled.

The intrinsic characteristics of the radio communication systems can strongly impact the non-stationary behavior of the radio propagation channel. For example, the larger the bandwidth (i.e. the higher the delay resolution), the better the ability to discriminate multipath components arriving with different delays. Hence, multipath components arriving with closer delays are more correlated, what clearly violates the US assumption [35]. Similarly, the shape of the antenna arrays (with elements looking in different directions), the spacing between the antenna elements or non-isotropic antenna patterns strongly impact on the resolution of the angular sampling and thus on the validity of the H assumption.

However, the radio propagation channel statistics do not change instantaneously, such that it is possible to identify bounded time, frequency or angular intervals within which they remain constant (i.e. over which the WSS-US-H assumption is locally fulfilled). Reliable estimates of the radio propagation channel statistics can therefore be obtained only over those time, frequency and space intervals.

1.2.2 Measuring the non-stationarity

Different methods have been proposed in the literature to measure the non-stationarity of radio propagation channels and to identify stationarity regions.

The stationarity of SISO radio propagation channels was investigated in [36], where local regions of stationarity were identified based on the correlation between consecutive PDPs. Alternatively, a framework for the characterization of the non-stationary behavior of SISO radio propagation channels over time and frequency was proposed in [37, 38]. The concept of Local Scattering Function (LSF) was first introduced as an extension of the scattering function to the non-stationary case. Stationarity regions in time and in frequency were then identified by applying similarity metrics (e.g. collinearity, spectral divergence, etc.) to the so-estimated LSFs. This approach has been used for the characterization of the non-stationary behavior of vehicular MIMO radio propagation channels and the identification of stationarity regions in [39, 40, 41, 42, 43].

Regarding Single-Input Multiple-Output (SIMO) radio propagation channels, the F-eigen ratio was introduced in [44] to measure the discrepancy between spatial correlation matrices at the Rx side. It corresponds to the penalty that is undergone (in terms of power loss) when out-dated spatial statistics are used in beamforming applications instead of the actual ones. Nonetheless, the F-eigen ratio is interesting only when the transmission is done over a reduced number of eigenmodes, and hence loses of its interest when all the eigenmodes are considered (e.g. in MIMO communication systems). For MIMO radio propagation channels, statistical tests based on their evolutionary spectrum estimated at different time instants were used in [45, 46] to determine time intervals over which the WSS assumption does remain valid. Stationarity distances were also estimated, which were found to be larger in presence of the LoS component. However, none of these methods really takes advantage of the knowledge of the spatial structure of MIMO radio propagation channels. For that purpose, the Correlation Matrix Distance (CMD) was introduced in [27, 47, 48, 49] in order to determine the amount of change in the spatial structure of the underlying MIMO radio propagation channel over time.

1.3 Radio propagation channel models

Realistic radio propagation channels models are important tools that have to be integrated in emulators in order to design and/or validate (parts of) communication systems, in a fully reproducible and parameterizable manner, before its deployment.

Since vehicular radio propagation channels are intrinsically non-stationary, their statistics can fluctuate significantly and rapidly over time, frequency and space. Hence, any good vehicular radio propagation channel model should be able to handle these non-stationary behaviors. To do so, different possible approaches can be considered for the characterization of MIMO radio propagation channels, which can be classified as [9, 28]

- Deterministic (physics-based) models, which explicitly rely on the propagation of the electromagnetic waves in the environment,
- Stochastic models, which account for the radio propagation channel only based on its statistical properties, i.e. with no physical justification related to the surrounding scattering environment,
- Geometry-based stochastic models, which have some characteristics of both the deterministic and stochastic models.

Each of these approaches has its own advantages and disadvantages, so that the choice of a radio propagation model strongly depends on the application that is targeted. It also depends on the system assumptions and has to take into account the trade-off between accuracy and complexity.

1.3.1 Deterministic channel models

Deterministic channel models seek at characterizing the radio wave propagation in a specific environment, which has to be defined with a certain level of accuracy. This requires a detailed description of the environment under investigation, including not only the intrinsic characteristics of the physical objects (e.g. their two- or three-dimensional geometries and positions, their material properties, etc.), but also people, weather conditions, realistic vehicular traffic models, etc.

The radio wave propagation is usually obtained via ray-tracing approaches [19, 50, 51, 52]. All possible propagation paths between the Tx and Rx sides are generated using geometrical optics laws. The interactions between the transmitted electromagnetic waves and the scattering environment are then modeled with the Fresnel coefficients for reflections, the universal theory of

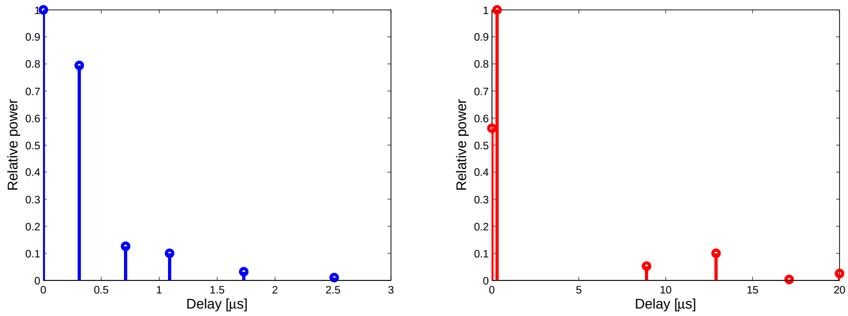

(a) ITU model (A). (b) ITU model (B).

Figure 1.6: ITU radio propagation channel models for testing vehicular environments, as used in the IEEE 802.11p standard.

diffraction, empirical diffraction or reflection models, etc. Diffuse scattering due to surface roughness can also be considered by including a statistical component in these deterministic approaches [53]. The total radio propagation channel is finally obtained by summing all the multipath components at the Rx side (after being weighted by the Tx and Rx antenna patterns).

Deterministic approaches provide very realistic and accurate estimations of the radio propagation channel (in terms of pathloss coefficients, RMS delay or Doppler spreads, etc.) in some specific environments (e.g. urban macrocells, street canyons, etc.). However, these approaches are difficult to calibrate (regarding the material properties, etc.) and computationally very expensive (depending on the number of parameters used in order to describe the environment and on the targeted level of accuracy). Hence, deterministic (ray-tracing) approaches are usually used only for very specific applications, e.g. for antenna positioning [54, 55, 56, 57], since they do not appear suitable for more complex simulations of wireless communication systems (e.g. for higher layer applications).

1.3.2 Purely stochastic channel models

Even though the radio propagation channel can vary over time, frequency and space, it does not fluctuate in a completely random manner. As a consequence, these variations can be represented by means of descriptive statistics, which do not necessarily have a physical signification. The statistical properties of SISO radio propagation channels can therefore be modeled according to some specific parameters, e.g. delay, Doppler shift, AoD, AoA, etc.

The most popular stochastic channel model of this kind is the Tapped-

Delay Line (TDL), which is based on the WSS-US assumption. The radio propagation channel is in that case described by a finite number of delay taps, each one being assumed to fade independently with given statistics (e.g. amplitude distribution, Doppler spectrum, etc.) that can be extracted from experimental measurement campaigns. Six- and twelve-tap models were developed at 2.4 GHz for various environments [58, 59]. Since each tap contains several paths (each with its own Doppler spectrum, that can be selected from a small number of shapes), they can be assigned an almost arbitrary Doppler spectrum.

Two TDL models have been adopted as reference models in the 802.11p standard [3]. They characterize vehicular environments with either low RMS delay spreads (model A) or medium RMS delay spreads (model B), respectively, and are represented in Fig. 1.6.

The main advantage of such TDL models is that they are mathematically very simple, so that they have low complexity and are easy to use. However, as pointed out in [60], they fail to reproduce some important characteristics of real-world physical radio propagation channels, especially their non-stationary behavior (since they strongly rely on the WSS-US assumption, with fading statistics for each tap constant over time). These models can thus be complexified to account for the non-stationary behavior of the radio propagation channel, e.g.

- “Birth/death” Markov processes, so as to model the appearance and disappearance of taps [21, 61]. However, they are not able to account for strong discrete scatterer contributions “drifting” from one tap to another (i.e. to address the US assumption),

- Different TDL models for regions exhibiting different delay spread or Bit Error Rate (BER) statistics [62]. Though, this approach is not able to provide radio propagation channel realizations with continuous statistics over time.

As these stochastic TDL models are unable to simulate realistic non-stationary radio propagation channel, they have therefore a significant impact on the estimation of communication system performances, e.g. underestimating the BER in single-carrier and multicarrier systems [22].

1.3.3 Geometry-based stochastic channel models

Geometry-based Stochastic Channel Models (GSCMs) are the combination of the deterministic and stochastic approaches. In such models, the radio wave propagation and the scattering aspects are indeed decoupled.

The positions of the scatterers in the environment are determined at random (according to some suitable statistical distributions), e.g. on two-dimensional (i.e. in the horizontal plane, elevation being usually not considered) rings located around the Tx and Rx [31]. This model can be complexified by considering the possibility of a LoS component [63], non-isotropic scattering environments [63, 64], an additional elliptical ring of scatterers [64], scatterers placed on three-dimensional cylinders [65, 66, 67], etc. The multipath components are obtained by applying very simplified models for the propagation of the electromagnetic waves and their interactions with the scatterers, e.g. assuming only single- or double-bounced reflections. Each multipath component is then assigned fading properties that are drawn from statistical distributions. The radio propagation channel is then obtained by summing all the multipath components at the Rx side. These geometrical models can be used in order to derive tractable closed-form expressions of the level crossing rate [68], the temporal variation of the MIMO spatial correlation [69, 70], the joint space-time correlation function [69, 71], etc. Though, as the scattering environment remains static over time (scatterers are indeed assumed to always stay at their position), they fail to reproduce a realistic physical environment, and do therefore not handle the non-stationary behavior of the radio propagation channel.

Another approach consists in placing (strong) scatterers at physically more realistic positions, e.g. buildings, road signs or vegetation on the road sides, vehicles placed on different (parallel) road lanes, etc. Diffuse scattering can also be considered, by placing numerous (low-power) scatterers on the road sides [72, 73]. As the scattering environment is now dynamic (i.e. the movement of the scatterers is taken into account), this approach inherently describes the non-stationary behavior of the radio propagation channel.

1.4 Experimental channel investigation

Owing to their non-stationarity in time, frequency and space, inter-vehicular radio propagation channels have to be investigated and parameterized from dedicated measurement campaigns which have specific requirements, especially in terms of

Measurement set-ups

The first inter-vehicular measurement campaigns were conducted before the introduction of the IEEE 802.11p standard in 2006, either in the Global System for Mobile Communications (GSM) band around 900 MHz [74, 75, 76] or in the WiFi band around 2.4 GHz [58, 62, 76]. Narrowband SISO measurement set-ups were mostly considered [19, 74, 75, 77, 78], using either spectrum analyzers [19] or vector network analyzers [16, 79]. As a consequence, only the time selectivity of vehicular radio propagation channels was characterized, in terms of pathloss [74, 75], small-scale fading analysis [19, 74], Doppler spread [19], etc.

After 2006, inter-vehicular measurement campaigns have shifted towards the 5 GHz band in which the IEEE 802.11p standard will operate [13, 14, 20, 32, 33, 80]. Moreover, the time, frequency and space selectivity of vehicular double-directional radio propagation channels started also to be investigated. Hence, MIMO measurement set-ups were adopted, e.g. with antenna arrays having dimensions $N_r \times N_t = 2 \times 2$ [80] or $N_r \times N_t = 4 \times 4$ [81, 82], respectively. On the other hand, larger measurement bandwidths were also considered in order to characterize frequency selectivity, e.g. 20 MHz [14], 50 MHz [78], up to 240 MHz [80, 83].

Vehicles and antennas

The type of vehicles and the location of the antennas on the vehicles at the Tx and Rx sides can significantly impact on the estimation of the radio propagation channel. For example, since the Tx and Rx antennas are roughly at the same (low) height, inter-vehicular communications mostly occur in the horizontal plane and the Tx-Rx link is likely to be obstructed by other vehicles in the traffic. On the other hand, strong multipath components can stem from the metallic roofs of the Tx and/or Rx measurement vehicles.

The Tx and Rx measurement vehicles are usually regular passenger vehicles or vans. The antennas can be placed either on top of their roofs [14, 80, 84] or within the vehicles, e.g. on loading platforms or on dashboards [13, 33, 81]. The placement of the antennas at the Tx and Rx sides has a significant impact on pathloss, delay spread or packet error rate [33, 85]. Note that most of the antennas that have been used in these measurement campaigns are regular antennas, that are not integrated to the measurement vehicles in a realistic manner. Nonetheless, specific antennas were designed in order to be fully integrated in radome cavities together with other GSM or FM radio antennas [54], and then used in realistic inter-vehicular communication scenarios [86].

Environments and scenarios

The characteristics of vehicular radio propagation channels strongly depend on the nature of the scattering environment surrounding the Tx and Rx measurement vehicles. These environments are usually classified as highways, rural, sub-urban and urban areas and have been already widely investigated and well documented for other cellular radio communication systems [10]. This classification is sufficient for a large number of road traffic safety applications and has been considered in several inter-vehicular measurement campaigns [14, 19, 33, 77, 87]. However, there are some applications very specific to vehicular communication systems that can not be included in this classification. This concerns for example intersection scenarios, e.g. in order to avoid possible collisions [88], or in-tunnel scenarios, e.g. in order to prevent traffic jams after an accident in a tunnel by broadcasting warning messages to the approaching vehicles [87]. Hence, each of these critical applications requires to be characterized separately, with dedicated radio propagation channel models [89] and measurement campaigns [86, 90].

1.5 Outline and contributions

Chapter 2: Vehicle-to-vehicle measurement campaigns

The measurement data used throughout this thesis are described in this Chapter. They were collected during two different measurement campaigns conducted in collaboration with Aalto University in 2007 and 2009, respectively. A short introduction on the concept of channel sounding is first provided. Afterwards, the technical details of each of these measurement campaigns are described, regarding the measurement set-ups and equipments as well as the investigated environments and scenarios (including their main characteristics).

Chapter 3: Non-stationarity of vehicular radio propagation channels

In this Chapter, we first characterize the frequency- and time-dependent behavior of the spatial structure of vehicular MIMO radio propagation channels. It is shown that significant changes, which may occur in the scattering environment (or, equivalently, in the radio wave propagation), are captured.

Based on these observations, we use the CMD as a measure of the amount of change in the spatial structure of MIMO radio propagation channels. This indicates how different neighboring spatial correlation matrices estimated at different time instants and frequencies can be. Since the CMD is a bounded metric, an appropriate threshold value can then be determined in order to quantitatively assess the (in-)validity of the WSS and US assumptions in vehicular radio propagation channels. Hence, stationarity regions in time and frequency can be identified, over which the WSS and US assumptions locally hold (i.e. where the fading statistics are constant), respectively.

Chapter 4: Non-stationary modeling of V2V fading statistics

Based on the observations done in the previous Chapter, we can now describe stochatically the time- and frequency-dependent behavior of the fading statistics of vehicular radio propagation channels.

First, we consider the non-stationary modeling of the fading statistics for narrowband radio propagation channels (i.e. assuming that the US assumption holds over the whole measurement bandwidth). The large- and small-scale fading statistics are estimated over time-varying stationarity intervals (over which the WSS assumption was found to hold), such that a faithful representation of the underlying fading properties can be obtained at any given time instant. Their time- and space-variabilities are also characterized.

Besides, this non-stationary analysis is extended to wideband radio propagation channels. The statistics of the small-scale fading are estimated using the same non-stationary approach, on a per-frequency bin basis. The frequency-, time- and space-variabilities of the so-extracted small-scale fading statistics are then investigated. On the other hand, the second-order moment of the radio propagation channel (in terms of RMS delay spread) are considered, and their space- and time-varying behavior are taken into account.

Chapter 5: Geometry-based stochastic channel modeling

In this Chapter, we now consider a GSCM approach for the description of wideband vehicular double-directional radio propagation channels. Since each multipath component is modeled separately, the GSCM approach inherently captures the non-stationary behavior of radio propagation channels.

The discrete scatterers are placed at physically realistic positions in the environment surrounding the Tx and Rx vehicles. Their contributions are indeed generated using very simplified ray-tracing tools, whereas their fading is modeled as the combination of a deterministic distance-decaying process and two stochastic small and large-scale processes. Moreover, the diffuse scattering is investigated and included in the GSCM, being characterized in a purely stochastic way. The complete parameterization of the model is provided, so that realizations of this vehicular radio propagation channel model can be easily generated.

CHAPTER 2
Vehicle-to-vehicle MIMO measurement campaigns

The design and deployment of the IEEE 802.11p, as well as alternative V2V wireless communication systems, requires therefore (according to Chapter 1) the knowledge of the underlying vehicular radio propagation channel characteristics, which may be significantly different from those of classical cellular wireless networks since *(i):* both the Tx and the Rx can be mobile (with possibly high velocities), *(ii):* the antennas have relatively low heights and *(iii):* the surrounding scattering environment can change very rapidly. Hence, the extensive evaluation of inter-vehicular radio propagation channels in real-world scenarios is needed, from which the estimation of these characteristics could be performed in order to derive accurate (measurement-based) models able to reliably reproduce the time-varying behavior of these characteristics.

For that purpose, two different measurement campaigns were conducted in collaboration with Aalto University in August 2007 and 2009, respectively, in order to characterize inter-vehicular MIMO radio propagation channels in the 5 GHz band. The main characteristics of these measurement campaigns are discussed in the following of this Chapter. The so-collected data will serve as a basis for the analysis conducted throughout this thesis.

2.1 Aalto channel sounder

The Aalto channel sounder is an in-house designed measurement system operating at a center frequency of 5.3 GHz, which is based on the switched-array principle [91]. This is a popular technique, which uses only one single RF chain in order to scan sequentially (using fast switches on both link ends) the radio propagation channel for all pairs of Tx and Rx antenna elements, as shown in Fig. 2.1. For every Tx antenna element, the whole Rx antenna array is therefore gone through (i.e. every Rx antenna element is measured) before the Tx antenna element is switched.

For that purpose, a Pseudo-Noise (PN) sequence is used as a measurement signal. It consists in a binary sequence with autocorrelation function similar to the one of noise, i.e. equal to one when the delay is zero and with small

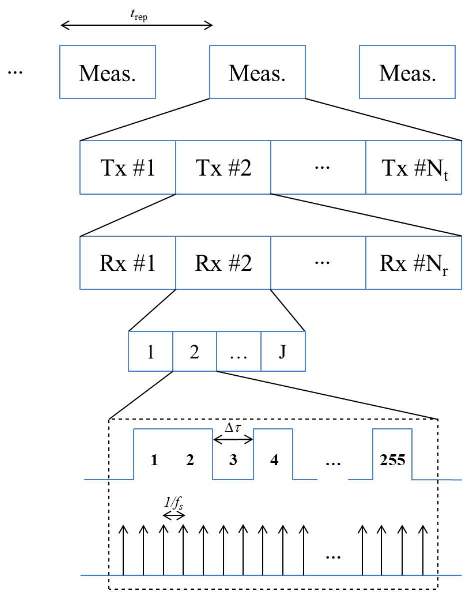

Figure 2.1: Principle of the switched array sounding technique.

values, close to zero, for other delay values. As a crucial issue, note that owing to these imperfections, the frequency response of the PN sequence is therefore not completely flat over the whole measurement bandwidth, since the transmitted power drops significantly on its edges. The behavior of the underlying radio propagation channel may therefore be clearly misestimated at these frequencies. This sequence has $M_f = 255$ chips sampled at rate 60 MHz (i.e. leading to a delay resolution $\Delta\tau$ of 16.7 ns), having therefore a total length of 4.25 µs. Each chip consists of two samples, so that the corresponding sampling rate is of 120 MHz.

This PN sequence is first modulated, up-converted to the desired center frequency and then sequentially switched to every Tx antenna element (out of a total number N_t). Reciprocally, every Rx antenna element is switched sequentially (out of a total number N_r), the received signal being then band-pass filtered, down-converted back to the base-band and demodulated. Moreover, the PN sequence is transmitted J times for every Tx-Rx antenna pair, for averaging reasons. This way, for each snapshot the transmitted code is measured $N_\mathrm{r} \times N_\mathrm{t} \times J$ times. The IR of the underlying radio propagation channel can then be measured for each antenna link by directly correlating the received signal with the transmitted one, which has therefore to be known *a priori* at both the Tx and Rx sides. Note that the TF of the radio propagation channel can also be obtained from the IR, by means of a simple one-dimensional Fourier transform.

As a consequence, such a sounding technique requires a given time reference and a very accurate synchronization between the Tx and Rx units, which are here provided by Rubidium clocks. Moreover, a back-to-back calibration procedure has to be conducted before every measurement campaign, so that the RF cable losses and the non-linear distorsions of the Tx power amplifier can be normalized from the measured IRs of the radio propagation channel.

The sounding of fast time-varying frequency selective radio propagation channels (typically in vehicular environments) requires special attention, as the two-dimensional Nyquist criterion has to be fulfilled [60], i.e.

- $t_{\text{rep}} \leq 1/2\nu_{\text{max}}$, i.e. the temporal resolution of the measurement system has to be shorter than the coherence time of the radio propagation channel under investigation (or, equivalently, the radio propagation channel is assumed to remain constant between two consecutive snapshots),
- $t_{\text{rep}} \geq \tau_{\text{max}}$, i.e. the temporal resolution of the measurement system has to be larger than the maximum delay of the radio propagation channel under investigation (or, equivalently, two consecutive snapshots do not have to overlap).

If these two conditions are satisfied, then the radio propagation channel under investigation is said to be underspread.

2.2 Aalto 2007: Measurement campaign

This campaign aimed at performing measurements of inter-vehicular MIMO radio propagation channels in various environments, for safety-related ITS applications. In this Section, we provide more details on the measurement set-up, the equipments as well as on the investigated scenarios.

2.2.1 Parameter set-up

As already mentioned, the Aalto channel sounder performs MIMO measurements at a center frequency of 5.3 GHz, that can be regarded as being as close to the 5.9 GHz frequency band of the IEEE 802.11p standard such that no significant differences in channel statistics are expected.

The radio propagation channel for every Tx-Rx antenna pair was measured a number $J = 2$ of times, before switching to the next Tx-Rx antenna pair. The maximum transmit power was 36 dBm (i.e. 3.98 W). The snapshot time

Table 2.1: Set-up parameters of the Aalto 2007 measurement campaign.

Center frequency, f_c	5.3 GHz
Transmit power, P_{Tx}	36 dBm
Code length, M_f	255 chips
Measurement bandwidth, BW	60 MHz
Sampling frequency, $f_s = 1/T_s$	120 MHz
Delay resolution, $\Delta\tau = 1/BW$	16.7 ns
Snapshot time, t_{snap}	8.4 ms
Snapshot repetition rate, $\nu_{rep} = 1/t_{rep}$	14.3 Hz

(i.e. the time required to measure the radio propagation channel for all Tx-Rx antenna pairs) was set at $t_{snap} = 8.4$ ms, whereas the snapshot repetition rate ν_{rep} was set at 14.3 Hz to limit the recorded file sizes. The main channel sounder parameters are summarized in Table 2.1.

With these settings, the maximum resolvable Doppler shift ν_{max} is limited to 7.15 Hz, what yields a maximum relative speed between the Tx-Rx vehicles and the discrete scatterers of only 1.45 km/h. As a consequence, the snapshot repetition rate ν_{rep} of the sounding signal is here definitely much smaller than the maximum Doppler shift ν_{max} that can be expected in vehicular environments (typically owing to other traveling vehicles, which are likely to have much higher velocities), i.e.

$$\nu_{rep} > 2\,|\nu_{max}| = 2\Delta v_{max}\frac{f_c}{c}. \tag{2.1}$$

In other words, the double Nyquist criterion is not completely fulfilled (its first condition being indeed not respected), such that the temporal behavior of the multipath components stemming from the discrete scatterers will clearly be undersampled (or, equivalently, will suffer aliasing). The Doppler information can definitely not be reliably estimated (and later correctly exploited) from the data collected during this measurement campaign and will therefore be ignored in the following of this thesis.

2.2.2 Tx and Rx antenna arrays

Semi-spherical antenna arrays were used at the Tx and Rx sides. The antenna arrays consist of 16 dual-polarized elements (i.e. 32 feeds), which are arranged in a spherical geometry [91], as shown in Fig. 2.2. The reference direction of the Tx and Rx antenna arrays was always pointing towards the front of the measurement vehicles (i.e.towards the direction of motion of the vehicles). Polarizations are horizontal and vertical in the Rx antenna array, whereas they

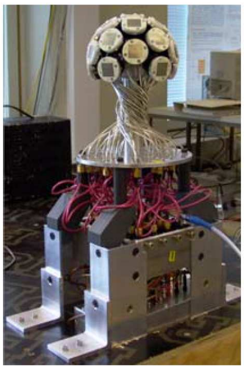

(a) Semi-spherical antenna array.

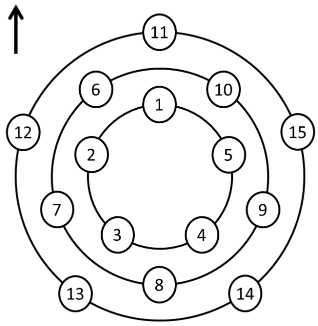

(b) Antenna element numbering.

Figure 2.2: Semi-spherical antenna array at the Tx and Rx sides. The arrow indicates the reference direction of the array.

are slanted at 45 degrees in the Tx one. Table 2.2 presents the allocation of the switch numbering (including polarization information) to the antenna elements at the Tx and Rx sides.

In the Rx antenna array, the first feed is replaced with a discone antenna, while the second feed is terminated and acted as a marker channel. In the Tx antenna array, the second last feed is terminated while the last feed is connected to a discone antenna and was not measured. The discone antennas are used for adjusting the Automatic Gain Control (AGC) of the channel sounder. Hence, for further calculations, the 15 remaining antenna elements at the Tx and Rx sides are selected in order to form the MIMO channel matrix, leading to $N_\mathrm{r} \times N_\mathrm{t} = 30 \times 30$ temporal multiplexed channels.

The Tx (resp. Rx) antenna array was mounted on top of a wooden platform on the roof of realistic passenger vehicles, i.e. an Opel Astra (resp. a Peugeot Partner). The antenna arrays were covered with a plastic tarpaulin to protect them from air streams and rain. The measurement set-up (i.e. the channel sounders, power amplifiers, batteries and laptops) was placed in the trunks of the measurement vehicles, as shown in Fig. 2.3.

2.2.3 Measured environments and scenarios

The measurement campaign was carried out in four different environments: on a campus (Otaniemi), on a highway (Ring 1), in sub-urban (Matinkyla, Lepp-

Table 2.2: Correspondence between the antenna elements and the switch numbers (including polarization information) at the Tx and Rx sides.

Antenna element	Tx side		Rx side	
	Polar. $\searrow$	Polar. $\nearrow$	Polar. $\uparrow$	Polar. $\rightarrow$
1	30	29	30	29
2	28	27	28	27
3	26	25	26	25
4	24	23	24	23
5	22	21	22	21
6	20	19	20	19
7	18	17	18	17
8	16	15	16	15
9	14	13	14	13
10	12	11	12	11
11	10	9	10	9
12	8	7	8	7
13	6	5	6	5
14	4	3	4	3
15	2	1	2	1

vaara) and urban (Helsinki) areas. Satellite photographs of these environments are depicted in Figure 2.4, which show that

- The campus and sub-urban areas are similar and mostly consist of small detached houses, parking lots and an average tree density of roughly 5 m high. There are large sidewalks and road signs sparsely distributed on both sides of the two-lane road as well as little to no traffic conditions,
- The six-lane highway is located in a sub-urban like area. The roadsides consist of natural (or artificial) embankments and low-height buildings, excepted around the exit ramps. There is a median strip with some vegetation and delimited by guardrails. Some roadsigns are scattered along the road. The Tx and Rx measurement vehicles are traveling on the hard shoulder, with traffic conditions from light to medium,
- The urban area is the city center of Helsinki, with six to eight-storey buildings on both sides of two-lane streets, medium to heavy traffic conditions and numerous roadsigns.

The Tx and Rx vehicles were always traveling in the same direction, the Tx ahead of the Rx one. The vehicles' speed was in the range of $5 - 15$ km/h, such that the channel coherence is, in the worst case, still larger than t_{snap}.

(a) Antenna array on the Tx roof.

(b) Antenna array on the Rx roof.

(c) Measurement equipment in the Tx trunk.

(d) Measurement equipment in the Rx trunk.

Figure 2.3: Pictures of the Tx and Rx measurement vehicles.

The inter-vehicle distance varied between 10 and 500 m, depending on the traffic conditions and the environment. Most of the measurement routes presented a strong LoS component between the Tx and Rx vehicles. However, the LoS component was possibly intermittently obstructed (even during one same measurement route), owing either to large vehicles (e.g. trucks, buses, etc.) traveling between the Tx and Rx vehicles or to buildings when one of the measurement vehicles was turning a corner.

(a) Satellite view of the campus area.

(b) Campus location.

(c) Satellite view of the urban area.

(d) Urban location.

(e) Satellite view of the sub-urban area.

(f) Sub-urban location.

(g) Satellite view of the highway area.

(h) Highway location.

Figure 2.4: Pictures of the environments investigated during the Aalto 2007 measurement campaign (Google ©).

Table 2.3: Set-up parameters of the Aalto 2009 measurement campaign.

Center frequency, f_{c}	5.3 GHz
Transmit power, P_{Tx}	36 dBm
Code length, M_f	255 chips
Measurement bandwidth, BW	60 MHz
Sampling frequency, $f_{\text{s}} = 1/T_{\text{s}}$	120 MHz
Delay resolution, $\Delta\tau = 1/BW$	8.33 ns
Snapshot time, t_{snap}	1.632 ms
Snapshot repetition rate, ν_{rep}	66.7 Hz

2.3 Aalto 2009: Measurement campaign

The objective of this campaign was to enlarge the already existing measurement data set of inter-vehicular MIMO radio propagation channels, which had been collected during the Aalto 2007 measurement campaign (as detailed in Section 2.2). In this Section, we provide more details on the measurement set-up, the equipments as well as on the investigated scenarios of this measurement campaign, with a special emphasis on what differs from the previous one.

2.3.1 Parameter set-up

The Aalto channel sounder was again used during this measurement campaign, with almost the same parameter set-up as the one described in Section 2.2.1. The only differences concern the snapshot time, which is chosen such that $t_{\text{snap}} = 1.632$ ms, and the snapshot repetition rate ν_{rep}, which is set at 66.7 Hz. The main channel sounder parameters are summarized in Table 2.3.

With these settings, the maximum resolvable Doppler shift ν_{max} is then of 33.35 Hz, hence yielding a maximum relative speed of 6.80 km/h between the measurement vehicles and the discrete scatterers. Again, the first condition of the double Nyquist criterion (as described in Section 2.1) is not fulfilled, such that the Doppler information will similarly be neglected in the following of this thesis.

2.3.2 Tx and Rx antenna arrays

A Uniform Linear Array (ULA) with 4 vertically polarized antenna elements is used at the Tx side, as shown in Fig. 2.5, whereas a dual-polarized semi-spherical antenna array is still used at the Rx side.

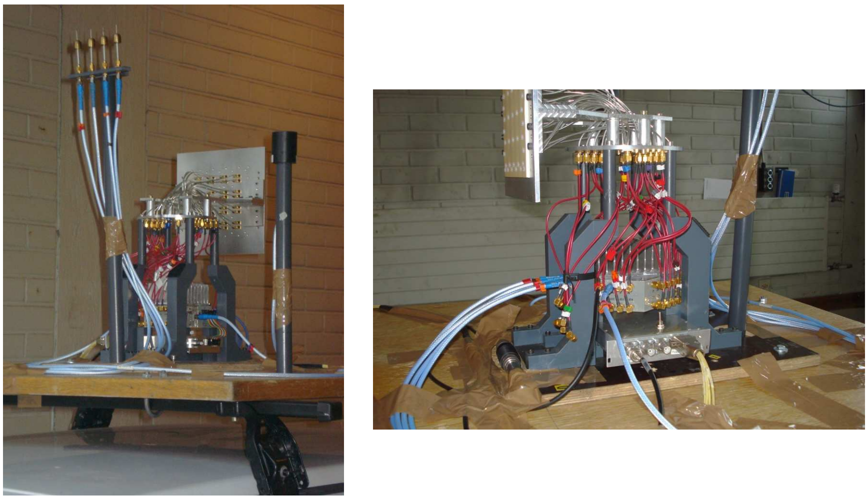

Figure 2.5: Pictures of the ULA used at the Tx side.

Discone antennas are also used at the Tx and Rx sides for adjusting the AGC of the channel sounder. For that purpose, the first feed of the Rx antenna array is thus replaced with a discone antenna, while its second feed is terminated and acts as a marker channel. The MIMO channel matrix is hence formed by $N_\mathrm{r} \times N_\mathrm{t} = 30 \times 4$ temporal multiplexed channels.

The Tx and Rx antenna arrays were mounted on a wooden platform on the car roofs. The antennas were covered with a plastic tarpaulin to protect them from air streams and rain. The main Tx and Rx measurement set-up is placed in the trunks of the Tx and Rx measurement vehicles that were previously used during the Aalto 2007 measurement campaign, as described in Section 2.2.2.

2.3.3 Measured environments and scenarios

This measurement campaign was conducted in three different environments: on a campus (Otaniemi), in sub-urban (Tapiola) and urban (Tapiola city center) areas. The two first ones were the same as the ones already described in Section 2.2.3. On the other hand, the city center of Tapiola consists of three to four-storey buildings on both sides of two-lane streets, occasional large open areas covered with vegetation and numerous roadsigns, as shown in Fig. 2.6. Medium to heavy traffic conditions were encountered, thus implying possible obstruction of the LoS component.

However, other scenarios that are more dedicated to specific safety-related ITS applications (i.e. not considered at all in classical cellular radio commu-

(a) Satellite view of the urban area. (b) Measurement location.

Figure 2.6: Pictures of the urban environment investigated during the Aalto 2009 measurement campaign (Google ©).

(a) Tx and Rx vehicles traveling in separate directions. (b) Road crossing scenario.

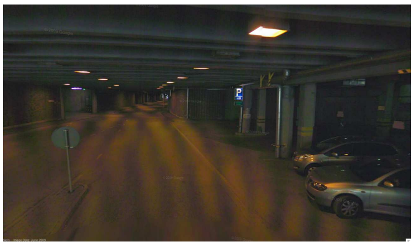

(c) Underground parking scenario.

Figure 2.7: Pictures of the specific scenarios investigated during the Aalto 2009 measurement campaign (Google ©).

nication systems) have also been investigated during this measurement campaign, namely

- When the Tx and Rx vehicles are traveling in either opposite or separate directions, as shown for example in Fig. 2.7(a). In that case, the Tx and Rx vehicles may be surrounded by distinct scattering environments that can vary over time independently one from another (with possible obstruction of the LoS component),

- When the Tx and Rx vehicles are approaching each other from perpendicular directions in road crossings, as shown in Fig. 2.7(b). The LoS contribution may then be obstructed during some time, such that the radio propagation channel consists only of contributions stemming from the surrounding scattering environment,

- When the Tx and Rx vehicles are traveling in underground (tunnel-like) parkings, as shown in Fig. 2.7(c). These are likely a rich scattering environment, owing to multiple reflections and waveguiding propagation effects (on walls, ceilings, other vehicles, metallic structures as ventilation systems, etc.).

The vehicles' speed was in all cases ranging from 5 to 20 km/h, while the inter-vehicle distance varied between 10 and 300 m, depending on the traffic conditions and the investigated environment.

2.4 Measured data

At the output of the channel sounder, we obtain time-varying complex wideband $N_{\mathrm{r}} \times N_{\mathrm{t}}$ matrices, which can be denoted as

$$\mathbf{H}(\tau_k\,;\, nt_{\mathrm{rep}}), \tag{2.2}$$

where $k = 0, ..., K-1$ and $n = 0, ..., N-1$ are the delay and time indices, respectively. The equivalent TFs $\mathbf{G}(f\,;\,t)$ can then be calculated by taking the one-dimensional Fourier transform of the IRs in the delay domain, namely

$$\mathbf{G}(f\,;\,t) = \int_{-\infty}^{+\infty} \mathbf{H}(\tau\,;\,t)e^{-j2\pi\tau f}d\tau. \tag{2.3}$$

In that case, note that the frequency resolution is given by $f_s = BW/K$ (with $K = 510$). Furthermore, the total number of recorded snapshots N depends on the duration length of each individual measurement run (which can vary from one route to another).

CHAPTER 3
Non-stationarity of MIMO vehicular channels

Real-world vehicular radio propagation channels can change very rapidly, owing to the high mobility of the Tx and Rx vehicles as well as of the scatterers located in the surrounding environment. This time-varying nature will impact significantly the spatial structure of the multipath components, whether it be in terms of magnitudes, propagation delays, Doppler frequency shifts, AoDs and AoAs, etc. As a consequence, the WSS-US-H assumption can no longer be fulfilled infinitely over all dimensions but only locally, within short bounded time, frequency bandwidth and space intervals.

When these stationarity intervals are large enough, then wireless communication systems can take advantage of them by estimating the statistics of the underlying radio propagation channel at the Rx side and feed them back to the Tx side so that it can adapt its transmission scheme accordingly. Nevertheless, such adaptive mechanisms are not possible when the stationarity regions are too small, as these statistics would be outdated when fed back to the Tx side (the current statistics of the radio propagation channel having indeed changed again in the meantime) [27, 92, 93, 94]. In that case, only blind transmission is possible, hence yielding important degradations in the communication system performances. The accurate understanding and modeling of the vehicular radio propagation channel non-stationarities are thus crucial, e.g. for the design optimization of such adaptive wireless communication systems.

For that purpose, Section 3.1 first characterizes the frequency- and time-dependent behavior of the spatial structure of vehicular MIMO radio propagation channels, which is shown to successfully detect significant changes occuring in the scattering environment surrounding the Tx and Rx vehicles. Hence, the CMD is considered in Section 3.2 as a meaningful measure of the non-stationary behavior of MIMO radio propagation channels, based on the amount of change in their spatial structures over both time and frequency. Then, Section 3.3 assesses the validity of the WSS and US assumptions for measured vehicular radio propagation channels, while a statistical characterization of stationarity frequency bandwidths and time durations is also provided. Finally, Section 4.3 provides a discussion and a conclusion.

3.1 Frequency- and time-varying MIMO spatial structure

As already mentioned in Section 1.1.4, one of the most important features of MIMO radio propagation channels concerns their spatial structure, which is governed by the radio wave propagation mechanisms that occur between the Tx and Rx sides. It is therefore meaningful to characterize the non-stationary behavior of MIMO radio propagation channels by measuring the amount of change in their spatial correlation matrices over time and frequency.

In the following, full spatial correlation matrices as given by Eq. (1.25) are assumed to be separable, so that only changes in the Tx and Rx spatial matrices will be considered.

3.1.1 Estimating spatial correlation matrices

Spatial correlation matrices have theoretically to be estimated over an infinite number of snapshots and frequency bins, as shown in Eqs. (1.26) and (1.27). This is nevertheless not possible when regarding radio propagation channels that are varying over both time and frequency. In that case, spatial correlation matrices have indeed to be calculated over finite subsets, using a sliding average window within which the WSS-US assumption is *a priori* supposed to locally hold. As depicted in Fig. 3.1,

- The sliding average window spans over L frequency bins and is centered on the indices $k_f \in \{1, \cdots, \left\lfloor \frac{K-L/2}{\Delta_f} \right\rfloor\}$, Δ_f corresponding here to the frequency shift between two consecutive estimates of the Tx or Rx spatial correlation matrices,
- The sliding average window spans over M snapshots and is centered on the indices $k_t \in \{1, \cdots, \left\lfloor \frac{N-M/2}{\Delta_t} \right\rfloor\}$, Δ_t corresponding here to the time shift between two consecutive estimates of the Tx or Rx spatial correlation matrices,

The frequency- and time-dependent spatial correlation matrices, as defined by Eqs. (1.26) and (1.27), can thus be rewritten as

$$\widehat{\mathbf{R}}_{\mathrm{Tx}}(k_f\,;\,k_t) = \frac{1}{LM} \sum_{k'=(k_f-1)\Delta_f+1}^{(k_f-1)\Delta_f+L} \; \sum_{n'=(k_t-1)\Delta_t+1}^{(k_t-1)\Delta_t+M} \mathbf{G}^{\mathrm{T}}(k'\,;\,n')\mathbf{G}^{*}(k'\,;\,n'), \tag{3.1}$$

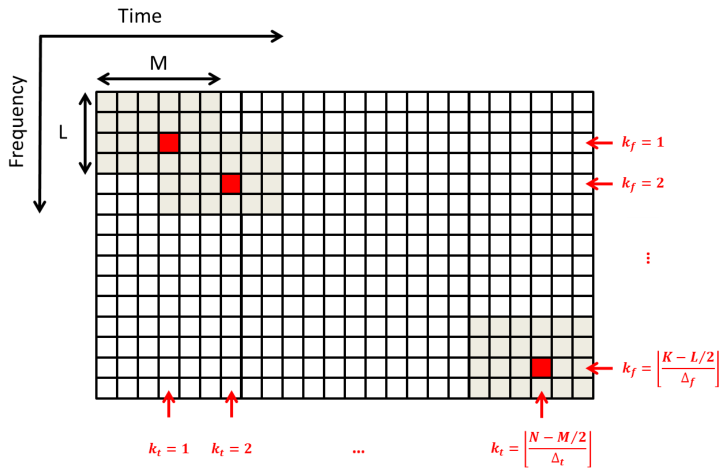

Figure 3.1: Principle of the frequency-time sliding average window used for the estimation of the spatial correlation matrices. The window sizes in frequency and time are chosen as $M = 6$ snapshots and $L = 4$ frequency bins, respectively. The corresponding frequency and time shifts are set to $\Delta_f = L/2$ and $\Delta_t = M/2$, respectively.

$$\widehat{\mathbf{R}}_{\mathrm{Rx}}(k_f\,;\,k_t) = \frac{1}{LM} \sum_{k'=(k_f-1)\Delta_f+1}^{(k_f-1)\Delta_f+L} \sum_{n'=(k_t-1)\Delta_t+1}^{(k_t-1)\Delta_t+M} \mathbf{G}(k'\,;\,n')\mathbf{G}^{\mathrm{H}}(k'\,;\,n'). \tag{3.2}$$

The dimensions M and L of the sliding average window used for the estimation of the spatial correlation matrices define the minimum stationarity regions in time and frequency over which the WSS and the US assumptions are assumed to hold, respectively. In other words, stationarity regions in time and frequency should be at least as large as the dimensions M and L of the sliding average window, in order to ensure that the spatial correlation matrices are estimated over regions where the statistics of the underlying radio propagation channels remain constant. Moreover, note that the elements on the main diagonal of the spatial correlation matrix correspond to the average power transmitted or received on each antenna, while the off-diagonal elements give the correlation between the corresponding Tx-Rx antenna pairs.

Note also that passing from Eqs. (1.26) and (1.27) to Eqs. (3.1) and (3.2), respectively, relies on the fact that the time-varying TFs are assumed to be ergodic. In that case, all their moments can indeed be determined from each single realization taken within the sliding average window, with probability one

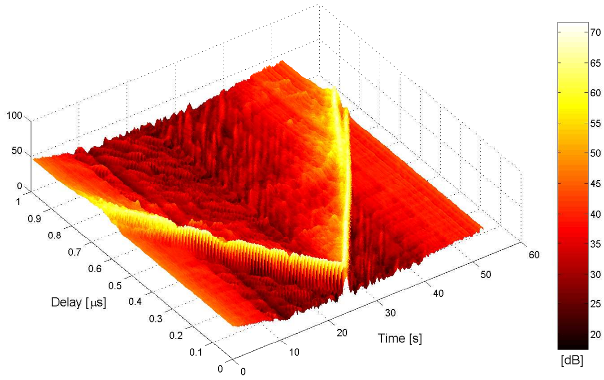

(a) Time-varying PDPs.

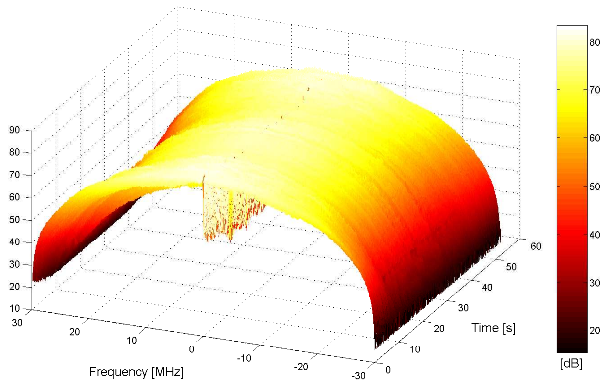

(b) Time-varying PSDs.

Figure 3.2: Time-varying PDPs and PSDs, for one route taken from the Aalto 2009 measurement campaign. The Tx and Rx vehicles are traveling in opposite directions, with occasional obstruction of the LoS component.

[95]. In other words, the expected value $\mathrm{E}\{\cdot\}$ (which corresponds to an ensemble average) can be safely replaced by a time average. Throughout this thesis, this ergodicity assumption will therefore be assumed to always hold (though it will not be tested). As a consequence, the whole analysis regarding the validity of the WSS assumption will depend on the fact that the time-varying TFs are effectively ergodic.

3.1.2 Example and general comments

Let us now consider the outcome of the spatial correlation matrix estimation, for one examplary route taken from the Aalto 2009 measurement campaign located in a campus environment with almost no traffic at all. The Tx and Rx vehicles are traveling in a bend in opposite directions and pass each other at time $t = 23.5$ s. Note also that since the Tx and Rx vehicles start initially at each side of the bend, the LoS component is obstructed at the beginning (i.e. between times $t = 0$ and $t = 9.5$ s) as well as at the end (i.e. between times $t = 41.5$ and $t = 52$ s) of the measurement run. Fig. 3.2 shows the corresponding time-varying PDPs and PSDs, which are both almost “symmetric” with respect to the time instant at which the two vehicles pass each other (due to the special configuration of this measurement route).

As shown from the time-varying PSDs in Fig. 3.2(b), the received power decreases abruptly at both the lower and upper edges of the measurement bandwidth, owing to limited bandwidth of the measurement system as well as the non-flatness of the frequency response of the PN sequence which is used as transmit signal. Note that this behavior will impact significantly the estimation of the spatial structure of the underlying MIMO radio propagation channel, and hence the modeling of its non-stationary behavior over frequency (more specifically on the edges of the measurement bandwidth), as further discussed in Section 3.4.1.

Fig. 3.3 shows the temporal evolution of the eigenmodes associated with the three strongest eigenvalues of the Rx spatial correlation matrices, estimated for a given frequency $f = 19.9$ MHz. Since the LoS component dominates over the radio wave propagation, the angular spectrum at the Rx side is highly directive, with only a single AoA (in the direction of the LoS component). In other words, all the Rx antenna elements that look towards the Tx side experience the same radio wave propagation conditions and are strongly correlated. Before (resp. after) the two vehicles pass each other, these elements are located at the frontside (resp. backside) of the Rx antenna array (see Table 2.2 for the link to antenna element mapping and Fig. 2.2(b) for the position of the elements in the antenna array, respectively). The transition between these two antenna configurations occurs exactly when the Tx and Rx vehicles pass each other and can be well identified from the spatial structure of the underlying MIMO radio propagation channel.

Moreover, since these eigenmodes have strongly correlated amplitudes (note that they are orthogonal only owing to their phase differences), they will suffer simultaneously from the same deep fades. This is typically the case between times $t = 0$ and $t = 9.5$ s as well as between times $t = 41.5$ and $t = 52$ s, when the LoS component is obstructed and no strong component dominates over the radio wave propagation any more. There are then only numerous multi-bounced (low-power) interactions with scatterers widely spread in the environment between the Tx and Rx sides, what leads to large angu-

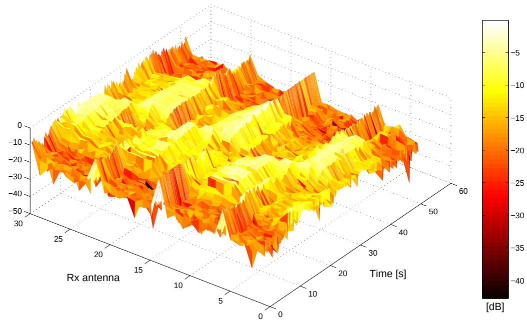

(a) First eigenmode.

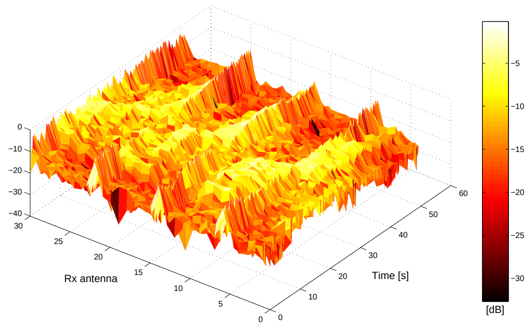

(b) Second eigenmode.

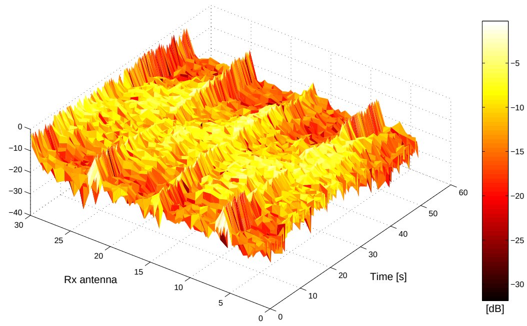

(c) Third eigenmode.

Figure 3.3: Time-varying eigenmodes of the spatial correlation matrices, at frequency $f = 19.9$ MHz. The Tx and Rx vehicles are traveling in opposite directions, with occasional obstruction of the LoS component. $L = M = 20$.

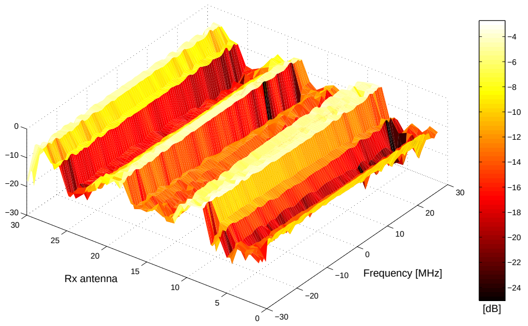

(a) First eigenmode.

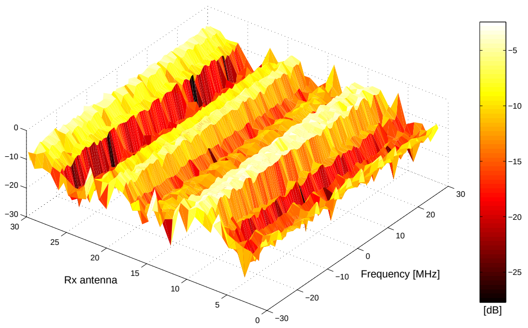

(b) Second eigenmode.

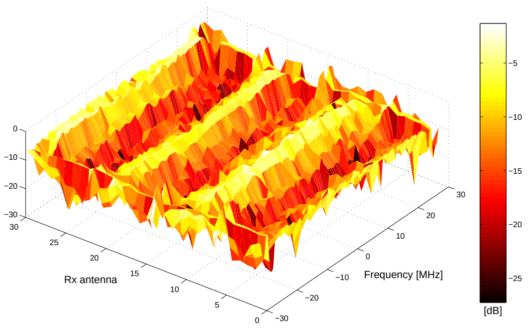

(c) Third eigenmode.

Figure 3.4: Frequency-varying eigenmodes of the spatial correlation matrix, at time $t = 18$ s. The Tx and Rx vehicles are traveling in opposite directions, with occasional obstruction of the LoS component. $L = M = 20$.

lar spreads at the link end. As a consequence, the received power impinges from all possible directions (i.e. the angular spectrum is in that case almost isotropic), such that the correlation decreases. The spatial correlation matrix becomes then increasingly similar to the identity matrix. Hence, the spatial structure of the underlying MIMO radio propagation channel is also able to capture accurately transitions between consecutive LoS and NLoS situations.

On the other hand, Fig. 3.4 shows the variations over frequency of the eigenmodes associated with the three strongest eigenvalues of the Rx spatial correlation matrices, estimated at time $t = 18$ s (i.e. before the Tx and Rx vehicles pass one another). The elements located at the frontside of the Rx antenna array collect the strongest power, which remains approximately constant over the whole measurement bandwidth (excepted on its edges, owing to effects due to the limited bandwidth of the measurement system and the PN sequence). Note that, although not described here, similar observations could be obtained for the spatial correlation matrices estimated at the Tx side.

3.2 Stationarity assessment based on the MIMO spatial structure

As observed from the examplary measurement route in Section 3.1, vehicular MIMO radio propagation channels are strongly frequency- and time-dependent. Noticeable variations are observed in their spatial structures, which can be related to changes that are occuring in the scattering environment surrounding the Tx and Rx vehicles.

The validity of the WSS and US assumptions can therefore be assessed by measuring the amount of change in the spatial structure of adjacent spatial correlation matrices (shifted by Δk_t and Δk_f in time and frequency, respectively). Indeed, if two spatial correlation matrices are similar enough, then the underlying fading process has the same statistical properties (i.e. the underlying MIMO radio propagation channel can be considered as stationary).

3.2.1 Correlation matrix distance

In [47, 48], the CMD was introduced as a metric for the characterization of the amount of change between two arbitrary time- and frequency-dependent spatial correlation matrices $\mathbf{R}(k_f\,;\,k_t)$ and $\mathbf{R}(k_f+\Delta k_f\,;\,k_t+\Delta k_t)$, i.e.

$$\begin{aligned} d_{\text{corr}}(k_f,k_t\,;\,k_f+\Delta k_f,k_t+\Delta k_t) &= 1-\cos(\phi) \\ &= 1-\frac{\text{tr}\left\{\mathbf{R}(k_f\,;\,k_t)\mathbf{R}(k_f+\Delta k_f\,;\,k_t+\Delta k_t)\right\}}{\left\|\mathbf{R}(k_f\,;\,k_t)\right\|_F\left\|\mathbf{R}(k_f+\Delta k_f\,;\,k_t+\Delta k_t)\right\|_F}, \end{aligned} \tag{3.3}$$

where $\text{tr}\left\{\cdot\right\}$ and $\left\|\cdot\right\|_F$ are the trace operator and the Frobenius norm, respectively. The CMD is based on the angle ϕ between the two spatial correlation matrices that are being compared and can be interpreted as the measure of their orthogonality, i.e. how much their respective signal subspaces overlap, independently on changes in the received power. The CMD ranges between zero when the compared spatial correlation matrices are identical (up to a scaling factor) and one when they are completely different (i.e. uncorrelated).

Ideally, true spatial correlation matrices, as given by Eq. (1.27), would be required in order to estimate the CMD (i.e. the non-stationary behavior of the underlying radio propagation channels) as accurately as possible. Nevertheless, this is in practice not possible since they have to be estimated over short sliding average windows over frequency and time (with dimensions L and M, respectively). As a result, as we do not know *a priori* how much the WSS and US assumptions remain valid, these dimensions M and L have to be chosen carefully. In the following, we will use $L = 20$ frequency bins (i.e. 2.35 MHz wide) and $M = 20$ snapshots (i.e. 0.30 s long) in the frequency and time domains, respectively (further details about the impact of the dimensions of the sliding average window on the estimation of the CMD can be found Section 3.2.3). Note that these values correspond to the dimensions of the minimum stationarity region over which the WSS-US assumption is assumed to locally hold, i.e. the estimated stationarity frequency and time intervals have to be always larger than these dimensions.

3.2.2 Examples and general comments

Let us now consider the frequency- and time-dependent CMD for the exemplary route described in Section 3.1.2, when the Tx and Rx vehicles are traveling in opposite directions (with occasional obstruction of the LoS component).

Fig. 3.5 shows only the case where the Tx and Rx vehicles are getting closer one from another (between times $t = 0$ and $t = 23.5$ s). Two representative (equivalent baseband) frequencies are also considered, i.e. at the center (i.e. $f = 2$ MHz) and at the upper edge of the measurement bandwidth (i.e. $f = 23$ MHz), respectively.

When there is a strong LoS component between the Tx and Rx sides, the CMD remains almost constant over the whole measurement bandwidth, as it is

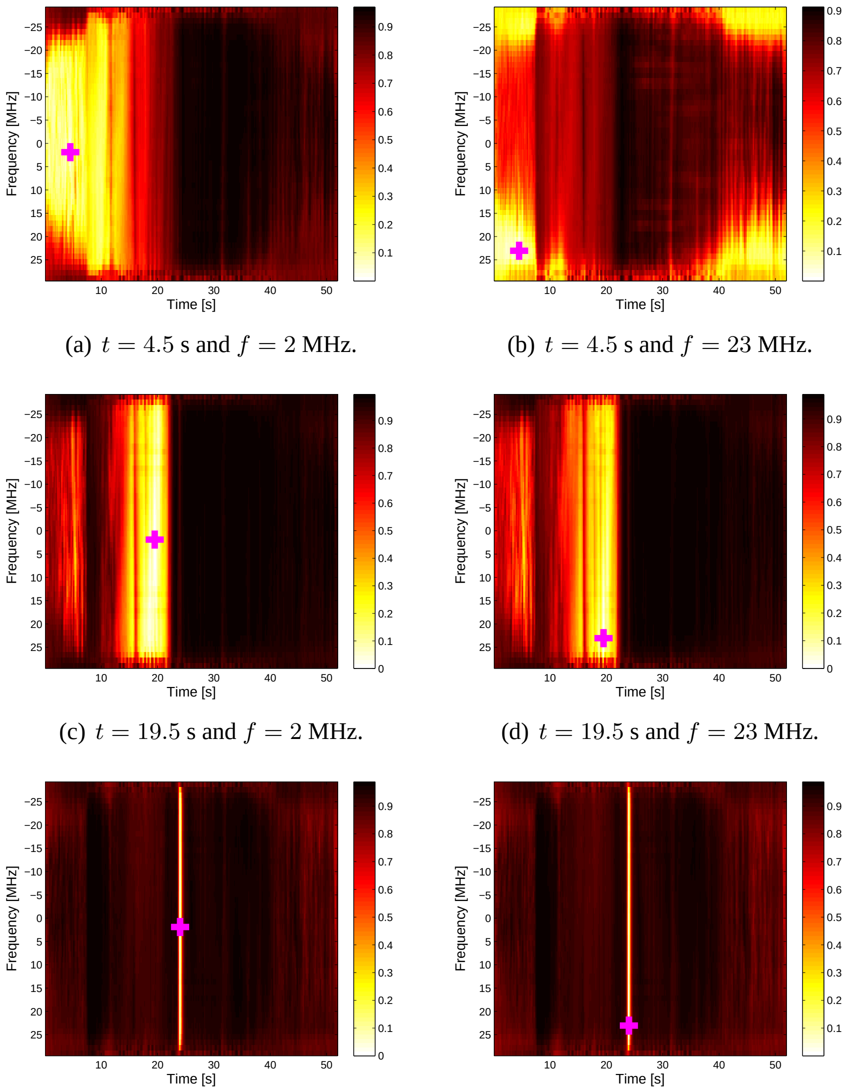

(a) $t = 4.5$ s and $f = 2$ MHz. (b) $t = 4.5$ s and $f = 23$ MHz.

(c) $t = 19.5$ s and $f = 2$ MHz. (d) $t = 19.5$ s and $f = 23$ MHz.

(e) $t = 23.5$ s and $f = 2$ MHz. (f) $t = 23.5$ s and $f = 23$ MHz.

Figure 3.5: Frequency- and time-dependent CMD estimated at the Rx side. The magenta cross indicates the frequency and time at which a reference spatial correlation matrix was estimated and compared with those estimated at other frequencies and times. The Tx and Rx vehicles are traveling in opposite directions, with occasional obstruction of the LoS component. $L = M = 20$ and $\Delta_f = \Delta_t = 10$, respectively.

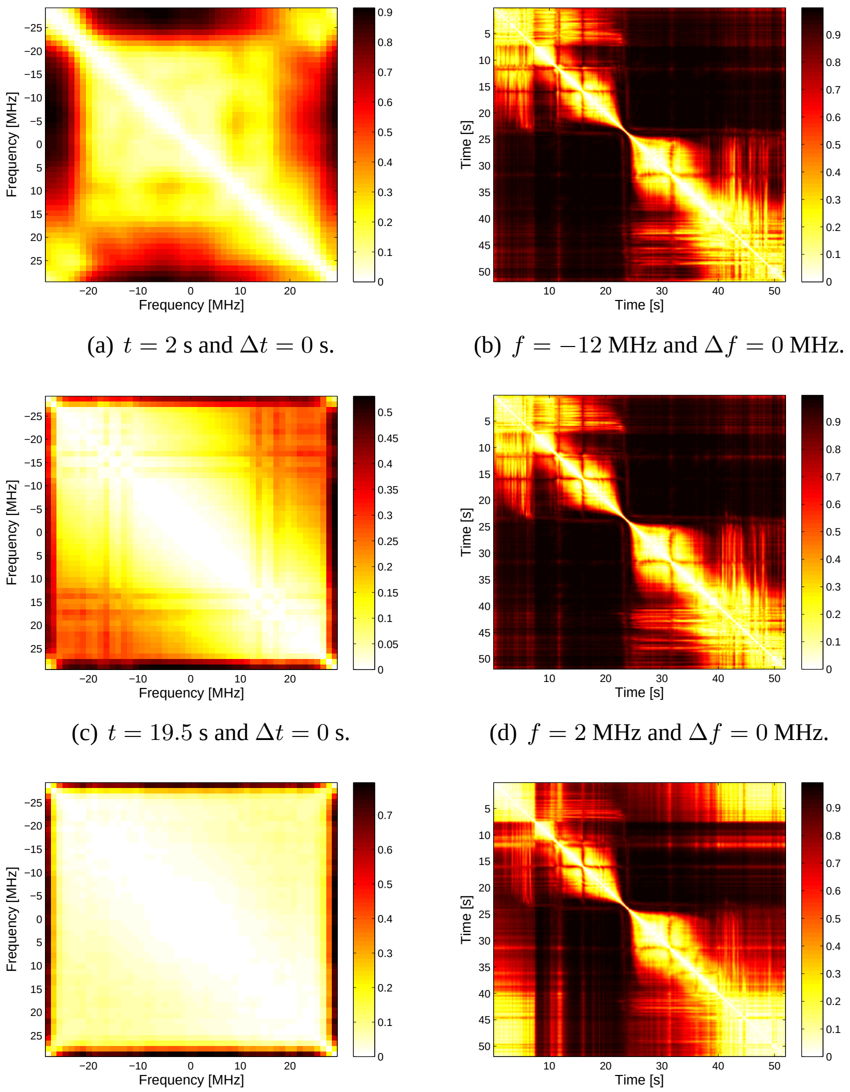

(a) $t = 2$ s and $\Delta t = 0$ s.

(b) $f = -12$ MHz and $\Delta f = 0$ MHz.

(c) $t = 19.5$ s and $\Delta t = 0$ s.

(d) $f = 2$ MHz and $\Delta f = 0$ MHz.

(e) $t = 23.5$ s and $\Delta t = 0$ s.

(f) $f = 23$ MHz and $\Delta f = 0$ MHz.

Figure 3.6: Frequency- and time-dependent CMD estimated at the Rx side as a function of the frequency (left) and time (right) shifts. The Tx and Rx vehicles are traveling in opposite directions, with occasional obstruction of the LoS component. $L = M = 20$ and $\Delta_f = \Delta_t = 10$, respectively.

shown in Figs. 3.7(c) $-$ 3.7(d) between times $t = 10$ and $t = 23.5$ s. In other words, the spatial structure of the MIMO radio propagation channel does not change significantly with the frequency shift Δk_f. Spatial correlation matrices estimated at the frequencies k_f and $k_f + \Delta k_f$ are then almost identical. This is due to the fact that the LoS component definitely dominates over the other radio wave propagation mechanisms (and equally affects all the signal frequencies), such that interactions with the scatterers located in the surrounding environment are almost negligible. On the other hand, when the LoS component becomes obstructed, i.e. between times $t = 0$ and $t = 10$ s as shown in Figs. 3.7(a) $-$ 3.7(b), then the radio wave propagation is dominated by the interactions with the surrounding scattering environment. As a consequence, the signal frequencies may be affected by different multipath components, such that the spatial structure of the MIMO radio propagation channel can change significantly with the frequency shift Δk_f.

Besides, variations in the spatial structure of the MIMO radio propagation channel are much more abrupt over time than over frequency and can be clearly related to significant changes occuring in the scattering environment surrounding the Tx and Rx vehicles. Figs. 3.7(a) $-$ 3.7(b) show indeed that a stationarity region can be identified between times $t = 0$ and $t = 10$ s, when the Tx and Rx vehicles are in a NLoS situation (when they are at each side of the bend). Similarly, another one can be identified between times $t = 10$ and $t = 23$ s, when the LoS component is not obstructed any more and the Tx and Rx vehicles are approaching one from another, as shown in Figs. 3.7(c) $-$ 3.7(d). Moreover, the closer the Tx and Rx vehicles (typically when they are passing one another, e.g. at time instant $t = 23.5$ s), the faster the spatial structure of the underlying MIMO radio propagation channel is likely to change. In other words, high CMD values can in that case be achieved within short time intervals (i.e. between spatial correlation matrices estimated at very close time instants), what yields the shortest stationarity regions, as represented in Figs. 3.7(e) $-$ 3.7(f).

Noteworthy also is the fact that even though the scenario is almost “symmetric” with respect to the time instant at which the two vehicles pass each other, this is clearly not the case for the estimated CMD. Fig. 3.5 shows that the spatial structure of the MIMO radio propagation channel is completely different when the Tx and Rx vehicles are approaching (between times $t = 0$ and $t = 23.5$ s) or are moving away one from another (between times $t = 23.5$ and $t = 52.5$ s), with however an exception on the edges of the measurement bandwidth when the LoS is obstructed, see Fig. 3.7(b). This is due to the fact that the relative orientation of the Tx and Rx antenna patterns can completely change over time: indeed, when the vehicles are approaching (resp. moving away) one from another, antenna elements located at the frontside (resp. backside) of the Tx and Rx antenna arrays are facing one another (it was already observed in Fig. 3.3 from the time evolution of their strongest eigenmodes). Hence, the comparison between spatial correlation matrices with these two antenna array configurations will lead to large CMD values.

Alternatively, the variations of the CMD can also be considered over frequency or time only. The left (resp. right) column of Fig. 3.6 represents to the variations of the CMD versus the frequency (resp. time) shift Δk_f (resp. Δk_t), taken at different time instants (resp. frequencies). Values on the diagonal correspond in that case to zero frequency (resp. time) shifts (i.e. when spatial correlation matrices are compared to themselves), such that the CMD is zero. Off-diagonal elements represent the CMD estimated between adjacent spatial correlation matrices taken at distinct frequencies or time instants (the further from the diagonal, the larger the shift Δk_f or Δk_t, respectively). As it can be observed, vehicular MIMO radio propagation channels have spatial structures that can experience significant changes within very short time intervals, while they noticeably remain approximately constant over the whole 60 MHz measurement bandwidth. It can therefore be already concluded from this examplary measurement route that vehicular radio propagation channels violate the WSS assumption much more violated than the US assumption.

3.2.3 Definition of the minimum stationarity regions

Fig. 3.7 shows the impact of the dimensions of the sliding average window on the estimation of the frequency- and time-dependent CMD

- For small dimensions of the sliding average window, e.g. when $M = 4$ snapshots (i.e. 0.06 s long) and $L = 4$ frequency bins (i.e. 0.47 MHz wide), estimated spatial correlation matrices are clearly ill-conditioned (especially when large antenna arrays are considered at the Tx or Rx side) and are therefore significantly different from the theoretical expectations. In other words, even consecutive spatial correlation matrices (in the time or frequency domain) are found to be significantly different one from another. Hence, the estimated frequency- and time-dependent CMD represents harsh variations of the spatial structure of the underlying MIMO radio propagation channel over time and frequency, which do definitely not represent accurately the ”true” ones,

- As the dimensions M and L of the sliding average window increase, e.g. when $M = 20$ snapshots (i.e. 0.30 s long) and $L = 20$ frequency bins (i.e. 2.35 MHz wide), estimated spatial correlation matrices are

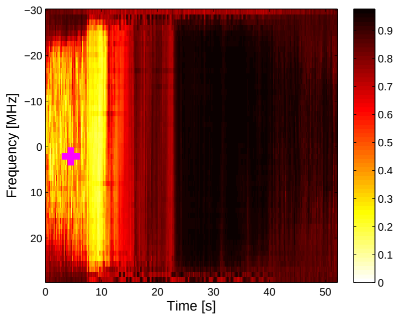

(a) $M = L = 4$ and $\Delta_f = \Delta_t = 10$.

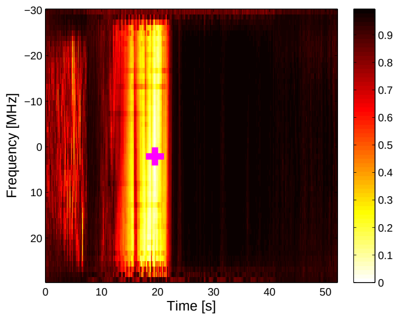

(b) $M = L = 4$ and $\Delta_f = \Delta_t = 10$.

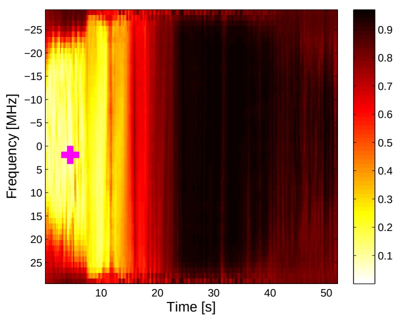

(c) $M = L = 20$ and $\Delta_f = \Delta_t = 10$.

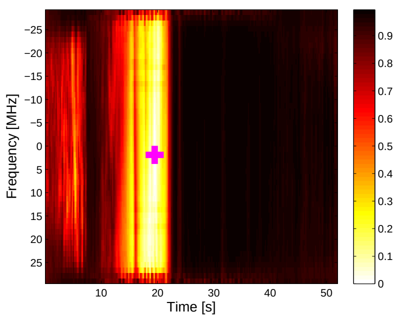

(d) $M = L = 20$ and $\Delta_f = \Delta_t = 10$.

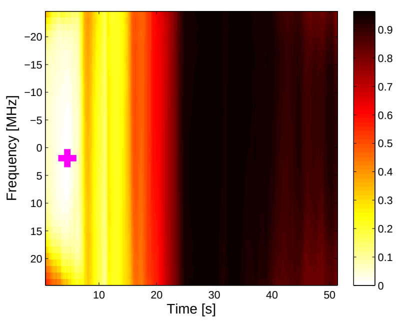

(e) $M = L = 100$ and $\Delta_f = \Delta_t = 10$.

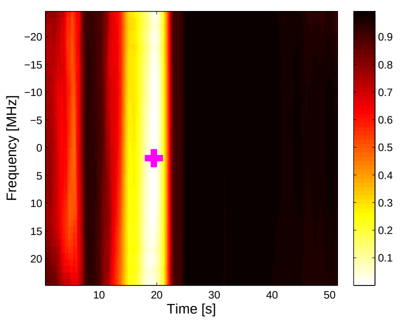

(f) $M = L = 100$ and $\Delta_f = \Delta_t = 10$.

Figure 3.7: Frequency- and time-dependent CMD estimated at the Rx side, for different dimensions of the sliding average window. The two reference spatial correlation matrices were taken at $t = 4.5$ s and $f = 2$ MHz and $t = 19.5$ s and $f = 2$ MHz, respectively. The Tx and Rx vehicles are traveling in opposite directions, with occasional obstruction of the LoS component.

better conditioned. They become in that case closer from their theoretical expectations, such that the frequency- and time-dependent CMD represents smoother (and more reliable) variations of the spatial structure of the underlying MIMO radio propagation channel over time and frequency,

- Finally, for large dimensions of the sliding average window, e.g. when $M = 100$ snapshots (i.e. 1.50 s long) and $L = 100$ frequency bins (i.e. 11.76 MHz wide), estimated spatial correlation matrices are clearly well-conditioned. However, the fading process is in that case likely to change over much shorter time (resp. frequency) scales, such that the WSS-US assumption may no longer be fulfilled within the sliding average window. Besides, consecutive spatial correlation matrices in time (resp. frequency) are all more or less significantly correlated, since they are estimated using the same snapshots (resp. frequency bins). As a result, the spatial structure of the underlying MIMO radio propagation channel may remain unchanged over very large time (resp. frequency) intervals. In other words, the frequency- and time-dependent CMD does no longer accurately represent the ”true” variations of its spatial structure over time and frequency. Moreover, note that stationarity regions shorter than the sliding average window cannot be estimated (as the dimensions M and L of the sliding average window define the minimum stationarity region over which the WSS and US assumptions is assumed to locally hold, respectively).

As a consequence, a trade-off must be taken into account between the accuracy of the spatial correlation matrices estimates (the dimensions M and L have to be large enough, such that the spatial correlation matrices are well-conditioned) and the local fulfillment of the WSS-US assumption (i.e. the dimensions M and L do not have to be too large, since the fading behavior has to remain unchanged over the time and frequency span of the sliding average window, respectively). This is the reason why sliding average windows with dimensions $L = 20$ frequency bins and $M = 20$ snapshots are used in order to estimate spatial correlation matrices, as previously mentioned in Section 3.2.1.

3.2.4 Identifying frequency and time stationarity intervals

Since the CMD is a bounded metric, indicative threshold values can be defined in order to identify stationarity time durations and frequency bandwidths over which the WSS and US assumptions are locally fulfilled, respectively.

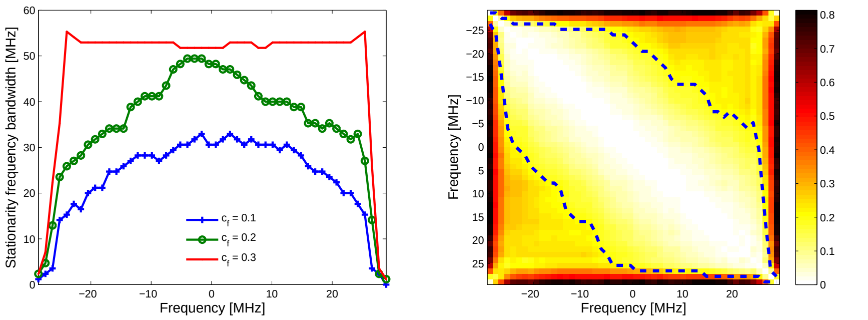

(a) Stationarity frequency bandwidth for different thresholds c_f.

(b) Frequency-dependent CMD (at time $t = 37.5$ s) and the corresponding stationarity frequency bandwidth for $c_f = 0.2$.

Figure 3.8: Stationarity frequency bandwidth for different thresholds c_f. The Tx and Rx vehicles are traveling in opposite directions with occasional obstruction of the LoS component. $L = M = 20$ and $\Delta_f = \Delta_t = 10$, respectively.

Stationarity frequency bandwidth

For a given time instant and a given frequency bin, the stationarity frequency bandwidth is defined as the maximum (connected) frequency bandwidth over which the CMD remains below some indicative threshold value c_f, such that

$$F_{\text{s}}(k_f\,;\,k_t) = [k_{f,\text{max}}(k_f\,;\,k_t) - k_{f,\text{min}}(k_f\,;\,k_t)]\,\Delta_f\,f_s, \tag{3.4}$$

where $k_{f,\text{min}}(k_f\,;\,k_t)$ and $k_{f,\text{max}}(k_f\,;\,k_t)$ are the frequency-varying lower and upper bounds of the stationarity frequency bandwidth, respectively, i.e.

$$\begin{aligned} k_{f,\text{min}}(k_f\,;\,k_t) &= \underset{-k_f \leq \Delta k_f \leq 0}{\arg\max}\; d_{\text{corr}}\left(k_f, k_t\,;\,k_f, k_t\right) \geq c_f \\ k_{f,\text{max}}(k_f\,;\,k_t) &= \underset{0 \leq \Delta k_f \leq \left\lfloor \frac{K-L}{\Delta_f} \right\rfloor - k_f}{\arg\min}\; d_{\text{corr}}\left(k_f, k_t\,;\,k_f + \Delta k_f, k_t\right) \geq c_f. \end{aligned}$$

These stationarity frequency bandwidth can therefore be interpreted as a coherence bandwidth that would be estimated from frequency- and time-dependent spatial correlation matrices. In other words, two different frequencies of the transmitted signal (when taken within the same stationarity frequency bandwidth) do experience comparable (or correlated) spatial structures of the underlying MIMO radio propagation channel.

Fig. 3.8(a) shows the frequency-dependent stationarity frequency bandwidth estimated at time $t = 37.5$ s using different thresholds c_f for the same examplary route as previously. The less restrictive the threshold c_f is, the more sensitive the stationarity frequency bandwidths are to small changes in the spatial structures of MIMO radio propagation channels. On the other hand, Fig. 3.8(b) shows that reasonable estimates of the stationarity frequency bandwidth can be obtained for $c_f = 0.2$, in good agreement with what was reported in [96]. The smooth variations of the estimated stationarity frequency bandwidth over frequency are due to the fact that the spatial correlation matrices are estimated over sliding average windows that are wide enough (using L consecutive frequency bins) with respect to the number of measured frequency bins.

Stationarity time intervals

Similarly, the stationarity time duration is defined as the maximum (connected) time interval over which the CMD remains below some indicative threshold value c_t, such that

$$T_{\text{s}}(k_f\,;\,k_t) = [k_{t,\text{max}}(k_f\,;\,k_t) - k_{t,\text{min}}(k_f\,;\,k_t)]\,\Delta_t\,t_{\text{rep}}, \tag{3.5}$$

where $k_{t,\text{min}}(k_f\,;\,k_t)$ and $k_{t,\text{max}}(k_f\,;\,k_t)$ are the time-varying lower and upper bounds of the stationarity time interval, respectively, i.e.

$$\begin{aligned} k_{t,\text{min}}(k_f\,;\,k_t) &= \underset{-k_t \leq \Delta k_t \leq 0}{\arg\max}\; d_{\text{corr}}\left(k_f, k_t\,;\,k_f, k_t + \Delta k_t\right) \geq c_t \\ k_{t,\text{max}}(k_f\,;\,k_t) &= \underset{0 \leq \Delta k_t \leq \left\lfloor \frac{N-M}{\Delta_t} \right\rfloor - k_t}{\arg\min}\; d_{\text{corr}}\left(k_f, k_t\,;\,k_f, k_t + \Delta k_t\right) \geq c_t. \end{aligned}$$

These stationarity time interval can therefore be interpreted as a coherence time that would be estimated from frequency- and time-dependent spatial correlation matrices. In other words, signals transmitted at two different time instants (when taken within the same stationarity time interval) do experience comparable (or correlated) spatial structures of the underlying MIMO radio propagation channel.

Fig. 3.9(a) shows the time-varying stationarity time duration estimated at frequency $f = -24$ MHz using different thresholds c_t for the same examplary route as previously. Again, the less restrictive the threshold c_t is, the more sensitive the stationarity time intervals are to small changes in the spatial structures of MIMO radio propagation channels. Fig. 3.9(b) shows that reasonable estimates of the stationarity time duration can be obtained for $c_t = 0.2$, in good agreement with what is reported in [47, 48]. Moreover, the jitter is due to the

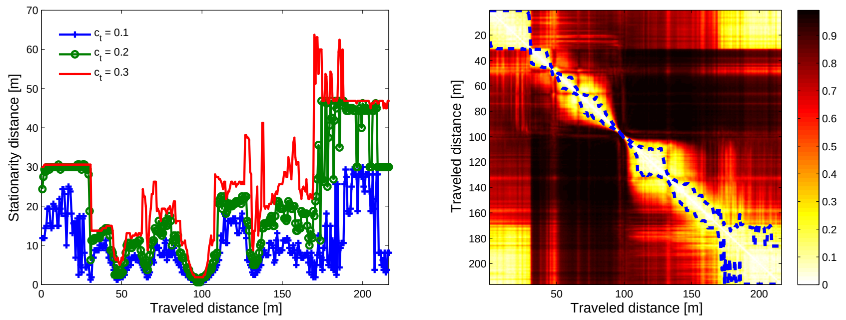

(a) Stationarity distance for different thresholds c_t.

(b) Time-dependent CMD (at frequency $f = -24$ MHz) and the corresponding stationarity distance for $c_t = 0.2$.

Figure 3.9: Stationarity distance for different thresholds c_t. The Tx and Rx vehicles are traveling in opposite directions, with occasional obstruction of the LoS component. $L = M = 20$ and $\Delta_f = \Delta_t = 10$, respectively.

fact that the spatial correlation matrices used for the estimation of the CMD are estimated over short sliding average windows (using only M consecutive snapshots in the time domain). The stationarity time duration should rather remain constant for each time instant within a same stationarity region. In other words, the stationarity time duration should theoretically vary by blocks, with sharp transitions between two consecutive ones.

Since the stationarity time duration depends on the Tx and Rx vehicles' speed, it can equivalently be expressed in terms of traveled distance. Hence, stationarity distances can equivalently be defined as

$$D_{\mathrm{s}}(k_f\,;\,k_t) = v(k_t)\,T_{\mathrm{s}}(k_f\,;\,k_t), \tag{3.6}$$

where $v(k_t)$ is the speed of the vehicles at the time instant k_t. However, since the exact vehicles' speed was not available at each time instant during the measurement campaign, $v(k_t)$ can be replaced in the previous relationship by its average value $\bar{v}$.

3.3 Empirical analysis of the non-stationary behavior

So far, we have shown that the non-stationary behavior of MIMO radio propagation channels can be successfully detected and characterized based on their spatial structure. However, only one single measurement route was up to now considered as an examplary case. Hence, this analysis can now be extended to the large data sets collected during the Aalto 2007 and 2009 measurement campaigns, in order to assess more generally the validity of the WSS and US assumptions in vehicular environments.

3.3.1 (In)-validity of the US assumption?

Fig. 3.10 shows how much the stationarity frequency bandwidth $F_\mathrm{s}(k_f\,;\,k_t)$ varies simultaneously over time and frequency. For that purpose, three examplary measurement scenarios are considered, with different temporal dynamics and scattering richness conditions, i.e. respectively

- When the Tx and Rx vehicles are traveling in a bend in opposite directions, in a campus environment with almost no traffic at all. They pass each other at time $t = 23.5$ s. The LoS component is obstructed at the beginning (i.e. between times $t = 0$ and $t = 9.5$ s) as well as at the end (i.e. between times $t = 41.5$ and $t = 52$ s) of the measurement run,

- When the Tx and Rx vehicles are traveling always in the same direction, in an open campus environment with light traffic conditions. The LoS component is obstructed by a van that comes between the Tx and Rx vehicles in the middle of the measurement run (i.e. between times $t = 30$ and $t = 65$ s),

- When the Tx and Rx vehicles are first traveling in the same direction, in a sub-urban environment with medium traffic conditions. Then, at time $t = 18$ s, each vehicle is taking a different direction when arriving at a fork in the road. The LoS component is then obstructed until the end of the measurement run.

As it can be observed, the richer the scattering environment surrounding the Tx and Rx vehicles, the smaller the stationarity frequency bandwidth $F_\mathrm{s}(k_f\,;\,k_t)$. When the radio wave propagation is dominated by a strong LoS component, then the different multipath components do indeed not have a significant impact on the transmitted signal. As a consequence, all the frequencies are affected by the same fading conditions, such that the stationarity frequency bandwidth $F_\mathrm{s}(k_f\,;\,k_t)$ spans almost the whole measurement bandwidth $B = 60$ MHz (note that even though the actual stationarity frequency bandwidth could be much larger, it is upper-bounded by this value). On the other hand, smaller (but still relatively high) stationarity frequency bandwidths are obtained in richer scattering environments. This is typically the case when the LoS component is obstructed, such that the radio wave propagation is in that case dominated by the numerous multipath components stemming from the same scat-

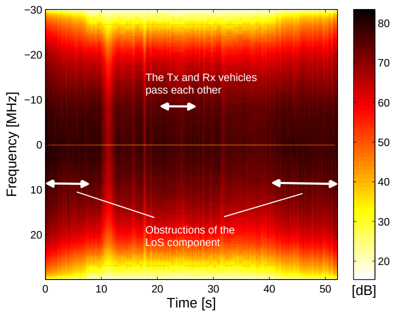

(a) Time-varying PSDs for opposite traveling directions.

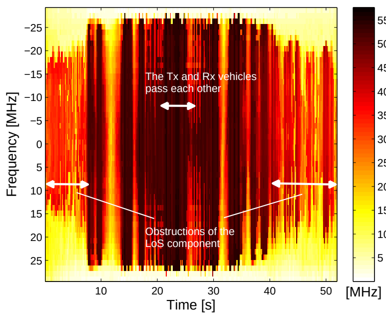

(b) Stationarity frequency bandwidth for opposite traveling directions.

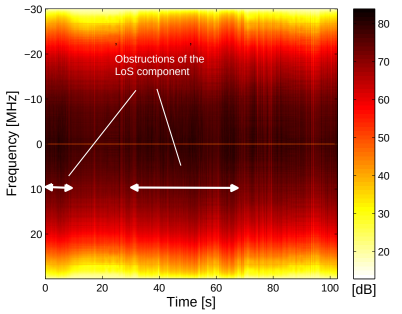

(c) Time-varying PSDs with occasional obstruction of the LoS component.

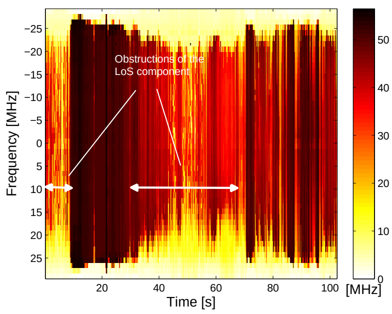

(d) Stationarity frequency bandwidth with occasional obstruction of the LoS component.

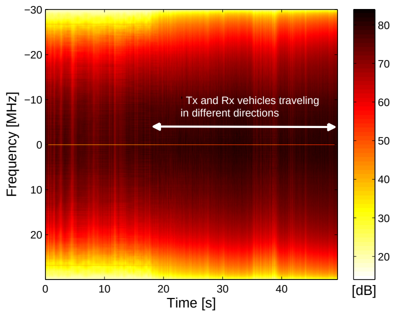

(e) Time-varying PSDs for different traveling directions (NLoS situation).

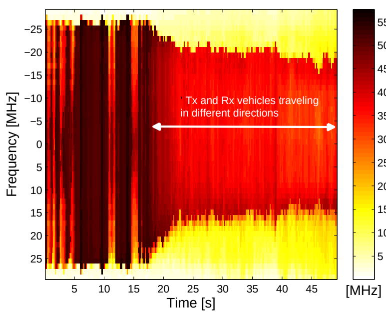

(f) Stationarity frequency bandwidth for different traveling directions (NLoS situation).

Figure 3.10: Time-varying PSDs and the corresponding frequency- and time-dependent stationarity frequency bandwidth, for three different scenarios investigated during the Aalto 2009 measurement campaign. $L = M = 20$, $\Delta_f = \Delta_t = 10$ and $c_f = 0.2$, respectively.

terer with different delays, as shown for example in Figs. 3.10(b) $-$ 3.10(f). Moreover, it has to be pointed out that the stationarity frequency bandwidth decreases abruptly for both low and high frequencies, owing to the limited bandwidth of the measurement system and the PN sequence.

Table 3.1 summarizes *(i):* the 5%-percentile, *(ii):* the median, *(iii):* the 95%-percentile and *(iv):* the standard-deviation of the stationarity frequency bandwidth $F_{\mathrm{s}}(k_f\,;\,k_t)$ estimated in the different scenarios investigated during the Aalto 2009 measurement campaign. Note that the estimated stationarity frequency bandwidths are almost always larger than the frequency bandwidth of the sliding average window used in order to calculate the spatial correlation matrices. The smallest stationarity frequency bandwidths are found to occur in the richest scattering scenarios (e.g. in underground parkings, when the Tx and Rx vehicles pass each other, etc.) with median values around 35 - 40 MHz, whereas their standard-deviations always remain around 15 MHz.

Similar observations were reported in [96], where the validity of the US assumption was assessed by characterizing the amount of change over frequency between consecutive Local Scattering Functions (LSFs), based on the collinearity metric (these LSFs were averaged over all Tx-Rx antenna links, such that the equivalent antenna radiation pattern is almost fully omnidirectional). Mean stationarity frequency bandwidths were in that case reported to range from 80 up to 230 MHz (with a measurement bandwidth of 240 MHz, i.e. edge effects due to the limited measurement bandwidth were also observed), depending on the temporal variability of the scattering environments under investigation (which appear to be mostly similar to the ones described in Section 2.3.3). These values are always much larger than the 10 MHz bandwidth that is used in IEEE 802.11p radio communication systems, such that it can be safely concluded that vehicular radio propagation channels do hardly violate the US assumption.

3.3.2 (In)-validity of the WSS assumption?

For wideband radio propagation channels

Fig. 3.11 shows how much the stationarity time duration $T_{\mathrm{s}}(k_f\,;\,k_t)$ varies simultaneously over frequency and time. The different sub-figures correspond to the same three examplary routes already considered in Section 3.3.1.

As it can be observed, the smallest stationarity time durations $T_{\mathrm{s}}(k_f\,;\,k_t)$ are found to occur when the scattering environment surrounding the Tx and Rx vehicles varies rapidly over time. The spatial structure of the radio propagation channel (and therefore the underlying fading statistics) is then likely to

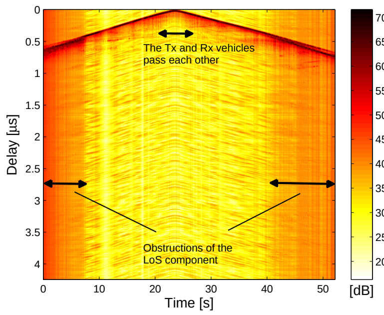

(a) Time-varying PDPs for opposite traveling directions.

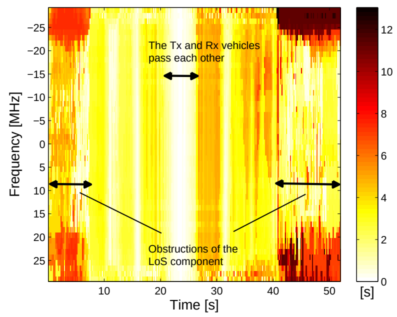

(b) Stationarity time duration for opposite traveling directions.

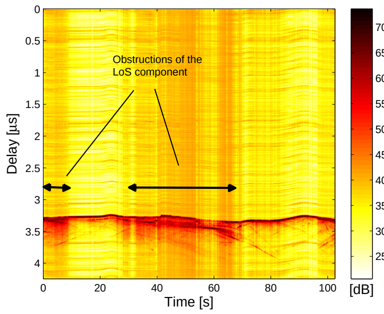

(c) Time-varying PDPs with occasional obstruction of the LoS component.

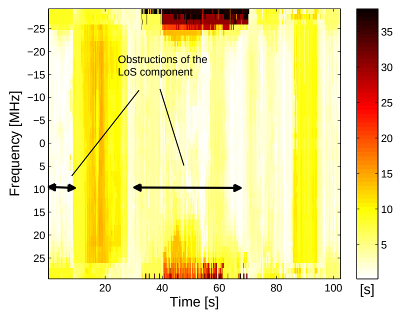

(d) Stationarity time duration with occasional obstruction of the LoS component.

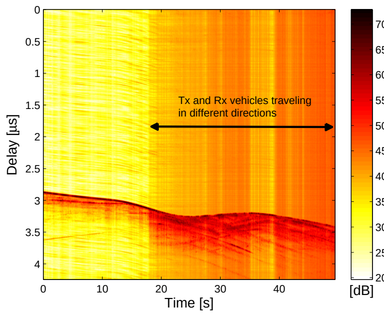

(e) Time-varying PDPs for different traveling directions (NLoS situation).

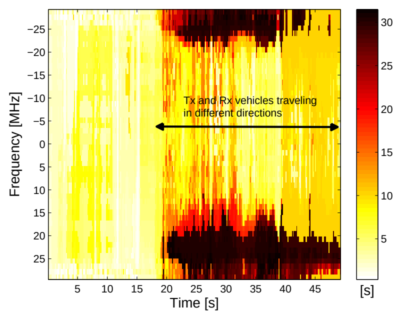

(f) Stationarity time duration for different traveling directions (NLoS situation).

Figure 3.11: Time-varying PDPs and the corresponding frequency- and time-dependent stationarity time duration, for three different scenarios investigated during the Aalto 2009 measurement campaign. $L = M = 20$, $\Delta_f = \Delta_t = 10$ and $c_t = 0.2$, respectively.

change completely over short time scales. This is typically the case when the Tx and Rx vehicles are traveling in opposite directions and pass each other, as shown in Fig. 3.11(b), or when the LoS component becomes suddenly obstructed, as it is illustrated in Fig. 3.11(f). Noteworthy also is the fact that although the LoS component is obstructed, frequencies at the upper and lower edges of the measurement bandwidth exhibit large stationarity time durations. In other words, this means that these frequencies are much less sensitive to changes in the spatial structure of the MIMO radio propagation channel due to the LoS component (contrary to the frequencies at the center of measurement bandwidth). On the other hand, longer stationarity time durations occur when the scattering environment varies more slowly (with respect to the motion of both the Tx and Rx vehicles). This is typically the case when there is a strong LoS component that dominates over the radio wave propagation, as shown in Fig. 3.11(f), or when the LoS component is definitely obstructed (with Tx and Rx vehicles moving slowly), as this is illustrated in Fig. 3.11(e).

Table 3.1 summarizes *(i):* the 5%-percentile, *(ii):* the median, *(iii):* the 95%-percentile and *(iv):* the standard-deviation of the stationarity time duration $T_{\mathrm{s}}(k_f\,;\,k_t)$ estimated in the different scenarios investigated during the Aalto 2009 measurement campaign. Noteworthy are the estimated stationarity time durations always longer than the size of the sliding average window used in order to calculate the spatial correlation matrices. Furthermore, the median stationarity distance ranges from 8.7 up to 31.2 m (or, equivalently, from 4.8 up to 19.2 s, when the Tx and Rx vehicles are traveling at $\bar{v} = 15$ km/h) and its standard-deviation from 10.4 up to 37.5 m (or, equivalently, from 2.5 up to 9.0 s, when $\bar{v} = 15$ km/h), depending on the investigated scenario.

These values are all in good agreement with those reported in [39, 96] (in terms of stationarity distances), where the validity of the WSS assumption was assessed by characterizing the amount of change over time between consecutive LSFs, based on the collinearity metric. Mean stationarity time durations were in that case reported to range from 0.6 up to 2.6 s (i.e. from 15 up to 65 m at $\bar{v} = 90$ km/h), depending on the temporal variability of the scattering environments under investigation.

For narrowband radio propagation channels

As seen in Section 3.3.1, the US assumption can reasonably be considered as holding over the whole measurement bandwidth B, such that multipath components arriving at different delays are uncorrelated. Hence, the size of the sliding average window in the frequency domain can be extended to span the whole measurement bandwidth, i.e. using $L = K = 510$ frequency bins. The

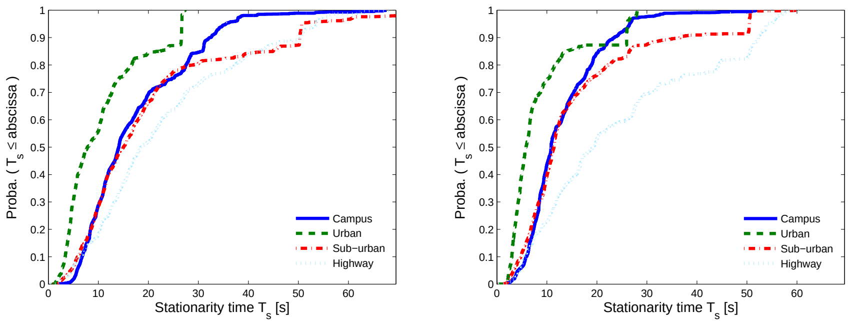

(a) At the Tx side. (b) At the Rx side.

Figure 3.12: CDFs of the stationarity time duration estimated $T_{\mathrm{s}}(k_t)$ for all the environments investigated during the Aalto 2007 measurement campaign. $M = 20$, $\Delta_t = 1$ and $c_t = 0.2$, respectively.

so-estimated spatial correlation matrices thus characterize the spatial structure of the equivalent narrowband radio propagation channel, which is obtained from the IRs by coherent summation in the delay domain, i.e.

$$\mathbf{H}(nt_{\mathrm{rep}}) = \sum_{k=0}^{K-1} \mathbf{H}(\tau_k\,;\,nt_{\mathrm{rep}}). \tag{3.7}$$

Enlarging the size of the sliding average window thus allows a refined estimation of the spatial correlation matrices. The variations in the spatial structure of the MIMO radio propagation channel are then more accurately detected and characterized, hence yielding a better resolution for the identification of time-varying stationarity time duration $T_{\mathrm{s}}(k_t)$.

Table 3.1 summarizes *(i):* the 5%-percentile, *(ii):* the median, *(iii):* the 95%-percentile and *(iv):* the standard-deviation of the stationarity time duration $T_{\mathrm{s}}(k_t)$ estimated in the different scenarios investigated during the Aalto 2009 measurement campaign. On the other hand, Table 3.3 provides the parameterization of the corresponding Gamma distribution. Both the wideband and narrowband stationarity time durations $T_{\mathrm{s}}(k_f\,;\,k_t)$ and $T_{\mathrm{s}}(k_t)$ are found to be relatively close one from another. Though, some discrepancies can be observed, due to a limited data sets for some scenarios, e.g. in the case when the Tx and Rx vehicles are traveling in different directions.

Moreover, Fig. 3.12 shows the Cumulative Density Functions (CDFs) of the stationarity time duration $T_{\mathrm{s}}(k_t)$ estimated in all the environments investigated during the Aalto 2007 measurement campaign. When the Tx and Rx vehicles are traveling in the same direction, median stationarity distances range between 10 and 40 m (or, equivalently, median stationarity time durations between 4.8 and 19.2 s, when $\bar{v} = 7.5$ km/h), in good agreement with the results of the Aalto 2009 measurement campaign. The smallest stationarity time durations occur in the urban environment, owing to a high density of scatterers which can appear or disappear on very short time scales. On the other hand, the highway environment provides the largest stationarity time durations, due to a fewer number of scatterers homogeneously distributed in the environment surrounding the Tx and Rx vehicles. Moreover, since the campus and suburban environments share the same characteristics, they provide comparable stationarity time durations.

Noteworthy also are the stationarity time durations at the Tx and Rx sides very similar, i.e. the corresponding spatial structures of the MIMO radio propagation channel indicate the same changes in the scattering environment over time. In other words, it can be concluded that the WSS assumption holds for vehicular radio propagation channels only locally over short time intervals.

3.4 Statistical modeling the non-stationary behavior

The distribution of the stationarity frequency bandwidths and stationarity time durations can now be characterized to account for their time and frequency variability, respectively. In this Section, we will consider only the ones estimated from the data collected during the Aalto 2009 measurement campaign.

3.4.1 Modeling the stationarity frequency bandwidths

Fig. 3.13 shows that the frequency- and time-dependent stationarity frequency bandwidth $F_{\mathrm{s}}(k_f\ ;\ k_t)$ can be best described using a three-modal Gaussian distribution, which is defined as

$$f(\omega_i\,;\,\mu_i\,;\,\sigma_i) = \sum_{i=1}^{3} \omega_i\,\mathcal{N}\,(\mu_i\,;\,\sigma_i), \tag{3.8}$$

where $\mathcal{N}\,(\mu_i\,;\,\sigma_i)$ denotes the normal PDF of the i^{th} mode of the distribution with mean μ_i and standard-deviation σ_i, and ω_i the associated weight, respectively. The parameterization of this three-modal Gaussian distribution is provided in Table 3.2 for all the scenarios that were investigated during the Aalto 2009 measurement campaign.

The first mode describes approximately 10% of the overall distribution and encompasses the smallest stationarity frequency bandwidths. These values are usually found within two sub-bands of approximately 3 MHz located at both

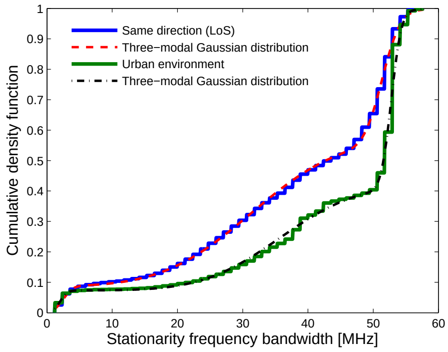

Figure 3.13: Distribution of the frequency- and time-dependent stationarity frequency bandwidth $F_{\mathrm{s}}(k_f\,;\,k_t)$ estimated at the Rx side, for two different scenarios taken from the Aalto 2009 measurement campaign. $L = M = 20$, $\Delta_f = \Delta_t = 10$ and $c_f = 0.2$, respectively.

the lower and upper edges of the measurement bandwidth, as it can be observed in Fig. 3.10. These two sub-bands correspond to the frequencies for which the transmitted power drops significantly, owing to the limited bandwidth of the measurement system and the PN sequence. These stationarity frequency bandwidths can therefore be considered as artifacts, which do not reliably characterize the non-stationary behavior of the underlying MIMO radio propagation channel at these frequencies, and could easily be discarded from the modeling (i.e. by investigating the validity of the US assumption over only the central part of the measurement bandwidth, which is $60-2\times 3 = 54$ MHz wide). However, this mode can possibly represent up to 30% of the measured stationarity frequency bandwidths in very rich scattering environments (typically when the Tx and Rx vehicles are traveling in separate directions, under deep NLoS conditions). On the other hand, the second mode characterizes intermediate values of the stationarity frequency bandwidth which are typically ranging from 30 to 40 MHz (i.e. larger than the 10 MHz bandwidth of the IEEE 802.11p standard). This mode corresponds therefore to situations where multipath components are arriving at the Rx side with significant power (this typically occurs in rich scattering environment). Finally, the last mode of the distribution encompasses the largest stationarity frequency bandwidths, which are covering almost the whole measurement bandwith. This corresponds to situations when multipath components that are arriving at the Rx side have only a minor impact in the radio wave propagation (typically when there are only few scatterers in the environment surrounding the Tx and Rx vehicles) and

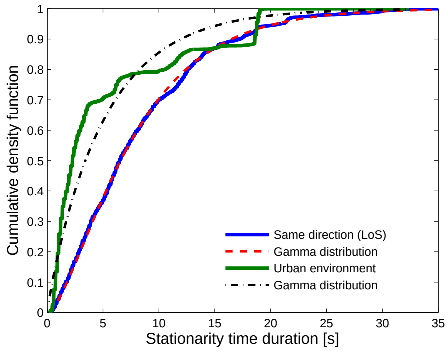

Figure 3.14: Distribution of the frequency- and time-dependent stationarity time duration $T_\mathrm{s}(k_f\,;\,k_t)$ estimated at the Rx side, for two different scenarios taken from the Aalto 2009 measurement campaign. $L = M = 20$, $\Delta_f = \Delta_t = 10$ and $c_f = 0.2$, respectively.

represent in all the investigated scenarios about 30 to 60% of the measured values.

3.4.2 Modeling the stationarity time durations

Fig. 3.14 shows that the frequency- and time-dependent stationarity time duration $T_\mathrm{s}(k_f\,;\,k_t)$ can be modeled using a Gamma distribution, with PDF

$$f(x\,;\,\theta,k) = \frac{1}{\theta^k}\frac{1}{\Gamma(k)}x^{k-1}e^{-\frac{x}{\theta}}, \tag{3.9}$$

where θ and k are the scale and shape parameters of the distribution, respectively. The parameterization of the Gamma distribution of the stationarity time duration $T_\mathrm{s}(k_f\,;\,k_t)$ estimated in the different scenarios investigated during the Aalto 2009 measurement campaign is provided in Table 3.3.

3.5 Conclusions and general comments

In this Chapter, the non-stationary behavior of MIMO vehicular radio propagation channels was investigated by measuring the amount of change in their spatial structure over both frequency and time. The CMD was used for that purpose, as it was shown to successfully detect significant changes in the scattering environment surrounding the Tx and Rx vehicles, e.g. the (dis)-appearance of the LoS component, when the Tx and Rx vehicles pass one another, when they are moving away one from another, etc. Both the WSS and US assumptions were then assessed by applying indicative thresholds on the CMD.

Time- and frequency-dependent stationarity time durations and frequency bandwidths were defined as the local regions in time and frequency over which the underlying fading statistics remain constant, respectively. The measured stationarity distances and frequency bandwidths were approximately 10 to 40 m long (depending on the environment or scenario under investigation) and 40 to 50 MHz wide (i.e. almost the whole measurement bandwidth), respectively. Interestingly, note that these values are all in good agreement with those estimated from different measurement campaigns using another metric [39, 96].

From these observations, it can therefore be concluded that the WSS assumption holds only over very short time intervals, whereas the US assumption is not violated within the 10 MHz bandwidth of IEEE 802.11p radio communication systems. In other words, the non-stationary behavior of vehicular radio propagation channels is much more critical over time than over frequency.

Moreover, it has to be pointed out that there is no clear relationship between the estimated stationarity time durations and frequency bandwidths. For example, strong violations of the WSS assumption (i.e. short stationarity distances) do not necessarily imply the fact that the US assumption will also be strongly violated, since they do not rely on the same radio wave propagation mechanisms, i.e.

- The non-stationary behavior over frequency depends on the richness of the scattering environment surrounding the Tx and Rx vehicles. Rich (resp. poor) scattering environments yield indeed smaller (resp. larger) stationarity frequency bandwidths F_{s},
- The non-stationary behavior over time depends on how rapidly the scattering environment changes around the Tx and Rx vehicles. Highly dynamic (resp. static) scattering environments (with respect to the motion of the Tx and Rx vehicles) yield indeed smaller (resp. larger) stationarity time durations T_{s}.

Hence, let us consider for example a rich scattering environment that remains "static" over time (with respect to the motion of the Tx and Rx vehicles). In that case, the WSS assumption can be fulfilled over wide stationarity time durations, whereas the US assumption holds over small stationarity frequency bandwidths. If now all the scatterers in this environment start moving, then the scattering environment surrounding the Tx and Rx vehicles will be not only rich but also rapidly time-varying. In other words, the US assumption will still hold only over small stationarity frequency bandwidths, while the WSS assmuption will now be fulfilled over shorter stationarity time durations.

Table 3.1: Stationarity intervals for all the the scenarios investigated during the Aalto 2009 measurement campaign. For the frequency- and time-dependent stationarity frequency bandwidth and time duration: $L = M = 20$, $\Delta_f = \Delta_t = 10$ and $c_f = c_t = 0.2$, respectively. For the time-dependent stationarity time duration: $L = 20$, $\Delta_t = 10$ and $c_t = 0.2$, respectively.

		$F_\mathrm{s}(k_f\,;\,k_t)$ [MHz]	$T_\mathrm{s}(k_f\,;\,k_t)$ [s]	$T_\mathrm{s}(k_t)$ [s]
Underground parkings (3 routes)	5 % prctile	2.35	0.45	0.60
	Median	41.18	3.60	4.95
	95 % prctile	54.12	13.19	16.34
	Std.	15.30	4.26	5.41
Road crossings (2 routes)	5 % prctile	2.35	0.30	0.45
	Median	41.18	2.40	3.15
	95 % prctile	55.29	10.94	11.39
	Std.	16.15	3.36	3.57
Urban environment (2 routes)	5 % prctile	2.35	0.60	0.75
	Median	51.76	2.25	2.55
	95 % prctile	55.29	18.74	18.89
	Std.	15.14	5.99	6.39
Opposite directions (3 routes)	5 % prctile	3.53	0.45	0.60
	Median	43.53	3.00	3.60
	95 % prctile	54.12	8.40	9.00
	Std.	16.84	2.54	2.47
Different directions (1 route)	5 % prctile	4.71	1.50	2.53
	Median	36.47	7.50	8.10
	95 % prctile	52.94	30.13	16.49
	Std.	16.06	8.86	4.55
Static-to-mobile (4 routes)	5 % prctile	3.53	0.45	0.75
	Median	43.53	2.10	2.70
	95 % prctile	52.94	13.04	8.40
	Std.	17.44	4.60	2.49
Same direction (LoS) (8 routes)	5 % prctile	2.35	1.20	1.65
	Median	43.53	7.50	8.85
	95 % prctile	54.12	21.44	27.60
	Std.	16.28	6.40	7.43
Same direction (partial NLoS) (7 routes)	5 % prctile	3.53	0.60	1.05
	Median	41.18	4.35	5.25
	95 % prctile	52.94	16.04	16.34
	Std.	17.09	5.18	4.84

Table 3.2: Parameters of the three-modal Gaussian distribution of the stationarity frequency bandwidth $F_\mathrm{s}(k_f\,;\,k_t)$ for all the scenarios investigated during the Aalto 2009 measurement campaign. $L = M = 20$, $\Delta_f = \Delta_t = 10$ and $c_f = 0.2$, respectively.

	$i=1$			$i=2$			$i=3$		
	ω_1	μ_1	σ_1	ω_2	μ_2	σ_2	ω_3	μ_3	σ_3
Underground parkings (3 routes)	0.07	1.97	0.81	0.57	33.51	10.14	0.36	52.30	1.70
Road crossings (2 routes)	0.10	3.23	1.74	0.51	32.79	10.72	0.39	51.20	2.97
Urban environment (2 routes)	0.07	2.01	0.90	0.35	35.71	9.30	0.58	52.76	1.24
Opposite directions (3 routes)	0.12	4.54	2.87	0.51	35.17	11.36	0.37	52.50	1.33
Different directions (1 route)	0.28	10.28	5.75	0.48	36.88	4.43	0.24	51.85	1.68
Static-to-mobile (4 routes)	0.21	8.41	5.40	0.40	36.03	9.83	0.39	52.01	1.41
Same direction (LoS) (8 routes)	0.09	2.51	1.19	0.48	31.33	10.68	0.43	51.40	2.18
Same direction (partial NLoS) (7 routes)	0.14	4.59	2.37	0.50	31.89	11.91	0.36	50.62	2.34

Table 3.3: Parameters of the Gamma distribution of the stationarity time durations $T_{\mathrm{s}}(k_f\,;\,k_t)$ and $T_{\mathrm{s}}(k_t)$ for all the scenarios investigated during the Aalto 2009 measurement campaign. For $T_{\mathrm{s}}(k_f\,;\,k_t)$: $L = M = 20$, $\Delta_f = \Delta_t = 10$ and $c_f = c_t = 0.2$, respectively. For $T_{\mathrm{s}}(k_t)$: $L = 510$, $M = 20$, $\Delta_t = 10$ and $c_t = 0.2$, respectively.

	$T_{\mathrm{s}}(k_f\,;\,k_t)$ [s]		$T_{\mathrm{s}}(k_t)$ [s]	
	k_{s}	θ_{s} [s]	k_{s}	θ_{s} [s]
Underground parkings (3 routes)	1.26	3.93	1.33	4.96
Road crossings (2 routes)	1.29	2.87	1.47	2.91
Urban environment (2 routes)	0.93	5.51	1.00	5.86
Opposite directions (3 routes)	1.71	2.08	2.11	1.93
Different directions (1 route)	1.51	6.74	3.39	2.49
Static-to-mobile (4 routes)	1.09	3.23	2.09	1.65
Same direction (LoS) (8 routes)	1.67	4.87	1.75	5.42
Same direction (partial NLoS) (7 routes)	1.27	4.43	1.71	3.62

Table 3.4: Parameters of the Gamma distribution of the stationarity time duration $T_{\text{s}}(k_t)$ at the Tx and Rx sides in all the environments investigated during the Aalto 2007 measurement campaign. $L = 510$, $M = 1$, $\Delta_t = 10$ and $c_t = 0.2$, respectively.

	At the Tx side		At the Rx side	
	k_{s}	θ_{s} [s]	k_{s}	θ_{s} [s]
Campus (4 routes)	3.06	5.67	3.54	3.70
Urban (3 routes)	2.04	5.24	1.95	4.47
Sub-urban (6 routes)	1.86	11.06	1.92	8.25
Highway (5 routes)	2.19	10.57	1.89	12.91

CHAPTER 4

Stochastic modeling of non-stationary vehicular channels

As pointed out in the Chapter 3, vehicular radio propagation channels are intrinsically non-stationary. The WSS assumption is indeed fulfilled only over short traveled distances (typically on the order of 10 to 40 m), such that each OFDM frame of the transmitted signal may experience different fading conditions. On the other hand, the US assumption remains valid over large frequency bandwidths (typically on the order of 40 to 50 MHz), so that it is almost never not violated over the narrower (10 MHz) bandwidth of IEEE 802.11p communication systems. Finally, the H assumption can also be violated, owing to correlation between adjacent antenna elements or non-isotropic antenna patterns at the Tx and Rx sides. As a consequence, the statistical properties of vehicular radio propagation channels can no longer be considered as constant over any of these dimensions, as it is the case in the already existing stochastic radio propagation channel models (TDLs are for example based on the WSS-US assumption).

Therefore, this Chapter focuses on the characterization of these time, frequency and space non-stationary behaviors. Section 4.1 first covers the time- and space-varying description of the narrowband large- and small-scale fading statistics. These statistics are estimated over the time-varying narrowband stationarity time intervals that were previously identified in Section 3.3.2 and compared to the values that would have been obtained under the WSS assumption. This approach is then extended in Section 4.2 to the wideband case, over the whole 60 MHz measurement bandwidth. The time and space dependencies of the Ricean K-factor as well as of the RMS delay spread are investigated over the time-varying wideband stationarity time intervals that were previously identified in Section 3.3.2.

4.1 Narrowband channel modeling

As the non-stationary behavior of vehicular radio propagation channels is much stronger over time than over frequency (especially for IEEE 802.11p radio communication systems), we focus in the following only on the non-stationary statistical characterization of the equivalent narrowband radio propagation channels, as given by Eq. (1.2), based on the data collected during the Aalto 2007 measurement campaign (described in Section 2.2). This is indeed relevant, since the US assumption was found in the Section 3.3.1 to hold over the whole measurement bandwidth.

4.1.1 Fading statistics under WSS assumption

Let first suppose the case where the WSS assumption is always fulfilled. The large- and small-scale fading statistics are then assumed to remain constant over the whole measurement time and can therefore be estimated using different approaches, namely

Separation of the large- and small-scale fading processes

The average received power can be estimated at each time instant and for each Tx-Rx antenna pair by low-pass filtering the received power with a 40λ sliding average window [97], such that

$$S(k_t\,;\,p) = \frac{1}{N_{\text{LS}}} \sum_{n'=k_t-N_{\text{LS}}/2}^{k_t+N_{\text{LS}}/2-1} |h(k_t\,;\,p)|^2\,. \tag{4.1}$$

According to Eq. (1.2), the large-scale fading is then extracted by removing from the so-estimated average received power the deterministic distance dependent pathloss, so that it can be expressed (in the dB scale) as

$$S_{\text{LS,[dB]}}(k_t\,;\,p) = S_{\text{[dB]}}(k_t\,;\,p) - G_{0,\text{[dB]}} - 10n\log_{10}\left(\frac{d}{d_0}\right). \tag{4.2}$$

For each Tx-Rx antenna pair, the so-extracted large-scale fading can be modeled as a normally distributed random process with zero-mean and variance $\sigma^2_{\text{LS,[dB]}}(p)$. On the other hand, the small-scale fading can be derived as

$$s_{\text{ss}}(k_t\,;\,p) = \frac{h(k_t\,;\,p)}{\sqrt{S(k_t\,;\,p)}}. \tag{4.3}$$

For each Tx-Rx antenna link, the envelope of the so-extracted small-scale fading can be modeled as a Ricean random process, with K-factor $K_{\text{ss}}(p)$. K-factor values close to 0 (in linear scale) denote deep (Rayleigh-like) fading conditions, while larger values yield more coherent fading conditions, i.e. with less variations in amplitude.

Composite modeling

Such approaches were originally proposed for satellite and land mobile communications systems, when the small- and large-scale fading mechanisms tend to occur on similar distance scales and are therefore intrinsically mixed. In that case, the received signal envelope can be modeled as the product of two different processes (after having removed the pathloss component) , i.e.

$$h(k_t\,;\,p) = \sqrt{S_{\text{LS}}(k_t\,;\,p)}\,\cdot\,s_{\text{ss}}(k_t\,;\,p), \tag{4.4}$$

where $S_{\text{LS}}(k_t\,;\,p)$ and $s_{\text{ss}}(k_t\,;\,p)$ are the large- and small-scale fading, respectively. The PDF of the received signal envelope is then given by

$$f_{|h|}(x) = \int_0^{+\infty} f_{\text{ss}}(x|y) f_{\text{LS}}\,(y)\,dy, \tag{4.5}$$

where $f_{\text{ss}}(x|y)$ is the PDF of the envelope of the small-scale fading conditioned on a certain large-scale fading, whose PDF is given by $f_{\text{LS}}(y)$. Assuming these two processes to be independent one from another, their joint distribution can then be rewritten as

$$f_{|h|}(x) = \int_0^{+\infty} \frac{1}{y} f_{\text{ss}}\left(\frac{x}{y}\right) f_{\text{LS}}(y)dy. \tag{4.6}$$

Any mixture of distributions can be considered in these relationships for the characterization of the narrowband received signal envelope. As a result, when combining Eqs. (1.3) and (1.5), the PDF of the composite Rice-lognormal distribution can be expressed as

$$\begin{aligned} f_{|h|}(x) = \int_0^{+\infty} \frac{1}{\sigma_{\text{ss}}^2}\frac{x}{y} e^{-\left[K_{\text{ss}}+\frac{1}{2\sigma_{\text{ss}}^2}\left(\frac{x}{y}\right)^2\right]}\,\cdot \\ I_0\left(\frac{\sqrt{2K_{\text{ss}}}}{\sigma_{\text{ss}}}\frac{x}{y}\right)\frac{1}{\sqrt{2\pi}\sigma_{\text{LS}}y} e^{-\frac{(\ln y)^2}{2\sigma_{\text{LS}}^2}}\,dy, \end{aligned} \tag{4.7}$$

where K_{ss} and σ_{ss} are the Ricean K-factor and the energy of the diffuse part of the small-scale fading, respectively, whereas σ_{LS}^2 denotes the variance of the zero-mean lognormal large-scale fading. Fig. 4.1 shows the CDF of the Rice-lognormal composite distribution under different fading conditions.

Note that when $K_{\text{ss}} \to 0$, the Rice-lognormal composite distribution in Eq. (4.7) reduces to the more severe Rayleigh-lognormal one. Moreover, in the limit for $K_{\text{ss}} \to \infty$ (resp. $\sigma_{\text{LS}}^2 \to 0$), the small- (resp. large-) scale fading effects diminish, such that the envelope of the received signal is purely lognormally (resp. Ricean) distributed.

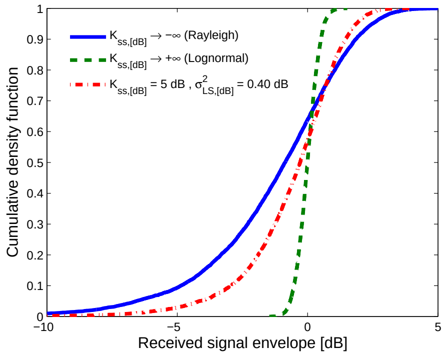

Figure 4.1: CDF of the composite Rice-lognormal distribution under various fading conditions.

Based on the moments of the Ricean and lognormal distributions, the t^{th} order moment of this composite model can be derived as

$$\mathrm{E}\left\{|h(k_t\,;\,p)|^t\right\} = \mathrm{E}\left\{|S_{\text{LS}}(k_t\,;\,p)|^t\right\}\,\mathrm{E}\left\{|s_{\text{ss}}(k_t\,;\,p)|^t\right\}. \tag{4.8}$$

Assuming that the small-scale fading has unit average power, the second-order moment of the composite model can be rewritten as the product of the second-order moments of the (lognormal) large- and (Ricean) small-scale fading (given that they are independent one from another), i.e.

$$\mathrm{E}\left\{|h(k_t\,;\,p)|^2\right\} = \mathrm{E}\left\{|S_{\text{LS}}(k_t\,;\,p)|^2\right\} = e^{2\sigma^2_{\text{LS}}}. \tag{4.9}$$

Hence, the variance σ^2_{LS} of the large-scale fading can then be estimated from the second order moment of the received signal envelope such that

$$\sigma^2_{\text{LS}} = \frac{1}{2}\log \mathrm{E}\left\{|h(k_t\,;\,p)|^2\right\}. \tag{4.10}$$

On the other hand, the first-order moment of the composite model can be similarly rewritten as the product of the first-order moments of the (lognormal) large- and (Ricean) small-scale fading (given that they are independent one from another), i.e.

$$\begin{aligned}\mathrm{E}\left\{|h(k_t\,;\,p)|\right\} &= \mathrm{E}\left\{|S_{\text{LS}}(k_t\,;\,p)|\right\}\,\mathrm{E}\left\{|s_{\text{ss}}(k_t\,;\,p)|\right\}\\ &= e^{\frac{1}{2}\sigma^2_{\text{LS}}}\,\frac{1}{2}\sqrt{\frac{\pi}{K_{\text{ss}}+1}}\mathrm{L}_{1/2}\left(-K_{\text{ss}}\right),\end{aligned} \tag{4.11}$$

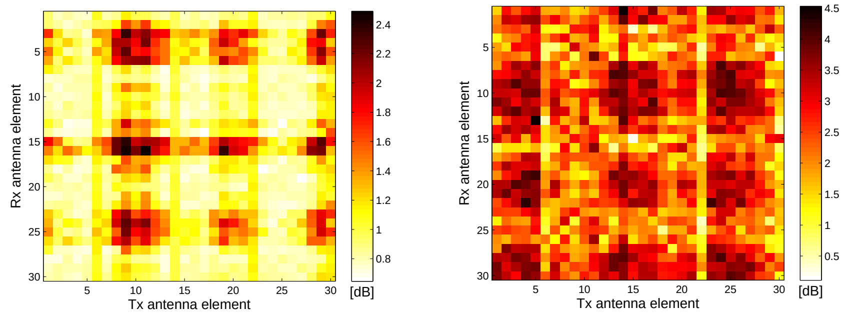

(a) Variance of the large-scale fading. (b) Ricean K-factor of the small-scale fading.

Figure 4.2: Fading statistics extracted after separation of the large- and small-scale fading, for one route in the highway environment taken from the Aalto 2007 measurement campaign.

where $\mathrm{L}_{1/2}(x)$ denotes a Laguerre polynomial. As a consequence, the Ricean K-factor can be coarsely estimated by grid searching as the value that minimizes the following objective function

$$\left| \mathrm{E}\left\{ |h(k_t\,;\,p)| \right\} - e^{\frac{1}{2}\sigma^2_{\mathrm{LS}}} \frac{1}{2} \sqrt{\frac{\pi}{K_{\mathrm{ss}}+1}} \mathrm{L}_{1/2}\left(-K_{\mathrm{ss}}\right) \right|, \tag{4.12}$$

The so-found parameter estimates are then used as starting points for a numerical curve fitting between the CDFs of the received signal envelope and the composite distribution.

Empirical results

Fig. 4.2 shows that the large- and small-scale fading statistics, estimated under the WSS assumption, can vary significantly from one Tx-Rx antenna pair to another, depending on their relative orientation.

Tx and Rx antenna pairs facing one another, i.e. between elements located at the backside (resp. frontside) of the Tx (resp. Rx) antenna array (see Table 2.2 for the link to element mapping and Fig. 2.2(b) for the position of the elements in the antenna array, respectively) are indeed the ones that are the most likely to experience strong coherent contributions dominating over the radio wave propagation (typically the LoS component). They are therefore associated with the smallest variances σ^2_{LS} and the largest Ricean K-factors K_{ss} for the large- and small-scale fading, respectively.

More surprisingly, the same behavior can also be observed for Tx-Rx antenna pairs that are completely hidden one from another, i.e. between elements

Table 4.1: Large- and small-scale fading statistics estimated using the separation and composite modeling approaches, respectively, for all the scenarios investigated during the Aalto 2007 measurement campaign.

		Separate modeling		Composite modeling	
		σ^2_{LS} [dB]	K_{ss} [dB]	σ^2_{LS} [dB]	K_{ss} [dB]
	5 % prctile	1.53	0.23	1.52	-0.15
Campus	Median	2.06	1.93	2.11	1.74
(4 routes)	95 % prctile	3.64	3.57	4.00	4.28
	Std.	0.70	1.07	0.80	1.28
	5 % prctile	1.49	-0.87	1.45	-0.71
Urban	Median	2.52	1.25	2.41	1.30
(3 routes)	95 % prctile	3.80	3.71	3.86	3.56
	Std.	0.79	1.44	0.79	1.43
	5 % prctile	1.80	-0.83	1.93	-0.83
Sub-urban	Median	2.51	0.99	2.41	0.75
(6 routes)	95 % prctile	4.53	4.78	4.82	4.88
	Std.	0.84	1.63	0.92	1.77
	5 % prctile	1.56	-0.52	1.45	-0.71
Highway	Median	2.38	1.68	2.41	1.44
(4 routes)	95 % prctile	3.99	4.10	4.34	4.60
	Std.	0.76	1.51	0.90	1.65

located at the frontside (resp. backside) of the Tx (resp. Rx) antenna array (owing to their semi-spherical geometries). Indeed, these Tx and Rx antenna pairs can experience some coherent contributions as well (even though the LoS component is in that case obstructed), which are typically stemming from other vehicles traveling either in front of or behind the Tx vehicle and Rx ones. As a consequence, slightly larger variances σ^2_{LS} and smaller Ricean K-factors K_{ss} can possibly be obtained for the large- and small-scale fading, respectively.

Finally, Tx and Rx antenna pairs looking towards the roadsides are the ones for which the scattering environment is changing the most rapidly (owing to all the scatterers that can be located on the roadsides), such that they hardly have the possibility of experiencing strong coherent contributions in the radio wave propagation. In that case, large fluctuations can be observed in the envelope of their narrowband radio propagation channels, hence yielding the largest variances σ^2_{LS} and the smallest Ricean K-factors K_{ss} for the large- and small-scale fading, respectively.

Based on these observations, we can already state that the fading behavior is strongly dependent on the geometry of the antenna arrays that are used at the

Tx and Rx sides, depending on how they are radiating (i.e. on their possibility, or not, of experiencing strong coherent contributions dominating over the radio wave propagation). Moreover, Table 4.1 shows that similar values (and thus similar trends) can be obtained for the variance σ^2_{LS} and the Ricean K-factor K_{ss} when using the composite and separate modeling approaches, so that these two approaches can be considered as providing consistent results.

4.1.2 Non-WSS fading statistics

Let us now consider the (more realistic) case where the statistics of the large- and small-scale fading fluctuate over time. As seen in Section 3.3.2, the WSS assumption remains in that case valid only over short time intervals, over which these statistics can be reliably estimated.

Extraction of the fading statistics

The large-scale fading is estimated by low-pass filtering over each stationarity time interval the received power with a 40 wavelength sliding window, i.e.

$$S_{\text{LS}}(k_t, m\,;\,p) = \frac{1}{M}\sum_{m'=m-M/2}^{m+M/2-1} |h(k_t\,;\,p)|^2\,, \tag{4.13}$$

where $m = k_{t,\text{min}}(k_t){+}M/2, ..., k_{t,\text{max}}(k_t){-}M/2{+}1$ is the relative time index within the k_t^{th} stationarity time interval, as previously defined in Eq. (3.5). In the following, the large-scale fading over the k_t^{th} stationarity time interval is denoted as a data set such that

$$\begin{aligned} S_{\text{LS}}(k_t\,;\,p) = \{&S_{\text{LS}}(k_t, m\,;\,p)\,,\\ &m = k_{t,\text{min}}(k_t) + M/2, ..., k_{t,\text{max}}(k_t) - M/2 + 1\}\,. \end{aligned} \tag{4.14}$$

For each Tx-Rx antenna pair, the large-scale fading can be modeled over each stationarity time interval as a lognormally distributed random process, which is therefore characterized by a time-and space-dependent variance $\sigma^2_{\text{LS}}(k_t\,;\,p)$. The small-scale fading is then obtained by removing over each stationarity time interval the large-scale fading from the measured narrowband radio propagation channel, such that

$$s_{\text{ss}}(k_t\,;\,m\,;\,p) = \frac{h(m\,;\,p)}{\sqrt{S_{\text{LS}}(k_t\,;\,m\,;\,p)}}. \tag{4.15}$$

For each Tx-Rx antenna pair, the envelope of the small-scale fading can be modeled over each stationarity time interval as a Ricean random process, hence characterized by a time-and space-dependent Ricean K-factor $K_{\text{ss}}(k_t\,;\,p)$.

Fading analysis over stationary time intervals

As already mentioned in Section 4.1.1, all the Tx-Rx antenna pairs experience different conditions regarding the radio wave propagation (depending on where they are located in their respective arrays). For a same given time instant, all the Tx-Rx antenna pairs are thus undergoing different conditions for the large- and small-scale fading, such that each can be associated with a different variance σ^2_{LS} and a different Ricean K-factor K_{ss}, respectively.

Fig. 4.3 shows also that all the Tx-Rx antenna pairs exhibit the same tendency for the time-varying behavior of their large- and small-scale fading statistics. Strong fluctuations can indeed be observed in the narrowband received signal envelope level from approximately times $t = 10$ to $t = 35$ s, so that each Tx-Rx antenna pair is significantly impacted by the large-scale fading. As a result, both large variances σ^2_{LS} and small Ricean K-factors K_{ss} are to be reported within this time interval. On the other hand, when the received signal envelope becomes more coherent (i.e. when it experiences less fluctuations), as it can be observed between times $t = 0$ and $t = 10$ s, each Tx-Rx antenna pair is then associated with smaller variances σ^2_{LS} and larger Ricean K-factors K_{ss}, respectively.

Regions over which the large- and small-scale fading statistics remain approximately constant (for all the Tx-Rx antenna pairs) can therefore clearly identified and are approximately delimited (based on a visual inspection) in Fig. 4.3 by black dashed-lines. This is typically the case between times $t = 45$ and $t = 95$ s, when the LoS component is obstructed and the narrowband total received power level drops by roughly 10 dB. These regions match very well to the stationarity time intervals, over which the large- and small-scale fading statistics were estimated. In other words, this corroborates the fact that the stationarity time intervals identified in Section 3.3.2 are strongly dependent on the variations of the underlying narrowband radio propagation channel statistics.

Moreover, transitions between two consecutive stationarity regions are often characterized by harsh variations in the time-varying behavior of both the large- and small-scale fading statistics. This can for example be noticeably observed at time $t = 10$ s, when the Ricean K-factor suddenly drops by approximately 8 dB (conversely, the variance of the large-scale fading then suddenly increases by roughly 2 dB). In that case, the small-scale fading switches indeed abruptly from strong Ricean conditions to Rayleigh (or even “worse than Rayleigh”) ones owing to changes in the surrounding scattering environment (as it can be also observed from the corresponding envelope of the narrowband radio propagation channel).

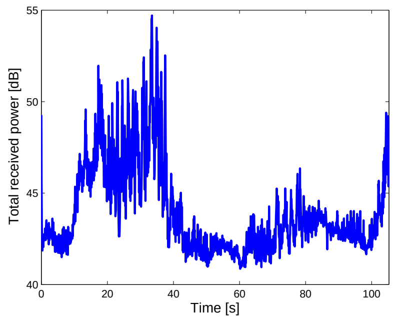

(a) Received power averaged over all Tx-Rx antenna pairs.

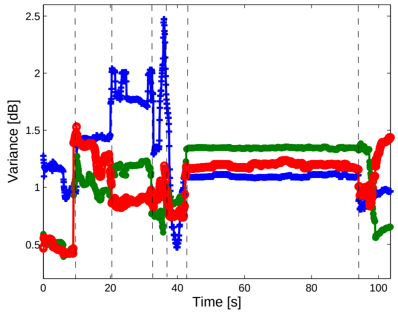

(b) Variance of the large-scale fading.

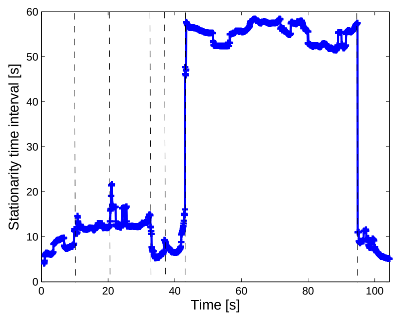

(c) Stationarity time intervals.

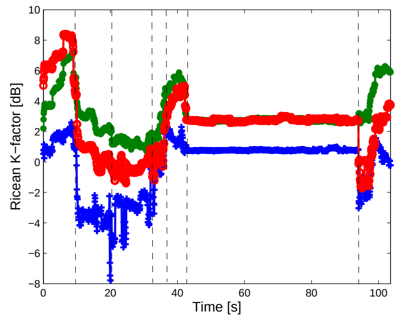

(d) Ricean K-factor.

Figure 4.3: Time-varying evolution of the large- and small-scale statistics for various examplary Tx-Rx antenna pairs, for one route in the highway environment taken from the Aalto 2007 measurement campaign.

Comparison between WSS and non-WSS modeling

Fig. 4.4 shows that the fading statistics estimated under the WSS assumption represent very well the average behavior of the fading over time, whatever the Tx-Rx antenna pair that is considered.

Hence, using radio propagation channel models based on the WSS assumption with parameters constant over time, as it is the case in the IEEE 802.11p standard [3], implies that only the average behavior of (real-world) non-stationary radio propagation channels can be investigated. In other words, only the average performances of a radio communication system can in that case be investigated. However, they can definitely not be used in order to accurately predict its instantaneous performances when the fading statistics of the radio propagation channel vary (sometimes severely) over time.

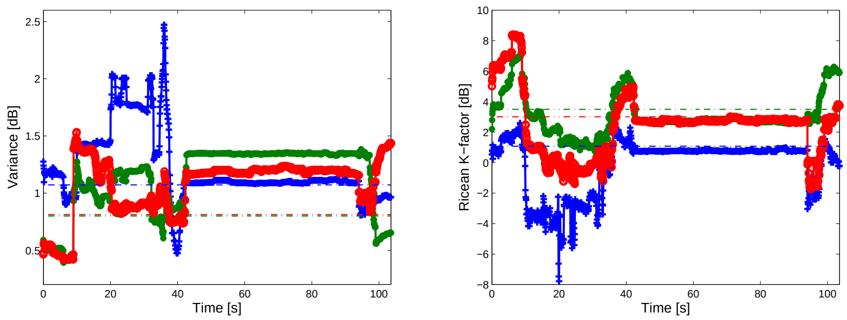

(a) Variance of the large-scale fading. (b) Ricean K-factor.

Figure 4.4: Comparison between the WSS and the time-varying estimates of the large- and small-scale fading, respectively.

Impact of the size of the stationarity time intervals

Fig. 4.5 depicts the effects of the size of the stationarity time intervals on the estimation of the fading statistics. The goodness-of-fit is determined for each Tx-Rx antenna pair and over each stationarity interval by means of the Mean Square Error (MSE) estimator, which is defined as

$$\mathrm{MSE}(k_t\,;\,p) = \mathrm{E}\left\{\left|F\left(x\right) - F'\left(x\right)\right|^2\right\}, \tag{4.16}$$

where $F(x)$ is the empirical CDF of the large- (resp. small-) scale fading over the k_t^{th} stationarity time interval, while $F'(x)$ denotes the corresponding fitted lognormal (resp. Ricean) CDF, respectively.

When short stationarity time durations are considered, the number of samples appears to be no longer sufficient so as to obtain reliable estimates of the fading statistics. As a consequence, the corresponding MSE values increase accordingly. Conversely, larger stationarity time durations are found to be associated with smaller MSE values (i.e. to more accurate fading statistics), as the number of samples progressively increases. Such an adaptive observation window assures that the fading statistics are always estimated, at each time instant, based on the maximum possible number of samples over which the WSS assumption remains (locally) fulfilled.

Moreover, note that the MSE converges towards some lower bound as the stationarity time duration increases. Indeed, the goodness-of-fit does not improve anymore for stationarity time durations larger than approximately 45 s (i.e. approximately 6.6 m at $\bar{v} = 7.5$ km/h). In other words, the stationarity intervals are in that case large enough so that the underlying fading statistics

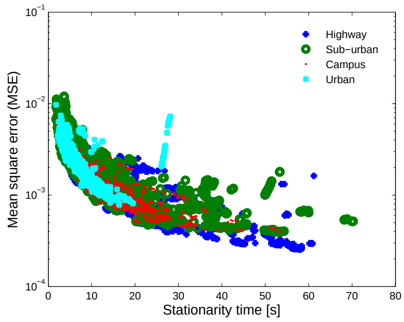

(a) For the large-scale fading.

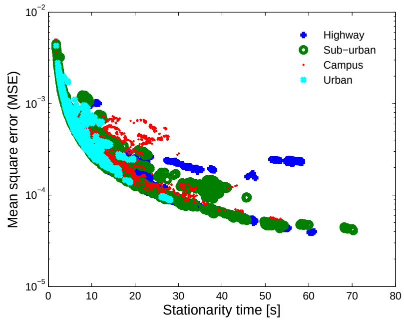

(b) For the small-scale fading.

Figure 4.5: Impact of the stationarity time duration on the median goodness-of-fit of the fading statistics in all the environments investigated during the Aalto 2007 measurement campaign).

can be reliably estimated.

4.1.3 Time- and space-varying fading statistics

The distribution of the fading statistics can now be characterized in order to account for their time (i.e. for each Tx-Rx antenna pair, their non-stationary behavior over time is investigated) and spatial (i.e. for each snapshot, their non-stationary behavior over all Tx-Rx antenna pairs is investigated) variability, respectively.

Modeling the time-varying behavior of the fading statistics

For each Tx-Rx antenna pair, the non-stationary behavior of the fading statistics is modeled using a bi-modal Gaussian distribution, with PDF given by Eq. (3.8). Fig. 4.6 shows representative distributions of the time-varying large- and small-scale fading statistics corresponding to these two states as well as the respective fitted bi-modal Gaussian distributions.

One first mode describes situations where there is a strong coherent contribution that dominates over the radio wave propagation (typically when there is a LoS component between the Tx and Rx vehicles), what corresponds to small variances and large Ricean K-factors for the large- and small-scale fading, respectively. Conversely, the other mode describes situations where there are no strong contribution that dominates over the radio wave propagation (typically when the LoS component is obstructed), what corresponds therefore to larger

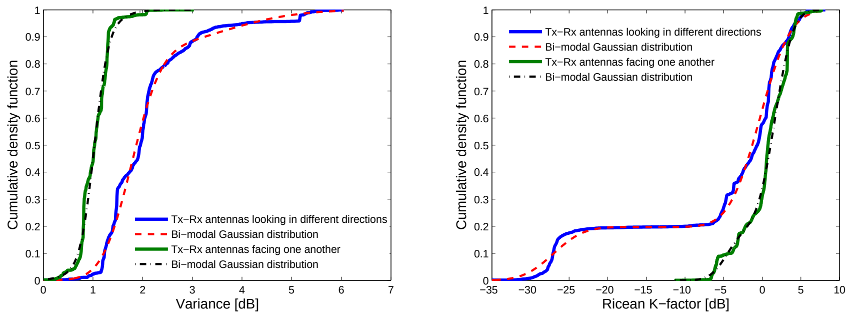

(a) For the large-scale fading. (b) For the small-scale fading.

Figure 4.6: Fitted bi-modal Gaussian distribution of the time-varying large- and small-scale fading statistics for two different Tx-Rx antenna pairs, respectively.

variances and smaller Ricean K-factors, respectively. The weights of the distribution indicate how often each of these two modes are likely to occur over time.

Modeling the space-varying behavior of the fading statistics

Since the Tx and Rx antenna arrays are semi-spherical with elements pointing in different directions, the statistical properties of the large- and small-scale fading can vary significantly from one Tx-Rx antenna pair to another. Fig. 4.7 shows the means of the bi-modal Gaussian distribution of the time-varying variance $\sigma^2_{\mathrm{LS}}(k_t\,;\,p)$ of the large-scale fading estimated for all the Tx-Rx antenna pairs. Three different subsets can be clearly characterized, i.e.

- Tx and Rx antenna elements facing one another,
- Tx and Rx antenna elements looking towards the roadsides,
- Tx and Rx antenna elements completely hidden one from another, owing to the semi-spherical geometry of the antenna arrays,

that were already identified in Section 4.1.1. For each of these antenna subsets, each parameter of the bi-modal modal Gaussian distribution can be modeled by means of a Gaussian distribution. As a consequence, the spatial distribution of the bi-modal Gaussian distribution parameters (i.e. taken over all possible Tx-Rx antenna pairs) is given by a three-modal Gaussian distribution (each of its mode characterizing a different subset of antenna elements and indicating how

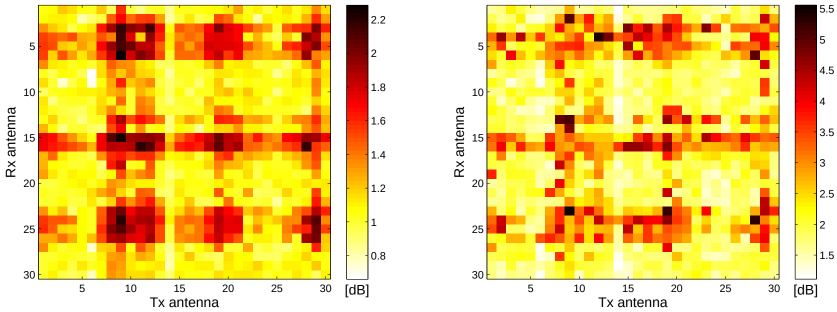

(a) Mean of the first mode: $\widehat{\mu}^{(1)}_{\sigma^2_{\text{LS}}}(p)$. (b) Mean of the second mode: $\widehat{\mu}^{(2)}_{\sigma^2_{\text{LS}}}(p)$.

Figure 4.7: Examples of parameters of the bi-modal Gaussian distributions for the variance of the large-scale fading estimated over each Tx-Rx antenna pair, in the highway environment (Aalto 2007 measurement campaign).

much the corresponding Tx-Rx antenna pairs experience either LoS or NLoS conditions). Note that similar observations can be done for the spatial distribution of the bi-modal Gaussian distribution parameters of the time-varying Ricean K-factor $K_{\text{SS}}(k_t\,;\,p)$.

4.1.4 Parameterizing the non-stationary fading model

Tables A.1 $-$ A.10 (see Appendix A) give the complete parameterizations of the spatial distributions of the variance $\sigma^2_{\text{LS}}(k_t\,;\,p)$ and the Ricean K-factor $K_{\text{SS}}(k_t\,;\,p)$, in all the environments investigated during the Aalto 2007 measurement campaign. Owing to the semi-spherical geometry of the arrays, the Tx-Rx antenna pairs facing one another almost always experience a very strong coherent contribution (since they are in LoS situations, with effectively a LoS component between the Tx and Rx sides), with Ricean K-factors up to 10 dB and variances of the large-scale fading around 1 dB. Though, note that these antenna pairs can also undergo no strong coherent contribution in the radio wave propagation (typically NLoS situations, or when other vehicles or objects are between the Tx and Rx vehicles, when one the Tx and Rx vehicles corners, etc.), hence resulting in lower K-factors around 0 dB.

On the other hand, Tx-Rx antenna pairs completely hidden one from another are found to always undergo deep NLoS situations (owing to the semi-spherical geometry of the Tx and Rx antenna arrays), with Ricean K-factors not much larger than 0 dB (and possibly as low as -25 dB) and variances of the large-scale fading ranging between 2 and 5 dB.

For each Tx-Rx antenna pair, the time-varying large- and small-scale fading statistics are estimated over narrow-band stationarity time intervals using Eqs. (4.13) $-$ (4.15)

$$\sigma^2_{\mathrm{LS}}(k_t\,;\,p) \quad K_{\mathrm{SS}}(k_t\,;\,p)$$

$$\text{where} \quad k_t = \{1, \cdots, \left\lfloor \frac{N - M/2}{\Delta_t} \right\rfloor\} \quad \text{and} \quad p = \{1, \cdots, N_{\mathrm{r}} \times N_{\mathrm{t}}\},$$

↓ **Temporal characterization**

For each Tx-Rx antenna pair, the time-varying behavior of the large- and small-scale fading statistics is modeled by means of a bi-modal Gaussian distribution (one mode describes LoS conditions, while the other one describes NLoS)

$$\sigma^2_{\mathrm{LS}}(k_t\,;\,p) \sim \sum_{i=1}^{2} \omega^{(i)}_{\sigma^2_{\mathrm{LS}}}(p)\, \mathcal{N}\left(\mu^{(i)}_{\sigma^2_{\mathrm{LS}}}(p)\,;\,\sigma^{(i)}_{\sigma^2_{\mathrm{LS}}}(p)\right)$$

$$K_{\mathrm{SS}}(k_t\,;\,p) \sim \sum_{i=1}^{2} \omega^{(i)}_{K_{\mathrm{SS}}}(p)\, \mathcal{N}\left(\mu^{(i)}_{K_{\mathrm{SS}}}(p)\,;\,\sigma^{(i)}_{K_{\mathrm{SS}}}(p)\right)$$

↓ **Spatial characterization**

Each parameter of the bi-modal Gaussian distribution is modeled over all Tx-Rx antenna pairs with a three-modal Gaussian distribution (each mode corresponds to a different configuration of Tx-Rx antenna pair, i.e. with antennas ***(i)***: facing one another, ***(ii)***: looking in different directions or ***(iii)***: hidden one from another)

$$x^{(i)}_{*}(p) \sim \sum_{j=1}^{3} \omega^{(j)}_{x}\, \mathcal{N}\left(\mu^{(j)}_{x}\,;\,\sigma^{(j)}_{x}\right) \quad \text{where} \quad x \in \{\omega, \mu, \sigma\}$$

$$* \in \{\sigma^2_{\mathrm{LS}}, K_{\mathrm{SS}}\}$$

Figure 4.8: Procedure for the stochastic characterization of the time- and space-dependent non-stationary statistics of the narrowband large- and small-scale fading.

All the other Tx-Rx antenna pairs looking in different directions experience numerous multipath components that could stem from scatterers appearing or disappearing rapidly over short time scales on the two roadsides. As a consequence, they exhibit low Ricean K-factors (typically ranging from -5 to 2 dB) and variances of the large-scale fading between 2 and 4 dB.

The procedure for the non-stationary time- and space dependent stochastic modeling of the large- and small-scale fading is summarized in Fig. 4.8.

4.2 Wideband channel modeling

Such a non-stationary modeling approach can now be extended to wideband data, for the data collected during the Aalto 2009 measurement campaign (described in Section 2.3).

4.2.1 Time-, frequency- and space-varying Ricean K-factor

As observed in Chapter 3, the US assumption can reasonably be assumed to hold over the whole measurement bandwidth, such that each delay tap can be considered as fading independently from the others. Hence, the non-stationary characterization of wideband radio propagation channels can be conducted using the same framework as the one already presented in Section 4.1.2 and summarized in Fig. 4.8, on a per frequency bin basis.

Characterizing the time-varying behavior of the Ricean K-factor

Fig. 4.9 shows the time evolution of the Ricean K-factor for the three examplary measurement scenarios that were previously investigated in Sections 3.3.1 and 3.3.2.

As pointed out in Section 4.1.2 for the fading statistics of narrowband radio propagation channels, time intervals over which the Ricean K-factor remains approximately constant can be clearly identified. This is typically the case in Figs. 4.9(c) and 4.9(d), whether it be for large Ricean K-factors between times $t = 8$ and $t = 28$ s (but also between times $t = 85$ and $t = 95$ s) or for lower Ricean K-factors between times $t = 25$ and $t = 65$ s. Remarkably, these so-identified temporal regions match very well the stationarity time intervals that were estimated for these measurement routes, provided in Fig. 3.11.

Large Ricean K-factors are typically around 8 - 10 dB (and can go up to 14 dB) and are generally obtained when there is a strong LoS component between the Tx and Rx sides. Though, this is not a sufficient condition, as shown in Fig. 4.9(c) between times $t = 74$ and $t = 82$ s. Indeed, the Ricean K-factor is found

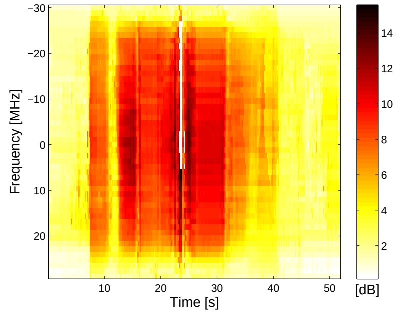

(a) Frequency- and time-varying, for opposite traveling directions.

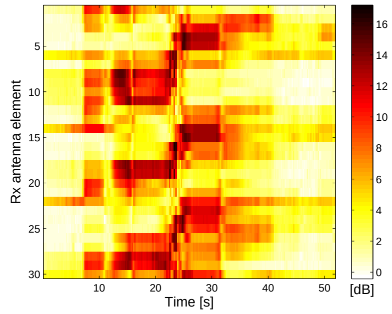

(b) Space- and time-varying, for opposite traveling directions.

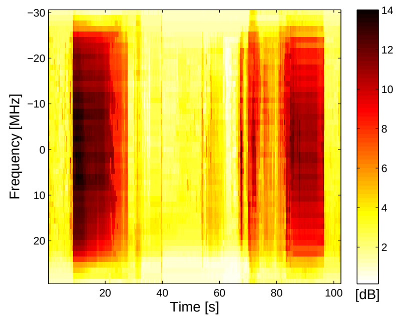

(c) Frequency- and time-varying, with occasional obstruction of the LoS component.

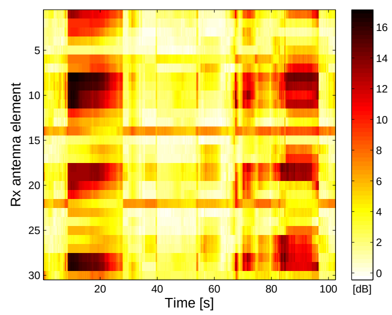

(d) Space- and time-varying, with occasional obstruction of the LoS component.

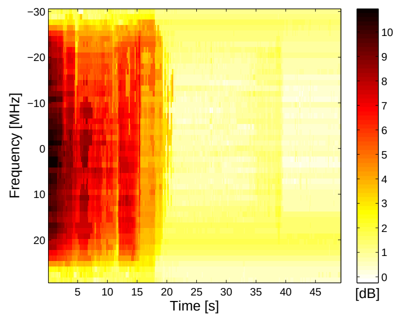

(e) Frequency- and time-varying, for different traveling directions (NLoS situation).

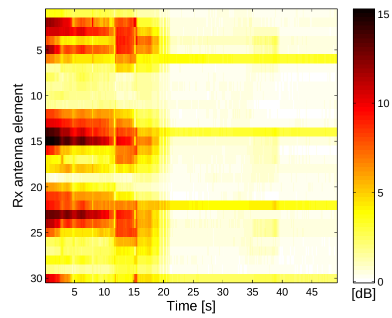

(f) Space- and time-varying, for different traveling directions (NLoS situation).

Figure 4.9: Frequency-, space- and time-varying Ricean K-factor, for three different scenarios investigated during the Aalto 2009 measurement campaign. $M = N = 20$, $\Delta_t = \Delta_f = 10$, respectively.

to drop in this case by approximately 5 dB, even if there is still a strong LoS component between the Tx and Rx sides. This is due to the fact that the Tx and Rx vehicles are at that time surrounded by a richer scattering environment, so that more multipath components are arriving at the Rx side. In that case, the diffuse component of the received signal becomes more significant in the received signal, hence yielding lower Ricean K-factors.

On the other hand, the lowest Ricean K-factors are obtained when the LoS component is obstructed and no strong coherent contribution dominates over the radio wave propagation, as shown for example in Fig. 4.9(e) when the Tx and Rx vehicles are traveling in separate directions from time $t = 18$ s until the end of the measurement run. Typical Ricean K-factors are then around 0 - 5 dB, depending on the severity of the obstruction.

Characterizing the frequency-varying behavior of the Ricean K-factor

The Ricean K-factor can also undergo significant variations over the measurement bandwidth. For example, Fig. 4.9(e) shows that the Ricean K-factor can typically fluctuate by approximately 10 dB between frequencies taken at the center and at the edges of the measurement bandwidth (the Ricean K-factor at the center of the measurement bandwidth being always larger than at its edges). This behavior is particularly emphasized when there is a LoS component between the Tx and Rx sides, as it the case between times $t = 0$ and $t = 18$s. However, this is much less evident when the LoS component is obstructed, since the Ricean K-factor varies then by only 1 or 2 dB (in maximum) between the center of the measurement bandwidth and its edges. Moreover, even though each frequency bin exhibits Ricean K-factors that can be significantly different at one given time instant, they all show the same trend over time (i.e. the Ricean K-factor increases or decreases similarly over time for all frequencies in the measurement bandwidth) as this was already observed from the narrowband non-stationary analysis in Section 4.1.2.

Even though the Ricean K-factor can vary significantly over a 60 MHz frequency bandwidth, they are found to remain approximately constant over narrower 10 MHz (IEEE 802.11p-like) bandwidth frequency sub-bands. Such a non-stationary behavior is due to the Tx and Rx antenna radiation patterns, which do not necessarily remain constant over frequency, the limited bandwidth of the measurement system as well as the non-flatness of the frequency response of the PN sequence.

Characterizing the space-varying behavior of the Ricean K-factor

Fig. 4.9(f) shows that the Ricean K-factor is strongly dependent on the relative orientation between the Tx and Rx antenna arrays. Indeed, when the Tx and Rx vehicles are traveling in the same direction (the Tx one being ahead of the Rx one) between times $t = 0$ and $t = 18$ s, then the Ricean K-factor is found to be larger for Tx-Rx antenna pairs facing one another (i.e. for Rx antennas located at the frontside of the array) than for ones hidden one from another (i.e. for Rx antennas located at the backside of the array).

This is reasonable, since the Rx antenna elements located at the frontside of the array are radiating towards the direction of motion (i.e. towards the Tx vehicle), such that they experience the strong LoS component. However, this is not the case for Rx antenna elements located either at the backside of the array or looking towards the roadsides, which undergo either deep NLoS situations (owing to the geometries of the antennas arrays) or a richer scattering environment in their radiating directions, consisting of other vehicles (either traveling or parked on the roadsides), buildings, metallic roadsigns, etc.

Furthermore, Fig. 4.9(b) shows the examplary case when the Tx and Rx vehicles are traveling in opposite direction. When the vehicles are approaching, the largest Ricean K-factors are obviously obtained for Rx antenna elements located at the frontside of the array (i.e. looking towards the direction of motion). After they passed one another, the largest Ricean K-factors are then obtained for Rx antenna elements located at the backside of the array.

4.2.2 Modeling the non-stationary Ricean K-factor

For each Tx-Rx antenna pair, the time-varying Ricean K-factor can be modeled using a bi-modal Gaussian distribution, characterizing either

- Small Ricean K-factors, which can be obtained *(i):* when the LoS component between the Tx and Rx sides is obstructed and *(ii):* in rich scattering environments when the power contribution of the multipath components is as significant as the LoS component,

- Large Ricean K-factors, which can be obtained in situations *(i):* when there is a strong LoS component between the Tx and Rx sides and *(ii):* when there are only very few scatterers in the environment surrounding the Tx and Rx vehicles.

Fig. 4.10(a) shows representative distributions of the time-varying Ricean K-factor corresponding to these two states as well as the respective fitted bi-modal Gaussian distributions. Moreover, Fig. 4.10(b) shows that the Ricean K-factor

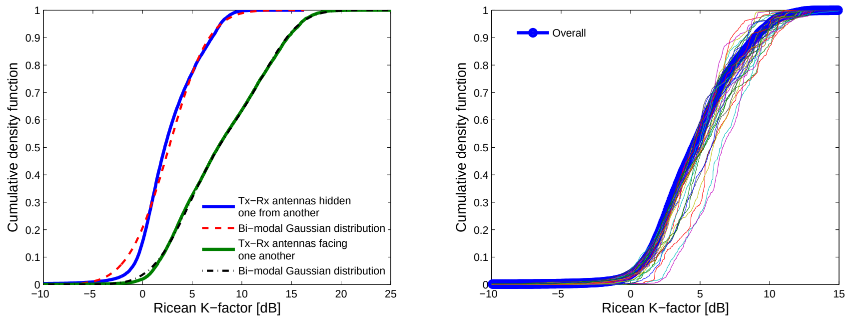

(a) For two different configurations of Tx-Rx antenna pairs.

(b) For each frequency bin, for one given Rx antenna, and over all frequency bins.

Figure 4.10: CDFs of the time-dependent Ricean K-factor and the corresponding fitted bi-modal Gaussian distribution.

estimated for each frequency bin can be described by the same distribution as the one estimated over all frequency bins. In other words, they can all be considered as different realizations of the same random process. The Ricean K-factor estimated for all frequencies can therefore be used for the joint estimation of the parameters of the bi-modal Gaussian distribution. Besides, since a ULA is used at the Tx side, its four (omnidirectional) elements experience the same scattering environment. As a consequence, one single Tx element will be considered in the following for the space- and time-varying modeling of the Ricean K-factor.

4.2.3 Parameterizing the non-stationary Ricean K-factor

Tables B.1 – B.3 (see Appendix B) provide the complete parameterization of the bi-modal Gaussian distribution for the three different sub-sets of Rx antenna elements, i.e. located *(i):* at the frontside, *(ii):* on the sides and *(iii):* at the backside of the antenna arrays, for all the environments investigated during the Aalto 2009 measurement campaign. The mode weights of the bi-modal Gaussian distribution indicate that all the Rx antenna elements, whatever their orientation with respect to the Tx side, have to cope with both LoS and NLoS situations, always in non-negligible proportions.

The smallest Ricean K-factors are obtained when the LoS component is clearly obstructed (as it is the case when the Tx and Rx vehicles are traveling in opposite directions). Otherwise, all the other investigated environments and scenarios show equivalent amount of large and small values for the Ricean K-factor, whatever the orientation of the Tx-Rx antenna pairs. This is due to the fact that the LoS component was possibly intermittently obstructed for some measurement routes (depending on the traffic conditions during the measurement runs, since other vehicles can for example come between the Tx and Rx vehicles, etc.). Moreover, the richness of the scattering environment could also have varied significantly, even within the same measurement run, owing to the traffic conditions, the nature of the scattering environment surrounding the Tx and Rx vehicles (e.g. the presence of urban furnitures, of buildings, of parkings, etc.). Hence, there are no clear distinction between the two states of the bi-modal Gaussian distributions (i.e. for the presence, or not, of a strong coherent contribution dominating over the radio wave propagation), as it can also be observed from the large standard-deviations of the bi-modal Gaussian distribution.

4.2.4 Time- and space-varying RMS delay spread

The RMS delay spread is an important measure of the fading severity and is crucial in the design of wireless communication systems. Indeed, if the RMS delay spread is larger than the length of the guard interval in OFDM, then the subcarriers are no longer orthogonal and consecutive symbols will overlap, hence causing intersymbol interference.

As for the large- and small-scale fading statistics, the RMS delay spread is usually assumed to be constant over time (under the WSS assumption). This is typically the case of the two ITU radio propagation channel models that are used in the IEEE 802.11p communication systems, which consist in taps with both fixed relative delay and average power values, as represented in Section 1.6. As a consequence, each of these two TDL models corresponds to a given RMS delay spread, which is specified to be either low (i.e. around 370 ns) or medium (i.e. around 4 µs). It is also supposed to remain constant during the whole simulation time.

However, as seen in Section 3.3.2, vehicular radio propagation channels are intrinsically non-stationary and the WSS assumption is fulfilled only within short (bounded) stationarity regions. Huence, the RMS delay spread is time-varying and its fluctuations have therefore to be characterized.

Data pre-processing

The RMS delay spread was estimated using Eq. (1.17) from PDPs averaged over a 40 wavelength sliding window, in order to filter out the small-scale fading. Moreover, a noise threshold was applied to remove spurious noise contributions that could be mistaken for multipath components. For that purpose, this threshold was set 6 dB above the noise level, which corresponds approximately to a constant false alarm rate (i.e. the probability that a noise peak is erroneously taken for a multipath component) of 1% [98].

Empirical results

Fig. 4.11 shows how much the RMS delay spread varies simultaneously over time and space, for the three examplary measurement scenarios previously investigated in Sections 3.3.1 and 3.3.2.

Looking to the results, the stronger the coherent contribution dominating over the radio wave propagation, the lower the RMS delay spread. This is typically the case in Fig. 4.11(d) between times $t = 9$ and $t = 28$ s, when there is a strong LoS component between the Tx and Rx vehicles and when multipath components arriving later at the Rx side do not contribute significantly to the radio wave propagation (since they have only low powers).

Conversely, when the LoS component is much weaker (e.g. if it is obstructed by some obstacles between the Tx and Rx vehicles) or when the surrounding scattering environment is much richer (i.e. the multipath components have much significant powers), then the RMS delay spread increases significantly. These two effects can for example be observed in Fig. 4.11(d) between times $t = 30$ and $t = 65$ s and in Fig. 4.11(f) between times $t = 0$ and $t = 10$ s, respectively.

Moreover, the RMS delay spread is strongly dependent on the relation orientation of the Tx and Rx antennas. As shown in Fig. 4.11(b), when the Tx and Rx vehicles are approaching one from another, the RMS delay spread is higher for Tx-Rx antenna pairs hidden one from another (i.e. for Rx antennas located at the backside of the array) than for ones facing one another (i.e. for Rx antennas located at the frontside of the array). Furthermore, after the Tx and Rx vehicles pass one another, the highest RMS delay spreads are then obtained for Rx antenna elements located at the frontside of the array.

4.2.5 Modeling the non-stationary RMS delay spread

For each Tx-Rx antenna pair, the time-varying RMS delay spread is modeled (in log-scale) using a bi-modal Gaussian distribution. One first mode corresponds to situations when a strong coherent contribution dominates over the radio wave propagation (typically when there is a LoS component between the two link ends and when multipath components have only negligible power), while the other one encompasses situations either when the LoS component is obstructed or when strong multipath components are experienced. These two

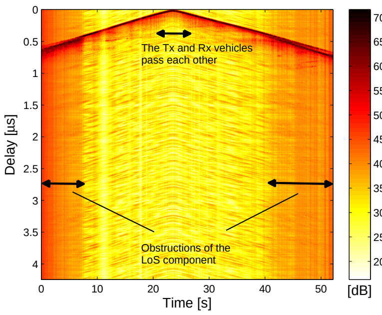

(a) Time-varying PDPs for opposite traveling directions.

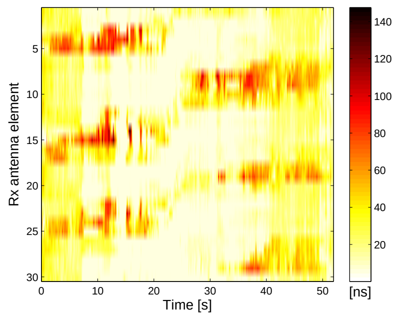

(b) RMS delay spread for opposite traveling directions.

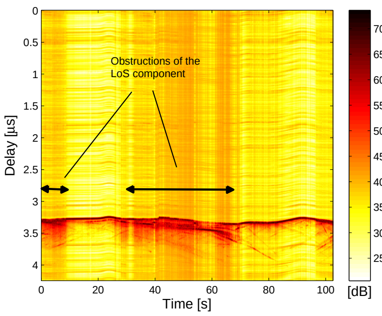

(c) Time-varying PDPs with occasional obstruction of LoS component.

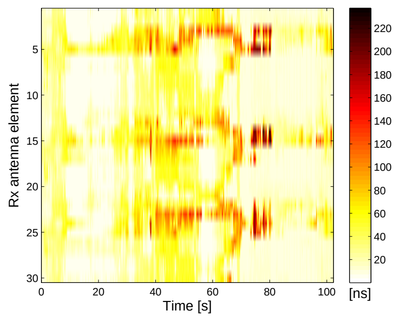

(d) RMS delay spread with occasional obstruction of LoS component.

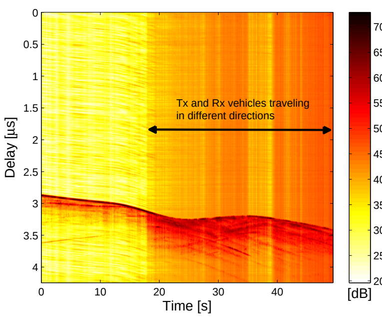

(e) Time-varying PDPs for different traveling directions (NLoS situation).

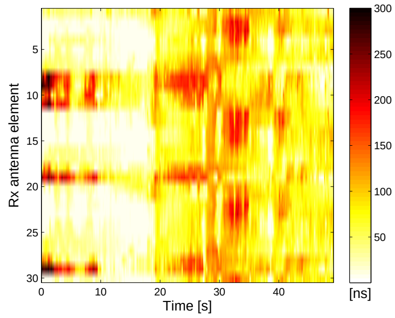

(f) RMS delay spread for different traveling directions (NLoS situation).

Figure 4.11: Time-varying PDPs and the corresponding time- and space-dependent RMS delay spread, for three different scenarios investigated during the Aalto 2009 measurement campaign. $M = 20$, $\Delta_t = 1$, respectively.

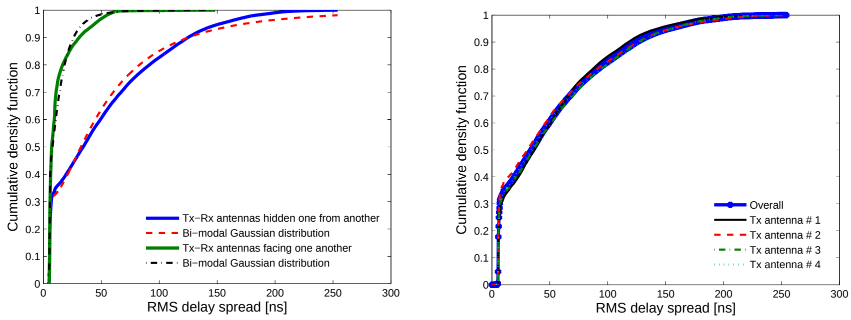

(a) For two different configurations of Tx-Rx antenna pairs.

(b) For each Tx antenna, for one given Rx antenna, and over all Tx antennas.

Figure 4.12: Distribution of the time-varying RMS delay spread and the corresponding fitted bi-modal Gaussian distributions.

modes characterize therefore small and large RMS delay spreads, respectively. Fig. 4.12(a) shows representative distributions of the time-varying RMS delay spread corresponding to these two modes as well as the respective fitted bi-modal Gaussian distributions.

Since a ULA is used at the Tx side, its four (omnidirectional) elements experience the same scattering environment, so that their RMS delay spread vary all similarly over time, as shown in Fig. 4.12(b). Hence, they can be considered as different realizations of the same random process and be used for the joint estimation of the parameters of the bi-modal Gaussian distribution.

4.2.6 Parameterizing the non-stationary RMS delay spread

Tables C.1 − C.3 (see Appendix C) provide the complete parameterization of the bi-modal Gaussian distribution for the three different sub-sets of Rx antenna elements, i.e. located *(i):* at the frontside, *(ii):* on the sides and *(iii):* at the backside of the array, for all the environments investigated during the Aalto 2009 measurement campaign. The mode weights of the bi-modal Gaussian distribution show that all the Rx antennas, whatever their orientation with respect to the Tx side, have to cope with both LoS and NLoS situations, always in non-negligible proportions.

The lowest RMS delay spreads are obtained in road crossing scenarios or when the Tx and Rx vehicles are traveling in opposite directions, since there were only very few scatterers in the surrounding environment and almost no traffic at all during these measurement runs. These lowest RMS delay spreads are most of the time obtained for Rx elements located at the frontside of the antenna array (i.e. facing the Tx side and experiencing therefore the LoS component). Though, such values can also be obtained for Rx elements located at the backside of the array, typically when the Tx and Rx vehicles are traveling in opposite directions and after passing one another, so that these antenna elements can then experience the LoS component. On the other hand, the highest RMS delay spreads are obtained in richer scattering environments, typically in the urban one or also when the Tx and Rx vehicles are traveling in separate directions. The several other vehicles traveling together with the Tx and Rx ones, buildings on the roadsides, metallic roadsigns, etc. tend indeed in that case to increase the RMS delay spread.

4.3 Conclusions and general comments

In this Chapter, the time-, frequency- and space-dependent stochastic modeling of MIMO vehicular radio propagation channels was provided. The large- and small-scale fading statistics were first extracted from narrowband vehicular radio propagation channels over the time-varying stationarity time intervals estimated in Chapter 3. Their variations over time and space were found to be strongly related to changes occuring in the scattering environment surrounding Tx and Rx vehicles (e.g. abrupt transitions between LoS and NLoS situations, etc.), and can therefore not be neglected in the realistic modeling of vehicular radio propagation channels. On the other hand, the WSS assumption is unable to describe this dynamic behavior (nor the extreme values that can be taken by the fading statistics) and was found to characterize only the average behavior of radio propagation channels. This non-stationary stochastic modeling approach was later extended to wideband vehicular radio propagation channels.

Multi-modal Gaussian distributions were used in order to model the variations of these statistics over time (each mode characterizing the presence, or not, of a strong coherent contribution in the radio wave propagation, which is usually the LoS component) and space (each mode describing a given configuration of Tx-Rx antenna pair, given the semi-spherical geometry of the antenna arrays used during the measurement campaigns), respectively.

The first- and second-order statistics of the radio propagation channel (i.e. on one hand the Ricean K-factor, the variance of the large-scale fading and on the other the RMS delay spread) were found to be strongly dependent on *(i):* the presence (or not) of a strong LoS component that dominates over the radio wave propagation, *(i):* the richness of the scattering environment surrounding the Tx and Rx vehicles, and *(iii):* the relative orientation of the Tx and Rx antenna arrays (including the impact of their radiation patterns).

CHAPTER 5

Geometry-based stochastic channel modeling

As seen in Chapters 3 and 4, vehicular radio propagation channels are intrinsically strongly non-stationary. The WSS and US assumptions were indeed found to hold only locally, within (short) bounded stationarity regions in time and frequency, respectively. Their underlying statistical properties can therefore vary significantly over time, frequency and space.

This non-stationary behavior has to be taken into account the development of realistic (and therefore reliable) vehicular radio propagation channel models. However, this is not the case of the classical TDLs that are used in IEEE 802.11p communication systems, since they rely on the (too) optimistic WSS-US assumption (each tap is indeed assumed to fade independently, with the same statistics over infinite time scales). On the other hand, a GSCM approach appears to be much more suitable, since it was shown to inherently take into account the non-stationary behavior of the radio propagation channel [73, 99], by modeling separately each multipath component (as it has already been described in Section 1.3.3).

The remainder of this Chapter is structured as follows: Section 5.1 first analyzes the main characteristics of the IRs measured in vehicular environments. Then, Section 5.2 introduces the general outline of the GSCM, which is based on the one presented in [73], including a detailed description of the discrete and diffuse scattering. The complete parameterization of this model is also provided, from the IRs collected during the Aalto 2007 measurement campaign. Section 5.3 describes the step-by-step implementation recipe as well as the validation of the proposed GSCM. Finally, Section 5.4 provides a discussion and a conclusion.

5.1 Characteristics of vehicular channels

5.1.1 Delay-time characterization

As seen in Section 1.1.1, the time-varying IRs can be divided into three different parts, namely *(i):* the LoS component that can be occasionally be ob-

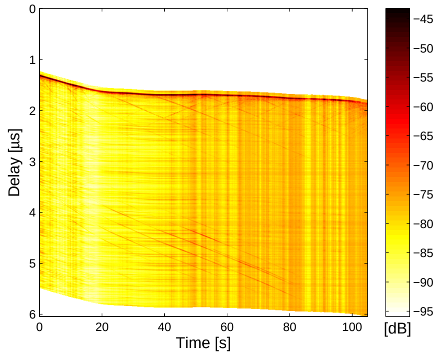

Figure 5.1: Time-varying PDPs. The Tx and Rx vehicles are traveling in the same direction in a highway environment.

structed, *(ii):* discrete scatterer contributions stemming from either static or mobile scatterers and that can drift strongly in the delay domain and *(iii):* diffuse scattering, which consists in numerous low-power contributions resulting from multiple scattering or diffraction processes that can not be associated with discrete scatterers. Fig. 5.1 shows an examplary of the time-varying PDPs in a highway environment, taken from the Aalto 2007 measurement campaign.

5.1.2 Extraction of the discrete scatterer contributions

The LoS component and the discrete scatterer contributions were identified from the time-varying PDPs averaged over all possible Tx-Rx antenna links, so that all the most significant discrete scatterer contributions are taken into account, with a Signal to Noise Ratio (SNR) high enough, and can therefore be reliably detected. For that purpose, we used a search-and-subtract procedure, very similar to the CLEAN-based one originally proposed in [100] and later refined in [73, 101], whose different steps can be summarized as follows:

- Select a number of multipath components (not necessarily consecutive) that are likely to belong to the same discrete scatterer contribution. They have to be sampled approximately every second and such that it includes the component with the strongest power,

- Interpolate (in the time domain) the so-selected multipath components in order to determine the underlying discrete scatterer contribution. Store the time-varying delay and amplitude of this contribution into vectors,

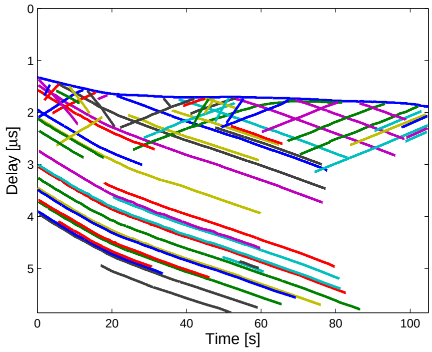

Figure 5.2: Time-varying discrete scatterer contributions at the output of the extraction procedure applied to the PDPs shown in Fig. 5.1.

- Filter out this contribution from the measured PDPs, so that no "ghost" contribution (with much weaker power, surrounding the "true" extracted ones) can later be extracted,
- Iterate until no additional discrete scatterer contribution with an average power at least 6 dB above the noise level can be identified.

All the discrete scatterer contributions are assumed to have been captured by the extraction procedure, so that the remaining "cleaned" IRs consist in diffuse scattering and noise only. Fig. 5.2 shows the different discrete scatterer contributions extracted from the measured time-varying PDPs in Fig. 5.1.

5.2 Structure of the channel model

5.2.1 General representation

Based on the previous observations, the double-directional time-varying IRs can then be expressed according to Eq. (1.7), such that

$$h(\tau\,;\,t) = h_{\mathrm{LOS}}(\tau_{\mathrm{LOS}}\,;\,t) + \sum_{p=1}^{P} h_p(\tau_p\,;\,t) + h_{\mathrm{d}}(\tau\,;\,t), \tag{5.1}$$

where P is the number of multipath components stemming from discrete either static or mobile scatterers. More specifically, the p^{th} multipath component can be modeled such that

$$h_p(\tau_p\,;\,t) = a_p(d_p)e^{j2\pi\nu_p t} \\ \times\,\delta(\tau-\tau_p)\delta(\Omega-\Omega_{\mathrm{Tx},p})\delta(\Omega-\Omega_{\mathrm{Rx},p}), \tag{5.2}$$

where $d_p = c \cdot \tau_p$ (with c the speed of light), ν_p, $\Omega_{\mathrm{Tx},p}$ and $\Omega_{\mathrm{Rx},p}$ denote its time-varying propagation distance, Doppler shift, AoD and AoA (only in terms of azimuth, since the radio wave propagation is assumed to occur only in the horizontal plane, i.e. elevation is not considered here), respectively. The complex amplitude $a_p(d_p)$ is modeled using a classical fading model, as given by Eq. (1.2), since it may consist of several unresolvable paths (i.e. arriving at the Rx side within the same delay bin, owing to the limited bandwidth of the measurement system) and includes the effects of the Tx and Rx antenna patterns. Finally, note that the LoS component can be modeled in a similar manner, by replacing the sub-index p by LoS in Eq. (5.2).

5.2.2 Modeling of the radio wave propagation

As already mentioned in Section 1.3.3, the GSCM approach is a trade-off between the simplicity of the stochastic models and the accuracy of the deterministic tools. In other words, it has on one hand to be relatively easy to parameterize (and thus tractable in an implementation point of view), and on the other to still be able to reproduce the main (non-stationary) physical characteristics of real-world vehicular radio propagation channels.

Very simplified ray-tracing methods are therefore considered regarding the modeling of the radio wave propagation mechanisms. In the following, we will indeed assume that

- The Tx and Rx vehicles are traveling at constant speeds v_{Tx} and v_{Rx}, respectively, along a straight route in the same (or opposite) direction in a two-dimensional environment, such that the relative orientation of the Tx and Rx antenna patterns (due to the movement of the Tx and Rx vehicles) remains constant over time,

- The discrete mobile scatterers are moving at constant speeds v_p parallel to the Tx and Rx vehicles, without further traffic modeling,

- Only single-bounced reflections are considered, as they have been found to be the most significant propagation mechanism in vehicular radio propagation channels [34, 73].

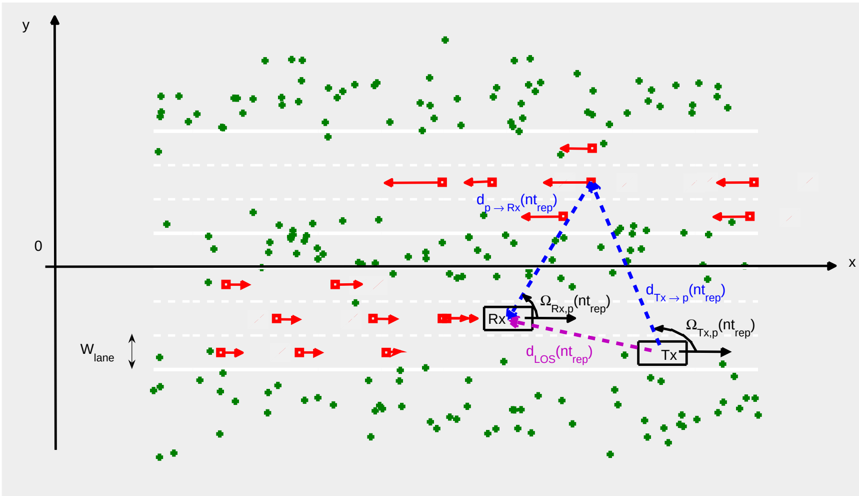

Figure 5.3: Simplified two-dimensional geometry of the scattering environment for the modeling of the radio wave propagation. The green crosses (resp. red squares) correspond to discrete static (resp. mobile) scatterers. The arrows indicate the direction of motion of the vehicles (adapted from [73]).

As a consequence, the time-variant propagation delay τ_p (or, equivalently, the propagation distance d_p) and Doppler shift ν_p of the discrete scatterer contributions can be determined by the simple geometry relationships

$$\begin{cases} \tau_p = \tau_{\text{Tx}\rightarrow p}(t) + \tau_{p\rightarrow\text{Rx}}(t) \\ \nu_p = \dfrac{1}{\lambda}\left[(v_{\text{Tx}} - v_p)\cos\Omega_{\text{Tx},p} + (v_{\text{Rx}} - v_p)\cos\Omega_{\text{Rx},p}\right]. \end{cases} \tag{5.3}$$

Similar relationships can also be derived for the LoS component, by replacing the sub-index p by LoS. The number of discrete static (resp. mobile) scatterers in the simulated environment is given by the density $\chi_{p,s}$ (resp. $\chi_{p,m}$). Hence, using the two-dimensional environment geometry in Fig. 5.3, which is similar to the one in [73], we can generate

- Static discrete scatterers on roadsides (and on the highway median strip). Their *x*- and *y*-coordinates are drawn from continuous uniform and multivariate normal distributions respectively, i.e. $x_{p,d} \sim \mathcal{U}(x_{d,\text{min}}, x_{d,\text{max}})$ and $y_{p,d} \sim L^{-1}\sum_{l=1}^{L}\mathcal{N}(\mu_{d,l}, \xi_d)$. L denotes here the number of strips of discrete scatterer contributions: $L = 2$ in the campus, urban and suburban environments (i.e. it corresponds to the two road sides), whereas

Table 5.1: Parameterization of the radio wave propagation aspects.

		Unit	Campus	Urban	Sub-urban	Highway
Road parameters	N_{lanes}	-	4	2	4	7
	W_{lane}	[m]	2.75			
Scatterer densities	$\chi_{p,s}$	[m^{-1}]	0.12	0.13	0.12	0.10
	$\chi_{p,m}$	[m^{-1}]	0.03	0.05	0.03	0.08
Scatterer "birth/death"	$\mu_{b/d}$	[m]	4.80			5.26
	$\xi_{b/d}$	[m]	0.78			0.99
Static discrete scatterers	$\mu_{d,l=1}$	[m]	$\pm(N_{\text{lanes}}/2+1)W_{\text{lane}}$			
	$\mu_{d,l=2}$	[m]				
	$\mu_{d,l=3}$	[m]	-	-	-	0
	ξ_d	[m]	2			

$L = 3$ in the highway environment (i.e. it corresponds to the two road sides as well as the median strip),

- Mobile discrete scatterers on the road lanes. As for static discrete scatterers, their initial *x*-coordinates are drawn from a continuous uniform distribution, whereas their *y*-coordinates are drawn from a discrete uniform distribution (with a number of outcomes equal to the total number of lanes N_{lanes}, each of width W_{lane}). Furthermore, they are assigned a (realistic) constant speed along the *x*-axis, drawn from a truncated Gaussian distribution, such that too high (or negative, on a wrong road lane) speeds are avoided.

The "birth/death" of the discrete scatterer contributions in the delay domain can be modeled by means of their maximum excess propagation distance (taken with respect to the LoS component) that was found to be best described by a lognormal distribution with mean $\mu_{b/d}$ and standard-deviation $\xi_{b/d}$, respectively. All the parameters for the modeling of the radio wave propagation aspects in each environment are summarized in Table 5.1.

5.2.3 Parameterizing the discrete scatterer contributions

As previously mentioned, the time-varying complex amplitude of the p^{th} discrete scatterer contribution can be modeled using the fading model given by

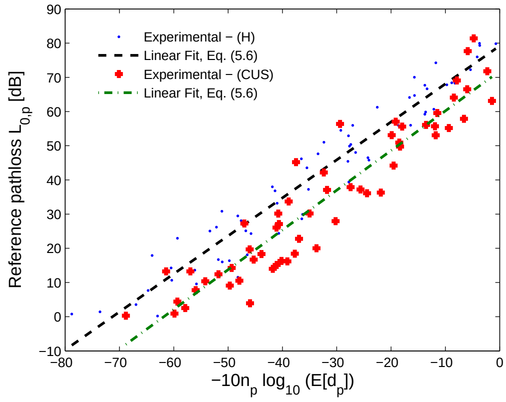

Figure 5.4: Reference pathloss $L_{0,p}$ depending on the propagation distance for the discrete scatterer contributions in the (H) and (CUS) environments.

Eq. (1.2), such that [73]

$$a_p \triangleq \underbrace{P_p^{1/2}}_{1)} \underbrace{g_p e^{j\phi_p}}_{2)} . \tag{5.4}$$

The LoS component is modeled similarly, the sub-index p being only replaced by LoS. The two processes in Eq. (5.4) are, respectively

1. **The time-varying average power of the discrete scatterer contribution**. It is obtained by low-pass filtering the amplitude $|a_p(d_p)|^2$ with a 40λ sliding-average window [97], assuming that the Tx and Rx vehicles are traveling with an average speed $\bar{v} = 7.5$ km/h.

   The power of the low-pass filtered signal is normalized with respect to the one of the LoS component and can be modeled (in the dB scale) as

$$10 \log_{10} \frac{P_p}{P_{\text{LOS}}} = -\left[L_{0,p} + 10 n_p \log_{10}(d_p) + S_p\right], \tag{5.5}$$

   where $L_p = L_{0,p} + 10 n_p \log_{10}(d_p)$ and S_p correspond to the (distance-dependent) pathloss and the (stochastic) large-scale fading, respectively. As a result, a pathloss exponent $n_p > 0$ and the corresponding pathloss reference power $L_{0,p} > 0$ were extracted for each discrete scatterer contribution, as well as a number of S_p values.

   Over all the extracted discrete scatterer contributions, the pathloss exponent n_p is found to be uniformly distributed, i.e. $n_p \sim \mathcal{U}(0, n_{\max})$.

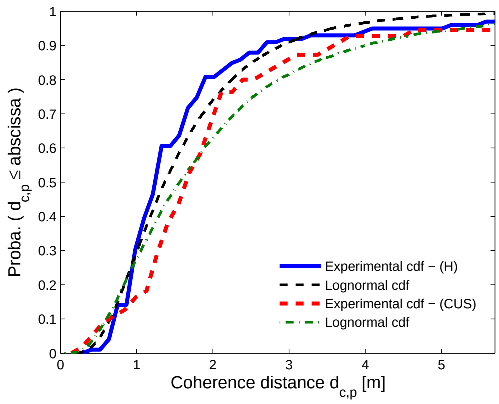

Figure 5.5: CDFs of the large-scale fading coherence distance $d_{c,p}$ for the discrete scatterer contributions in the (H) and (CUS) environments.

Moreover, Fig. 5.4 shows that $L_{0,p}$ can be modeled such that

$$L_{0,p} \sim 10\eta_{\Lambda_0} \log_{10} \left(E\left[d_p\right]^{-n_p} \right) + \Lambda_0, \tag{5.6}$$

where Λ_0 is a Gaussian random variable with mean μ_{Λ_0} and standard-deviation ξ_{Λ_0}. For the LoS component, the exponent n_{LoS} is arbitrarily fixed to 1.8 as reported in [13], as the inter-vehicle distance remained almost constant in all the routes (owing to the fact that the Tx and Rx vehicles were always traveling at approximately the same speed during the measurement runs).

On the other hand, over all the extracted LoS components and discrete scatterer contributions, the large-scale fading S_p is modeled (in the dB scale) by a Gaussian random process, with autocorrelation function [73]

$$r_p(\Delta d) = \sigma_{S,p}^2 e^{-\log 2 (\Delta d / d_{c,p})^2}, \tag{5.7}$$

where $\sigma_{S,p}$ and $d_{c,p}$ denote the standard-deviation and the 0.5-coherence distance of the Gaussian process, respectively. Fig. 5.5 shows that the coherence distance $d_{c,p}$ is lognormally distributed (with mean μ_c and standard-deviation ξ_c), whereas the standard-deviation $\sigma_{S,p}$ is log-correlated with $d_{c,p}$, i.e.

$$\log \sigma_{S,p} \sim \eta_S \log\left(d_{c,p}\right) + K_S, \tag{5.8}$$

where K_S denotes a Gaussian random variable with mean $\mu_S = \log \sigma_{S,0}$ and standard-deviation ξ_S,

Table 5.2: Number of "valid" discrete scatterer contributions (and routes) in all the environments investigated during the Aalto 2007 measurement campaign.

Campus	Urban	Sub-urban	Highway
10 (4)	1 (3)	16 (6)	67 (5)

2. **The time-varying small-scale fading** $g_p e^{j\phi_p}$. It corresponds to the out filtered signal when using the 40λ sliding average window. Its envelope g_p is a white process over time that can be modeled using the flexible Weibull distribution.

   Its shape parameter β_p is found to be Gaussian distributed (with mean μ_β and standard-deviation ξ_β). Moreover, since the average power of the small-scale fading is normalized to one, its scale parameter α_p is then deterministically given by $\alpha_p = 1/\sqrt{\Gamma(1 + 2/\beta_p)})$. On the other hand, the phase ϕ_p is uniformly distributed from 0 to 2π.

Regarding the parameterization of the discrete scatterer contributions, it has to be noted that only contributions spanning over sufficiently large distances are used for the extraction of reliable distance-dependent pathloss parameters (the other ones being discarded). Using the same criterion as in [73], their relative distances have indeed to be such that $(d_{p,\text{max}} - d_{p,\text{min}})/(d_{p,\text{max}} + d_{p,\text{min}}) \geq 0.1$. Moreover, discrete scatterer contributions with pathloss parameters that do not verify the conditions associated with Eq. (5.5) are discarded as they would introduce unrealistic propagation effects (i.e. with either negative pathloss exponents or reference powers).

The total number of "valid" discrete scatterer contributions extracted from the measured IRs in each environment is summarized in Table 5.2. Owing to their relative scarcity in some of the environments, only two aggregated environments will be considered in the following, i.e. the highway (H) environment and the campus / urban / sub-urban (CUS) areas. All parameters regarding the modeling of the discrete scatterer contributions the in (H) and (CUS) environments are provided in Table 5.3.

5.2.4 Parameterizing the diffuse scattering

Unlike [73] where the diffuse scattering is modeled by considering "walls" diffuse scatterers located on the roadsides, a purely stochastic approach is chosen here, so that

$$h_d(\tau\,;\,t) \triangleq \underbrace{\psi_d^{1/2}(\tau\,;\,t)}_{1)}\underbrace{g_d(\tau)e^{j\phi_d}}_{2)}, \tag{5.9}$$

Table 5.3: Parameterization of the discrete scatterer contributions in the (H) and (CUS) environments, from the Aalto 2007 measurement campaign.

			Unit	(CUS)	(H)
Pathloss	Exponent n_p	$n_{\max}$	-	3.00	3.05
	Reference pathloss $L_{0,p}$	η_{Λ_0}	-	1.16	1.11
		μ_{Λ_0}	[dB]	71.83	79.20
		ξ_{Λ_0}	[dB]	7.37	5.76
	Exponent n_{LoS}	-	-	1.80	
	Reference pathloss $L_{0,\mathrm{LoS}}$	-	[dB]	0	
Large-scale fading	Coherence distance $d_{c,p}$	μ_c	[m]	0.44	0.31
		ξ_c	[m]	0.74	0.58
	Standard-deviation $\sigma_{S,p}$	η_S	-	0.56	0.38
		$\sigma_{S,0}$	[dB]	2.32	2.32
		ξ_S	-	0.25	0.27
Small-scale fading	Weibull shape parameter β_p	μ_β	-	2.05	1.97
		ξ_β	-	0.20	0.20

v where the two processes are, respectively

1. **The time-varying large-scale power** $\psi_d(\tau\,;\,t)$. It decays exponentially (in the dB scale) in the delay domain, as shown in Fig. 5.6, i.e.

$$\psi_{d,[\mathrm{dB}]}(\tau\,;\,t) = \psi_{d,0} + \begin{cases} 0, & \tau < \tau_d \\ (\psi_{d,1} - \psi_{d,0})/2, & \tau = \tau_d \\ (\psi_{d,1} - \psi_{d,0})e^{-B_d(\tau-\tau_d)}, & \tau > \tau_d \end{cases}, \quad (5.10)$$

where $\psi_{d,1}$, $\psi_{d,0}$, B_d and τ_d are the maximum power, noise level, decay factor and base delay of the diffuse large-scale power, respectively. This model was first proposed in [102] for the description of the diffuse large-scale power in natural values, while it was later modified in [103] to account for the sampled bandwidth-limited effects of the measurement system.

The parameters of the large-scale power are estimated with a non-linear least-square estimator, as described in [103]. The maximum power $\psi_{d,1}$ of the diffuse scattering is found to be correlated with the LoS distance, as reported in [101, 103] and as shown in Fig. 5.7, such that

$$\psi_{d,1} \sim \psi_{0,1} + 10\eta_{\Psi,1}\log_{10}(d_{\mathrm{LOS}}) + \Psi_1, \quad (5.11)$$

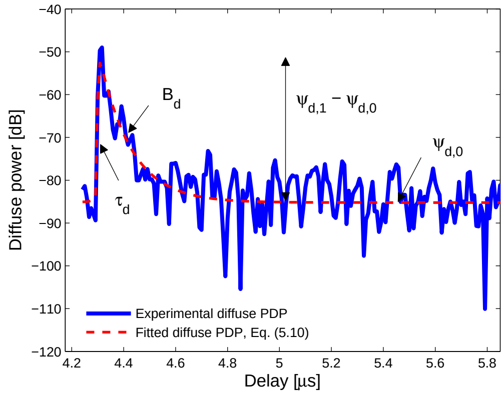

Figure 5.6: Exemplary diffuse large-scale power and the corresponding least-square estimate in the (H) environment.

where Ψ_1 is an exponentially correlated Gaussian random variable with zero-mean, standard-deviation $\xi_{\Psi,1}$ and 0.5-coherence distance $d_{\Psi,1}$, respectively. The noise level $\psi_{d,0}$ of the diffuse scattering is modeled similarly, by replacing the sub-index 1 by 0 in Eq. (5.11). The two Gaussian variables Ψ_0 and Ψ_1 are also correlated, with coefficient $\langle \Psi_0, \Psi_1 \rangle$. The decay factor B_d is found to increase exponentially with the diffuse peak-to-noise ratio, such that

$$\log B_d \sim \log \left(e^{(\psi_{d,1} - \psi_{d,0})/\psi_B} - 1 \right) + K_B, \tag{5.12}$$

where K_B is a Gaussian random variable with mean $\mu_B = \log B_0$ and standard-deviation ξ_B. Finally, the base-delay τ_d of the diffuse large-scale power is found to be highly correlated with the delay of the LoS component, such that

$$\tau_d = \tau_0 + \eta_\tau \tau_{\mathrm{LOS}}. \tag{5.13}$$

Note that the base delay can start immediatly with the LoS component, owing to diffuse scatterers located around the Tx or Rx vehicles within one single delay bin (i.e. 2.5 m in our measurement set-ups, when operating at 5.3 GHz), so that their contributions are arriving at the Rx side with the LoS component. Moreover, when the LoS component is obstructed, the strongest peak of the time-varying diffuse PDPs is even likely to come slightly before the LoS component, such that τ_0 can be negative.

2. **The small-scale fading** $g_d(\tau)e^{j\phi_d}$. Its envelope can be modeled for each

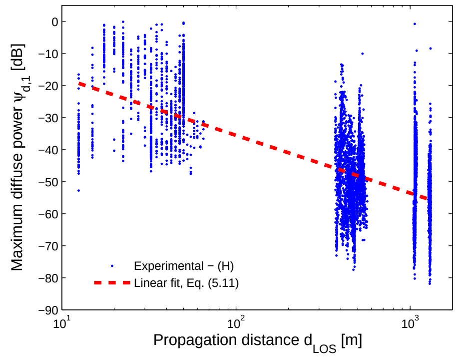

Figure 5.7: Maximum power $\psi_{d,1}$ of the diffuse scattering depending on the propagation distance in the (H) environment.

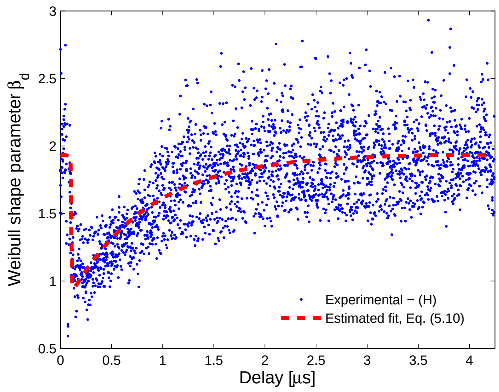

Figure 5.8: Weibull shape parameter β_d of the diffuse small-scale fading depending on the propagation delay in the (H) environment.

delay by the flexible Weibull distribution, with shape parameter $\beta_d(\tau)$, whereas its phase ϕ_d is uniformly distributed between 0 and 2π.

Fig. 5.8 shows that the shape parameter β_d can be described using the same model as the one given by Eq. (5.10), with a parameter set $\theta_\beta = [\beta_1 \;\; \beta_0 \;\; B_\beta \;\; \tau_\beta]$. Note that τ_β can also be defined with respect to the delay of the LoS component, such that $\tau_\beta = \tau_{\text{LOS}} + \Delta\tau_\beta$. A Gaussian random variable with zero-mean and standard-deviation ξ_β was also accounted. As it can be observed, the severity of the diffuse small-scale fading can change from "worse than Rayleigh" (typically around the LoS component) to Rayleigh (as the delay increases, i.e. $\beta_d \to 2$ when

Table 5.4: Parameterization of the diffuse scattering in the (H) and (CUS) environments, from the Aalto 2007 measurement campaign.

			Unit	(CUS)	(H)
Large-scale power	Maximum power $\psi_{d,1}$	$\psi_{0,1}$	[dB]	7.93	0.41
		$\eta_{\Psi,1}$	-	- 2.03	- 1.80
		$\xi_{\Psi,1}$	[dB]	11.07	11.29
		$d_{\Psi,1}$	[m]	6.93	5.73
	Noise level $\psi_{d,0}$	$\psi_{d,0}$	[dB]	-37.51	-29.49
		$\eta_{\Psi,0}$	-	- 1.80	- 2.07
		$\xi_{\Psi,0}$	[dB]	5.82	5.36
		$d_{\Psi,0}$	[m]	12.34	11.38
		$\langle \Psi_0, \Psi_1 \rangle$	-	0.56	0.43
	Decay factor B_d	ψ_B	[dB]	25.02	26.10
		B_0	[MHz]	14.94	15.12
		ξ_B	-	0.32	0.41
	Base delay τ_d	τ_0	[ns]	- 28.64	- 26.64
		η_τ	-	1.00	1.00
Small-scale fading	Shape parameter β_d	β_1	-	1.10	1.04
		β_0	-	2.01	1.94
		B_β	[MHz]	1.34	1.30
		$\Delta\tau_\beta$	[ns]	- 15.41	24.00
		ξ_β	-	0.26	0.26
	Scale parameter α_d	μ_α	-	1.31	1.29
		ξ_α	-	0.26	0.24

$\tau \to \infty$). On the other hand, the scale parameter α_d is found to be Gaussian distributed, with mean μ_α and standard-deviation ξ_α.

Regarding the parameterization of the diffuse scattering, it has to be observed that it was done from the residual IRs (i.e. what remains after filtering out the detected LoS component and all the discrete scatterer contributions from the measured IRs), according to Eq. (5.1).

Parameter sets $\theta_d = [\psi_{d,1} \;\; \psi_{d,0} \;\; B_d \;\; \tau_d]$ with a maximum power $\psi_{d,1}$ larger than the discrete peak power were discarded, since the detection of the discrete scatterer contributions would then not be possible. All the parameters for the modeling of the diffuse scattering model in (H) and (CUS) environments are provided in Table 5.4.

5.3 Validation of the GSCM

We provide in this Section the procedure to simulate this radio propagation channel model as well as its validition, by comparing its performances with the ones obtained from the measured data.

5.3.1 Implementation recipe

In order to generate realizations of this vehicular GSCM, the following steps have to be followed:

1. Determine the temporal (resp. delay) resolution t_{rep} (resp. $\Delta\tau$) as well as the total time duration and delay range of the simulation (i.e. the number$N$ and K of snpashots and delay bins, respectively),

2. Specify the initial *x*- and *y*-coordinates of the Tx and Rx vehicles as well as their velocities v_{Tx} and v_{Rx}. Generate discrete static (resp. mobile) scatterers, with density $\chi_{p,s}$ (resp. $\chi_{p,m}$) and assign them (initial) *x*- and *y*-coordinates (as well as velocities for the mobile ones),

3. Estimate at each time instant the relative positions of the discrete scatterers with respect to the Tx and Rx vehicles in the simulated environment (assuming uniform linear motion along the *x*-axis only, for the Tx and Rx vehicles as well as for the discrete mobile scatterers),

4. Estimate at each time instant the propagation distance d_p, the AoDs $\Omega_{\text{Tx},p}$ and AoAs $\Omega_{\text{Rx},p}$ for the LoS component and each single-bounced reflection on the discrete scatterers. Draw a value of the maximum excess propagation distance for each multipath component, in order to simulate their respective "birth/death" in the delay domain,

5. Draw pathloss, large- and small-scale fading statistics for the LoS component and each discrete scatterer contribution, given their respective propagation distance d_p (or d_{LOS}), according to Section 5.2.3 and with parameterization given in Table 5.3. Generate the corresponding time-varying complex amplitudes using Eq. (5.4),

6. Draw diffuse large-scale power (resp. diffuse small-scale fading) statistics at each time instant (resp. each delay tap), according to Section 5.2.4 and with parameterization given in Table 5.4. Generate the corresponding time-varying complex diffuse scattering using Eq. (5.9),

7. Sum up at the Rx side the so-generated LoS component, discrete scatterer contributions (including the bandlimited filter effects of the measurement system) and diffuse scattering, according to Eq. (5.1).

If MIMO radio propagation channels are to be simulated, then the characteristics of the MIMO system under consideration have to be specified as well (including the number of antenna elements at both link ends, their relative positions, their radiation patterns, their polarizations, etc.)

5.3.2 Comparison with measurements

The model validation can therefore be carried out by comparing metrics estimated from measured (based on the 2007 Aalto measurement campaign) and simulated (through Monte-Carlo iterations) channel realizations in the (CUS) and (H) environments. For that purpose, three different metrics were considered either in the delay- or time-domain, namely

RMS delay spread

Fig. 5.9(a) shows the distributions of the measured and simulated RMS delay spreads. The simulated average RMS delay spreads of 58.90 and 63.99 μs are found to be in pretty good agreement with the measured ones of 60.88 and 59.82 μs in both the (H) and (CUS) environments, respectively. Moreover, the Root Mean Square Errors (RMSEs) between the measured and simulated CDFs in these two environments are of 2.36% and 5.94%, respectively.

First-order statistics of the equivalent narrowband channel gain

Fig. 5.9(b) shows a good match between the measured and simulated CDFs of the SISO narrowband radio propagation channel gain in the (H) and (CUS) environments. Indeed, the measured and simulated distributions match pretty well in terms of median, with a difference of 0.59 and 1.70 dB in the (H) and (CUS) environments, respectively. Moreover, the RMSE between the measured and simulated CDFs in these two environments are of 4.77% and 3.23%, respectively. Note that the gap between the measured and simulated CDFs in the (H) environment is due to one specific measurement route where the distance between the Tx and Rx vehicles was much smaller than for the other ones, hence resulting in a higher envelope level.

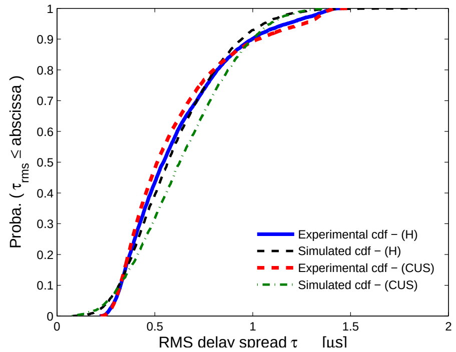

(a) RMS delay spread.

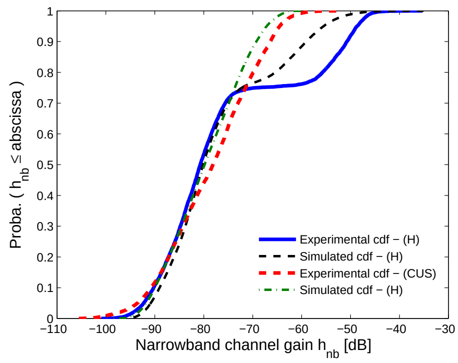

(b) Narrowband channel gain.

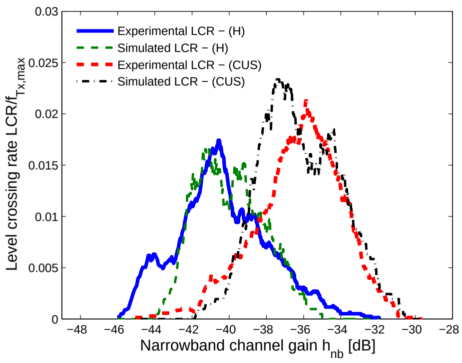

(c) Examplary normalized LCR of the equivalent narrowband envelope.

Figure 5.9: Validation metrics of the vehicular GSCM, for measured and simulated channel realizations in the (H) and (CUS) environments.

Level crossing rate

The Level Crossing Rate (LCR) characterizes the dynamics of the equivalent narrowband radio propagation channel over time. It is estimated from its large-scale variations only, since the small-scale fading process of the discrete scatterer contributions can be undersampled (they can indeed exhibit Doppler shifts larger than the maximum resolvable one $\nu_{\max}$, which is limited to only 7.15 Hz for the measurement settings of the Aalto 2007 measurement campaign). As a result, for a fair comparison, both the measured and simulated narrowband channels were low-pass filtered with a 40λ sliding-average window, in order to remove the small-scale fading. Fig. 5.9(c) shows that the proposed GSCM is able to generate realizations of the radio propagation channel with LCR very similar to the one that can be estimated for measurement routes in the (H) and (CUS) environments. Besides, note that this validation can be done here only for specific simulated realizations of the GSCM and measurement routes, since

- The size of the measurement data set is relatively small, so that it may not necessarily be representative of all the temporal dynamics that could be expected in real-world radio propagation channels,
- The outcome of the GSCM strongly depends on how the discrete scatterers evolve in the environment surrounding the Tx and Rx vehicles as well as on their strength, for which over-simplifying modeling assumptions were considered.

It is therefore relatively difficult to obtain a good overall agreement between measured and simulated LCRs.

Hence, it is reasonable to assess the validity of the proposed vehicular SISO GSCM based on these three metrics, as they have not been directly used for its parameterization. Moreover, the comparison between the measured and simulated metrics shows that the model proposed in this paper is well suited for the modeling of vehicular radio propagation channels, despite the simplifying approximations that have been assumed (e.g. a simplified model for the scattering environment, only single-bounced reflections, etc.).

5.4 Conclusions and general comments

In this Chapter, a vehicular GSCM was presented, based on an extensive measurement campaign conducted in different environments. Such an modeling approach appears to be particularly well-suited for the modeling non-stationary radio propagation channels, since each discrete scatterer is defined and characterized separately. Indeed, the radio wave propagation is modeled for each discrete scatterer contribution based on the assumption of single-bounced reflection processes, leading therefore to a simplified geometry with lower complexity than ray-tracing methods. On the other hand, the scattering aspects are described stochastically using a classical fading model. Besides, the diffuse scattering is characterized in a purely stochastic manner and included in the proposed GSCM approach.

Even though the framework of the proposed model relies on the one proposed in [73] (especially regarding the modeling of the LoS component as well as of the discrete multipath components), the main differences are that

- We model and parameterize the fading for the LoS component and the discrete multipath components in a purely stochastic manner,
- We model and parameterize the diffuse scattering in a purely stochastic manner, based on the approach proposed in [102].

The proposed vehicular GSCM was then completely parameterized, such that it can be easily implemented and simulated. Interestingly, its values stand relatively well those reported in [73], with very similar behaviors for the model parameters, despite a (sometimes significantly) different parameterization procedure based on another measurement data set (in terms of investigated environments and scenarios, antenna arrays used at the Tx and Rx sides, etc.). As a consequence, the proposed GSCM approach corroborates the pertinency of the one previously presented in [73].

Finally, validation showed that this model was able to well reproduce characteristics of measured SISO radio propagation channels, whether it be in the delay or in the time domain. Deviations between the measurement-based and the GSCM performances can mostly be explained by the different simplifying hypotheses which are underlying the GSCM, especially regarding

- The spatial distribution of the discrete scatterer contributions in the environment surrounding the Tx and Rx vehicle, since they are (unrealistically) assumed to be uniformly distributed either on the roadsides (for the static ones) or on the roads (for the mobile ones), without taking into account more physical distributions.
- The temporal behavior of the Tx and Rx vehicles as well as of the discrete mobile scatterers over time, since they are assumed to always travel along a straight line at the same constant speed,

- The purely stochastic modeling of the diffuse scattering, which does therefore have no real physical signification.

Although this GSCM was validated only for SISO systems (since the patterns of the measurement antennas were not known exactly), it could be easily generalized to MIMO systems, by considering appropriate antenna patterns.

CHAPTER 6
Conclusion

Summary of my contributions

Up to now, classical cellular wireless networks have been designed based on a stationarity assumption, which consists in saying that the statistics of the underlying radio propagation channels do not change neither over time nor frequency nor space. Most of the algorithms that are currently used at the Tx and Rx sides are designed under this assumption of stationarity, especially regarding the feedback of information from the Rx to the Tx side (so that this latter can adapt its transmission scheme accordingly). The fed back information should indeed correspond to the current state of the radio propagation channel over which the signal will be transmitted [27, 92, 93, 94]. However, such an approach is no longer valid in intrinsically rapidly time-varying (non-stationary) environments, such as the ones in which vehicular wireless communication systems are supposed to operate. Hence, this opens the door to new radio propagation channel models, that would describe this specific feature. Already existing algorithms could then be improved by taking into account the non-stationary description of radio propagation channel statistics.

With that perspective, we investigated in this thesis the non-stationary behavior of vehicular MIMO radio propagation channels, in order to establish appropriate models. For that purpose, two measurement campaigns were conducted in collaboration with Aalto University in 2007 and 2009, respectively. Different environments and scenarios that are very specific to vehicular radio communication systems (and more specifically to ITS safety-related applications) were extensively investigated.

After revisiting the popular WSS, US and H assumptions (which characterize the stationarity over time, frequency and space, respectively), the spatial structure of the MIMO radio propagation channel was shown to be subject to significant changes due to the dynamic scattering environment surrounding the Tx and Rx vehicles. Based on these observations, the validity of the WSS and US assumptions was assessed by means of the CMD, which characterizes the amount of change in the spatial structure of MIMO radio propagation channels. Using appropriate threshold values, stationarity regions were then identified in both time and frequency (over which the WSS and US assumptions locally hold, respectively). Typical stationarity distances and frequency bandwidth were estimated to be approximately 10 to 40 m long (depending on the environment or scenario under investigation) and 40 to 50 MHz wide (i.e. almost the whole measurement bandwidth), respectively. Hence, it can be concluded that US assumption is not violated within the 10 MHz bandwidth of IEEE 802.11p communication systems, whereas the WSS assumption holds only over very short time intervals. In other words, the WSS assumption is much more strongly violated than the US assumption in vehicular radio propagation channels.

Besides, the stochastic characterization of non-stationary radio propagation channels was considered over time, frequency and space, respectively. The large- and small-scale fading statistics were first extracted from narrowband vehicular radio propagation channels over time-varying stationarity time intervals. Their variations over time and space were found to be strongly related to changes occuring in the scattering environment surrounding Tx and Rx vehicles. These variations of the fading statistics should not be ignored. The WSS assumption is therefore definitely unable to describe such a dynamic behavior, since it was shown to describe only the average temporal behavior of non-stationary radio propagation channels. This non-stationary stochastic modeling approach was later extended to wideband (60 MHz) vehicular radio propagation channels, for which it was applied on a per frequency basis. Moreover, multi-modal Gaussian distributions were used in order to represent the distribution of

- The time-varying fading statistics. In this case, two different states were considered, depending on the presence (or not) of a LoS component that dominates the radio wave propagation as well as on the richness of the scattering environment that is surrounding the Tx and Rx vehicles. Rich scattering environments (or with NLoS conditions) were indeed found to yield the smallest Ricean K-factors and the largest RMS delay spreads. Conversely, environments with very few scatterers (or with a strong LoS component) were found to be characterized by larger Ricean K-factors and smaller RMS delay spreads, respectively,

- The space-varying fading statistics. In this case, three different states were considered, each corresponding a given configuration of Tx-Rx antenna pairs, depending on their relative orientation (i.e. if they radiate or not in the same directions). Given the semi-spherical geometry of the Tx and Rx antenna arrays that were used during our measurement campaigns, the smallest Ricean K-factors and the largest RMS delay spreads were obtained for antenna pairs completely hidden one from another (since they do not experience the LoS component). On the other hand, Tx-Rx antenna pairs facing one another are those with the largest Ricean K-factors and the smallest RMS delay spreads. Tx-Rx antenna pairs looking towards the roadsides correspond to an intermediate case, for which the Ricean K-factors and the RMS delay spreads mostly depend on the relative orientation of the Tx and Rx vehicles as well as of the illuminated scatterers on the roadsides.

Finally, a GSCM was proposed for the modeling of non-stationary vehicular radio propagation channels. In that case, each scatterer is defined and characterized: the radio wave propagation was indeed modeled using very simplified ray-tracing methods, while the scattering aspects were described stochastically using a classical fading model. A purely stochastic description of the diffuse scattering was also included in the GSCM, which has a definitely much lower complexity (for simulation purposes) than the "walls" of diffuse scatterers that are used in [73]. Moreover, the proposed GSCM approach was completely parameterized, with values and trends very similar to the ones reported in [73], and positively validated for SISO systems.

What about non-stationary performances?

Arriving at that point of the work, it is important to remember that building models for radio propagation channels is not an achievement in itself, but simply the first step when building wireless communication systems.

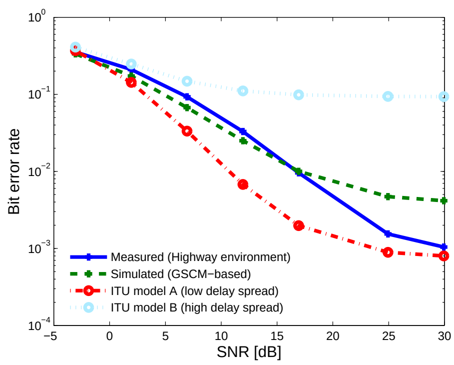

Figure 6.1: Bit error rate performances of IEEE 802.11p wireless communication systems obtained for different radio propagation channel models, in a highway environment.

Fig. 6.1 shows a representative example of the benefit that can be expected when taking into account the non-stationarities of the vehicular radio propagation channel in the evaluation of the IEEE 802.11p physical layer performance. As it can be observed, the GSCM that we proposed in this thesis outperforms the TDLs that are used in the IEEE 802.11p communication systems, such as the International Telecommunication Union (ITU) radio propagation channel models (A) and (B) which rely on the very restrictive WSS-US assumption, regarding the prediction of the achievable system performances (in that case in terms of achievable BER).

It has however to be kept in mind that such non-stationary models are more complex to handle than the ones that are already implemented in real-world communication systems. The question is now to decide if the trade-off between the accuracy and the complexity of these models is significant enough to push their implementations in the design of those real-world communication systems, in place of the already existing ones.

Recommendations for radio communication systems

Taking into account the non-stationary behavior of inter-vehicular radio propagation channels is therefore absolutly crucial. Three different cases can be considered, depending on whether it is to be used in

- Off-line analysis, when stationarity intervals have to be identified from data collected during a complete measurement route (as done in Chapter 3). This information can then be used in order to investigate the non-stationary behavior of the radio propagation channel, e.g. the time-, frequency- and space-dependency of the underlying fading statistics (as done in Chapter 4),

- Off-line emulators, in order to design and/or validate *(i):* (parts of) IEEE 802.11p based communication systems or *(ii):* dedicated algorithms for such systems. In that case, we require models that are able to reliably reproduce real-world radio propagation channels (especially regarding their non-stationary behavior).

  For that purpose, a GSCM approach similar to the one proposed in Chapter 5 could be purposely considered, since it is definitely simpler and faster (but yet less accurate) than ray-tracing techniques, while more accurate (but yet more complex) than other usual stochastic radio propagation channel models (e.g. TDLs). Moreover, such a model can easily be extended to additional environments or scenarios (by simply plugging the appropriate model parameters), integrate more elaborate traffic models, consider any arbitrary (SISO, MIMO) antenna pattern at the Tx and Rx sides, etc. depending on the users' needs,

- Real-world embedded communication systems, so as to be used in adaptive algorithms (e.g. for the optimization of the feedback rate between the Tx and Rx sides, etc). In that case, the characterization of stationarity time intervals (as previously described in Chapter 3) requires the knowledge of the spatial structure of the underlying MIMO radio propagation channel at future time instants (what is clearly not possible for such real-time applications, since this information is obviously not yet available at a given time instant).

  As a result, some algorithms (or some alternative system architectures) have for example to be considered in order to reliably predict the future state of the underlying MIMO radio propagation channel that will be undergone, with an horizon as far as possible (so that very large stationarity regions can be detected). Based on this information, stationarity time intervals, over which the WSS assumption (which was found to be the most critical one in vehicular environments) will remain valid, could then be identified.

In other words, the identification of stationarity intervals can for the moment be addressed only in the context of off-line applications, when the spatial structure of the underlying MIMO radio propagation channel is available at each single time instant (whether it be in the past or in the future). Regarding real-time applications, the procedure (as previously described in Chapter 3) cannot be used directly as such, since the future behavior of the radio propagation channel is unavailable and has therefore first to be somehow predicted, in an as accurate manner as possible.

What's next?

The analysis of the non-stationary behavior of vehicular radio propagation channels opens the door to different open questions that could be addressed for future possible work in that direction, for example

- To determine more precisely the improvement in the system performances that can be expected when taking into account the non-stationary behavior of radio propagation channels (Fig. 6.1 being simply an appetizer in that perspective). To turn it in another way, how can we optimize the already existing algorithms in order to take advantage of this non-stationary behavior?

  We could for example think to adaptive beamforming applications, so that information would be transmitted in the directions in the environment maximizing the stationarity of the experienced radio propagation channel, etc.

- To not only rely on statistical models for characterizing the non-stationary behavior of radio propagation channels, as this was almost always done in the literature up to now, whether it be throughout this thesis or in the work conducted by other research groups (to the best of my best knowledge). It would indeed be interesting to get a more in-depth understanding of the physical phenomena from which non-stationarity originates. Hence, next steps in that directions could for example consist of the analysis of the non-stationarity on a per-scatterer basis, in order to understand how much (and under which conditions) each of them contributes to the overall non-stationary behavior of the radio propagation channel (this latter being now well characterized), whether it be related to the way it moves in the environment surrounding the Tx and Rx, to their scattering properties, etc.

  However, this could also consist in characterizing how much the characteristics of real-world wireless communication systems (regarding the number of antennas at both link ends, the polarization, the bandwidth, the antenna radiation patterns, etc.) can impact the non-stationary behavior of the radio propagation channel over which it communicates.

  In other words, this would consist in proposing deterministic explanations of the non-stationary behavior of radio propagation channels,

- To extend the concept of non-stationarity to next generation wireless communication multi-user systems, including (non exhaustively) relaying applications, cognitive radio, etc. Indeed, the non-stationarity has up to now been considered only for single link systems, when one transmitter communicates with one receiver. The definition of the concept of non-stationarity in the context of multi-user systems is not necessarily straightforward: according to what reference could we define it? For each link separately? Or from a system point of view (i.e. by jointly considering all the links)?

As it can be seen, the question of the non-stationarity is just popping up (since the last few years), and a lot of groundbreaking work is therefore left to do.

APPENDIX **A**

Parameterizing the narrowband fading statistics

This Appendix provides the complete parameterization of the three-modal Gaussian distributions used for the spatial modeling (i.e. taken over all the antenna pairs between the Tx-Rx semi-spherical arrays) of the time-varying large- and small-scale fading statistics respectively (in all the environments investigated during the Aalto 2007 measurement campaign).

Table A.1: Estimated parameters of the bi-modal Gaussian distribution for $\widehat{\omega}^{(1)}_{K_{\mathrm{SS}}}(p)$ [1].

	$i=1$			$i=2$			$i=3$		
	$\widehat{\omega}_1$	$\widehat{\mu}_1$	$\widehat{\sigma}_1$	$\widehat{\omega}_2$	$\widehat{\mu}_2$	$\widehat{\sigma}_2$	$\widehat{\omega}_3$	$\widehat{\mu}_3$	$\widehat{\sigma}_3$
Campus (4 routes)	0.38	0.04	0.02	0.32	0.11	0.05	0.30	0.57	0.20
Urban (3 routes)	0.28	0.04	0.02	0.55	0.18	0.09	0.17	0.39	0.17
Sub-urban (6 routes)	0.57	0.08	0.04	0.31	0.20	0.07	0.12	0.38	0.15
Highway (5 routes)	0.43	0.07	0.04	0.26	0.17	0.07	0.30	0.46	0.18

[1] The weight of the distribution second mode can be obtained as $\widehat{\omega}^{(2)}_{K_{\mathrm{SS}}}(p) = 1 - \widehat{\omega}^{(1)}_{K_{\mathrm{SS}}}(p)$.

Table A.2: Estimated parameters of the bi-modal Gaussian distribution for $\widehat{\mu}^{(1)}_{K_{\mathrm{SS}}}(p)$.

	$i=1$			$i=2$			$i=3$		
	$\widehat{\omega}_1$	$\widehat{\mu}_1$	$\widehat{\sigma}_1$	$\widehat{\omega}_2$	$\widehat{\mu}_2$	$\widehat{\sigma}_2$	$\widehat{\omega}_3$	$\widehat{\mu}_3$	$\widehat{\sigma}_3$
Campus (4 routes)	0.33	-24.58	1.66	0.32	-16.31	4.65	0.34	-1.82	2.90
Urban (3 routes)	0.45	-25.34	1.52	0.29	-18.04	4.31	0.26	-3.64	4.11
Sub-urban (6 routes)	0.62	-24.75	1.50	0.31	-16.59	5.73	0.07	2.83	0.89
Highway (5 routes)	0.33	-24.58	1.66	0.32	-16.31	4.65	0.34	-1.82	2.90

Table A.3: Estimated parameters of the bi-modal Gaussian distribution for $\widehat{\mu}^{(2)}_{K_{\mathrm{SS}}}(p)$.

	$i=1$			$i=2$			$i=3$		
	$\widehat{\omega}_1$	$\widehat{\mu}_1$	$\widehat{\sigma}_1$	$\widehat{\omega}_2$	$\widehat{\mu}_2$	$\widehat{\sigma}_2$	$\widehat{\omega}_3$	$\widehat{\mu}_3$	$\widehat{\sigma}_3$
Campus (4 routes)	0.55	0.51	0.70	0.38	1.95	0.93	0.07	5.77	1.19
Urban (3 routes)	0.41	-0.42	0.83	0.45	1.39	1.01	0.15	2.24	2.48
Sub-urban (6 routes)	0.47	-0.66	0.62	0.40	0.12	0.51	0.13	4.36	1.86
Highway (5 routes)	0.50	0.41	0.70	0.43	1.51	0.83	0.07	6.30	0.90

Table A.4: Estimated parameters of the bi-modal Gaussian distribution for $\widehat{\sigma}^{(1)}_{K_{\mathrm{SS}}}(p)$.

	$i=1$			$i=2$			$i=3$		
	$\widehat{\omega}_1$	$\widehat{\mu}_1$	$\widehat{\sigma}_1$	$\widehat{\omega}_2$	$\widehat{\mu}_2$	$\widehat{\sigma}_2$	$\widehat{\omega}_3$	$\widehat{\mu}_3$	$\widehat{\sigma}_3$
Campus (4 routes)	0.46	2.32	1.04	0.27	5.58	1.35	0.27	9.60	1.53
Urban (3 routes)	0.54	3.27	1.13	0.23	6.11	1.21	0.22	9.36	1.48
Sub-urban (6 routes)	0.56	3.07	0.86	0.25	4.98	1.21	0.18	9.28	1.51
Highway (5 routes)	0.48	2.51	1.06	0.29	5.06	1.18	0.22	9.77	1.74

Table A.5: Estimated parameters of the bi-modal Gaussian distribution for $\widehat{\sigma}^{(2)}_{K_{\mathrm{SS}}}(p)$.

	$i=1$			$i=2$			$i=3$		
	$\widehat{\omega}_1$	$\widehat{\mu}_1$	$\widehat{\sigma}_1$	$\widehat{\omega}_2$	$\widehat{\mu}_2$	$\widehat{\sigma}_2$	$\widehat{\omega}_3$	$\widehat{\mu}_3$	$\widehat{\sigma}_3$
Campus (4 routes)	0.42	1.86	0.37	0.39	2.25	0.54	0.18	2.70	1.16
Urban (3 routes)	0.28	1.91	0.49	0.50	2.53	0.46	0.22	3.11	0.85
Sub-urban (6 routes)	0.09	1.43	0.41	0.62	2.90	0.38	0.28	3.35	0.65
Highway (5 routes)	0.20	1.44	0.62	0.55	2.63	0.52	0.24	2.79	0.93

Table A.6: Estimated parameters of the bi-modal Gaussian distribution for $\widehat{\omega}^{(1)}_{\sigma^2_{\mathrm{LS}}}(p)$ 2.

	$i=1$			$i=2$			$i=3$		
	$\widehat{\omega}_1$	$\widehat{\mu}_1$	$\widehat{\sigma}_1$	$\widehat{\omega}_2$	$\widehat{\mu}_2$	$\widehat{\sigma}_2$	$\widehat{\omega}_3$	$\widehat{\mu}_3$	$\widehat{\sigma}_3$
Campus (4 routes)	0.38	0.49	0.15	0.38	0.71	0.08	0.24	0.88	0.04
Urban (3 routes)	0.17	0.41	0.14	0.41	0.66	0.08	0.42	0.82	0.05
Sub-urban (6 routes)	0.11	0.34	0.10	0.51	0.58	0.09	0.39	0.65	0.10
Highway (5 routes)	0.17	0.46	0.15	0.35	0.70	0.09	0.47	0.86	0.07

Table A.7: Estimated parameters of the bi-modal Gaussian distribution for $\widehat{\mu}^{(1)}_{\sigma^2_{\mathrm{LS}}}(p)$.

	$i=1$			$i=2$			$i=3$		
	$\widehat{\omega}_1$	$\widehat{\mu}_1$	$\widehat{\sigma}_1$	$\widehat{\omega}_2$	$\widehat{\mu}_2$	$\widehat{\sigma}_2$	$\widehat{\omega}_3$	$\widehat{\mu}_3$	$\widehat{\sigma}_3$
Campus (4 routes)	0.41	0.95	0.12	0.36	1.14	0.14	0.23	1.49	0.25
Urban (3 routes)	0.47	0.89	0.10	0.32	1.20	0.17	0.21	1.61	0.23
Sub-urban (6 routes)	0.59	0.93	0.10	0.19	1.05	0.16	0.22	1.62	0.21
Highway (5 routes)	0.57	1.05	0.09	0.29	1.41	0.14	0.14	1.84	0.18

Table A.8: Estimated parameters of the bi-modal Gaussian distribution for $\widehat{\mu}^{(2)}_{\sigma^2_{\mathrm{LS}}}(p)$.

	$i=1$			$i=2$			$i=3$		
	$\widehat{\omega}_1$	$\widehat{\mu}_1$	$\widehat{\sigma}_1$	$\widehat{\omega}_2$	$\widehat{\mu}_2$	$\widehat{\sigma}_2$	$\widehat{\omega}_3$	$\widehat{\mu}_3$	$\widehat{\sigma}_3$
Campus (4 routes)	0.33	1.22	0.13	0.46	2.02	0.42	0.21	2.72	0.57
Urban (3 routes)	0.31	1.79	0.29	0.51	2.13	0.36	0.18	2.53	0.54
Sub-urban (6 routes)	0.49	1.88	0.26	0.31	2.01	0.20	0.20	2.98	0.36
Highway (5 routes)	0.61	1.82	0.24	0.26	2.86	0.41	0.12	3.97	0.63

Table A.9: Estimated parameters of the bi-modal Gaussian distribution for $\widehat{\sigma}^{(1)}_{\sigma^2_{\text{LS}}}(p)$.

	$i=1$			$i=2$			$i=3$		
	$\widehat{\omega}_1$	$\widehat{\mu}_1$	$\widehat{\sigma}_1$	$\widehat{\omega}_2$	$\widehat{\mu}_2$	$\widehat{\sigma}_2$	$\widehat{\omega}_3$	$\widehat{\mu}_3$	$\widehat{\sigma}_3$
Campus (4 routes)	0.29	0.21	0.03	0.28	0.31	0.06	0.42	0.32	0.12
Urban (3 routes)	0.22	0.24	0.02	0.49	0.29	0.09	0.29	0.40	0.11
Sub-urban (6 routes)	0.35	0.32	0.08	0.39	0.32	0.03	0.26	0.55	0.10
Highway (5 routes)	0.74	0.26	0.08	0.08	0.41	0.02	0.18	0.47	0.06

Table A.10: Estimated parameters of the bi-modal Gaussian distribution for $\widehat{\sigma}^{(2)}_{\sigma^2_{\text{LS}}}(p)$.

	$i=1$			$i=2$			$i=3$		
	$\widehat{\omega}_1$	$\widehat{\mu}_1$	$\widehat{\sigma}_1$	$\widehat{\omega}_2$	$\widehat{\mu}_2$	$\widehat{\sigma}_2$	$\widehat{\omega}_3$	$\widehat{\mu}_3$	$\widehat{\sigma}_3$
Campus (4 routes)	0.40	0.25	0.09	0.37	0.55	0.12	0.22	0.83	0.18
Urban (3 routes)	0.39	0.41	0.10	0.41	0.56	0.11	0.20	0.72	0.21
Sub-urban (6 routes)	0.31	0.41	0.08	0.39	0.55	0.20	0.29	0.69	0.21
Highway (5 routes)	0.46	0.29	0.12	0.30	0.59	0.14	0.24	0.94	0.19

APPENDIX B

Parameterizing the Ricean K-factor

This Appendix provides the complete parameterization of the bi-modal Gaussian distribution used for the modeling of the time-varying Ricean K-factor, for all the scenarios investigated during the Aalto 2009 measurement campaign.

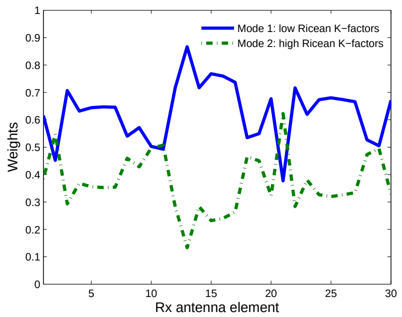

(a) Weights of the Gaussian modes.

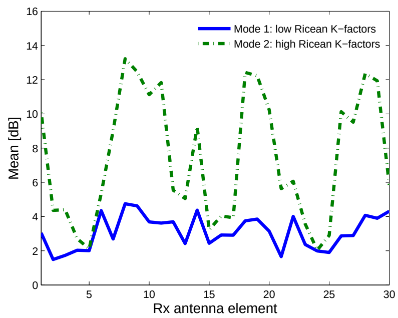

(b) Means of the Gaussian modes.

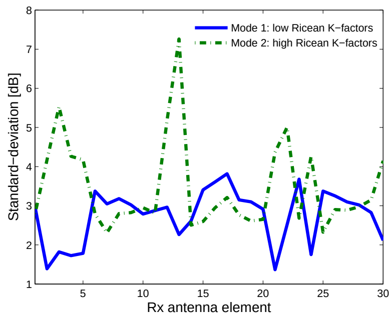

(c) Standard-deviation of the Gaussian modes.

Figure B.1: Parameters of the bi-modal Gaussian distribution estimated for all the Rx antenna elements, when the LoS component between the Tx and Rx vehicles is occasionally obstructed (Aalto 2009 measurement campaign).

Fig. B.1 shows how the parameters of the bi-modal Gaussian distribution estimated for all the elements of the Rx antenna array, when the LoS component between the Tx and Rx vehicles is occasionally obstructed (see Table 2.2 for the link to antenna mapping and Fig. 2.2(b) for the antenna positions in the array, respectively).

Three different cases can be identified, namely for elements located *(i):* at the frontside, *(ii):* on the sides and *(iii):* at the backside of the Rx antenna array. The average parameters of the bi-modal Gaussian distribution are provided in Tables B.1 $-$ B.3 for each of these three Rx antenna subsets, respectively.

Table B.1: Rx antennas located at the frontside of the array.

		$i=1$			$i=2$		
		$\widehat{\omega}_1$	$\widehat{\mu}_1$	$\widehat{\sigma}_1$	$\widehat{\omega}_2$	$\widehat{\mu}_2$	$\widehat{\sigma}_2$
Underground parkings	Median [dB]	0.66	2.86	2.01	0.34	9.19	6.20
(3 routes)	Std. [dB]	0.81	0.92	0.74	0.08	1.38	1.66
Road crossings	Median [dB]	0.66	4.27	3.38	0.34	7.88	3.82
(2 routes)	Std. [dB]	0.13	1.12	1.13	0.13	3.47	1.39
Urban environment	Median [dB]	0.52	3.73	3.21	0.48	10.90	2.52
(2 routes)	Std. [dB]	0.05	0.75	0.60	0.05	2.52	0.50
Opposite directions	Median [dB]	0.72	2.35	3.22	0.28	10.18	2.81
(3 routes)	Std. [dB]	0.07	0.58	0.40	0.07	2.66	1.12
Different directions	Median [dB]	0.53	0.47	0.93	0.47	1.27	1.74
(1 route)	Std. [dB]	0.21	0.77	0.75	0.21	1.93	0.97
Static-to-mobile	Median [dB]	0.63	4.03	3.14	0.37	10.38	3.32
(1 route)	Std. [dB]	0.13	0.92	0.61	0.13	1.91	1.15
Same direction + LoS	Median [dB]	0.47	4.04	2.34	0.53	13.27	2.74
(8 routes)	Std. [dB]	0.06	0.62	0.17	0.06	2.32	0.33
Same direction + NLoS	Median [dB]	0.56	3.77	2.89	0.44	11.47	2.89
(7 routes)	Std. [dB]	0.09	0.45	0.30	0.09	2.84	0.91

Table B.2: Rx antennas located on the sides of the array.

		$i=1$			$i=2$		
		$\widehat{\omega}_1$	$\widehat{\mu}_1$	$\widehat{\sigma}_1$	$\widehat{\omega}_2$	$\widehat{\mu}_2$	$\widehat{\sigma}_2$
Underground parkings	Median [dB]	0.45	4.60	4.10	0.55	6.37	2.64
(3 routes)	Std. [dB]	0.19	1.92	2.21	0.19	3.40	1.14
Road crossings	Median [dB]	0.66	4.27	3.38	0.34	7.88	3.82
(2 routes)	Std. [dB]	0.13	1.12	1.13	0.13	3.47	1.39
Urban environment	Median [dB]	0.62	2.98	3.44	0.38	7.39	2.38
(2 routes)	Std. [dB]	0.21	3.08	1.58	0.21	1.43	0.55
Opposite directions	Median [dB]	0.66	2.77	3.38	0.34	9.57	2.96
(3 routes)	Std. [dB]	0.11	0.84	0.65	0.11	3.78	1.46
Different directions	Median [dB]	0.54	0.42	0.69	0.46	4.05	2.11
(1 route)	Std. [dB]	0.10	0.64	0.48	0.10	2.21	0.98
Static-to-mobile	Median [dB]	0.61	3.79	3.74	0.39	5.80	2.81
(1 route)	Std. [dB]	0.26	1.70	1.98	0.26	3.49	1.58
Same direction + LoS	Median [dB]	0.55	3.14	2.13	0.45	9.64	2.68
(8 routes)	Std. [dB]	0.10	0.74	0.27	0.10	3.11	0.86
Same direction + NLoS	Median [dB]	0.63	2.98	2.99	0.37	9.14	2.93
(7 routes)	Std. [dB]	0.14	1.04	0.73	0.14	3.31	1.42

Table B.3: Rx antennas located at the backside of the array.

		$i=1$			$i=2$		
		$\widehat{\omega}_1$	$\widehat{\mu}_1$	$\widehat{\sigma}_1$	$\widehat{\omega}_2$	$\widehat{\mu}_2$	$\widehat{\sigma}_2$
Underground parkings	Median [dB]	0.82	2.70	1.70	0.18	4.15	5.89
(3 routes)	Std. [dB]	0.17	1.21	1.16	0.17	1.82	1.69
Road crossings	Median [dB]	0.56	5.50	5.36	0.43	8.79	4.28
(2 routes)	Std. [dB]	0.10	1.01	1.46	0.10	2.06	1.39
Urban environment	Median [dB]	0.53	1.77	3.43	0.47	2.42	2.14
(2 routes)	Std. [dB]	0.30	2.62	2.60	0.30	2.65	1.66
Opposite directions	Median [dB]	0.79	3.81	3.77	0.21	11.06	3.15
(3 routes)	Std. [dB]	0.12	0.73	0.42	0.12	3.21	1.16
Different directions	Median [dB]	0.54	0.57	0.66	0.45	6.34	2.98
(1 route)	Std. [dB]	0.06	0.40	0.25	0.06	2.03	0.92
Static-to-mobile	Median [dB]	0.77	2.28	4.48	0.23	3.70	2.76
(1 route)	Std. [dB]	0.35	6.91	2.06	0.35	3.33	2.20
Same direction + LoS	Median [dB]	0.65	2.36	1.97	0.35	7.42	4.48
(8 routes)	Std. [dB]	0.19	0.60	0.32	0.19	1.81	1.36
Same direction + NLoS	Median [dB]	0.67	2.20	3.31	0.33	3.40	2.92
(7 routes)	Std. [dB]	0.05	0.78	0.87	0.05	2.37	1.04

APPENDIX C
Parameterizing the RMS delay spread

This Appendix provides the complete parameterization of the bi-modal Gaussian distribution used for the modeling of the time-varying RMS delay spread (in the log-scale), for all the scenarios investigated during the Aalto 2009 measurement campaign.

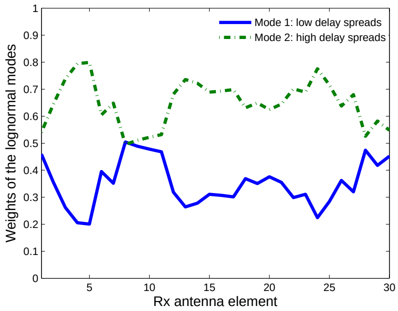

(a) Weights of the Gaussian modes.

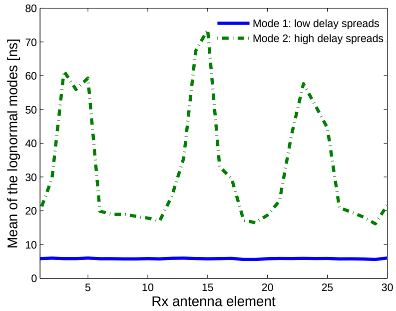

(b) Means of the Gaussian modes.

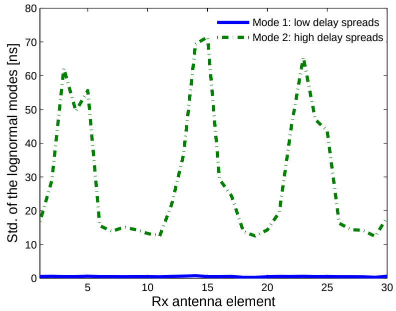

(c) Standard-deviations of theGaussian modes.

Figure C.1: Parameters of the bi-modal Gaussian distribution estimated for all the Rx antenna elements, when the LoS component between the Tx and Rx vehicles is occasionally obstructed (Aalto 2009 measurement campaign).

Fig. C.1 shows how the parameters of the bi-modal Gaussian distribution estimated for all the elements of the Rx antenna array, when the LoS component between the Tx and Rx vehicles is occasionally obstructed (see Table 2.2 for the link to antenna mapping and Fig. 2.2(b) for the antenna positions in the array, respectively). For clarity reasons, note that we provide here the means and standard-deviations of the lognormal modes.

Three different cases can thus be identified, namely for elements located *(i):* at the frontside, *(ii):* on the sides and *(iii):* at the backside of the Rx antenna array. The average parameters of the bi-modal Gaussian distribution are provided in Tables C.1 $-$ C.3 for each of these three Rx antenna subsets, respectively.

Table C.1: Rx antennas located at the frontside of the array.

		$i=1$			$i=2$		
		$\widehat{\omega}_1$	$\widehat{\mu}_1$	$\widehat{\sigma}_1$	$\widehat{\omega}_2$	$\widehat{\mu}_2$	$\widehat{\sigma}_2$
Underground parkings	Median [ns]	0.39	6.84	1.21	0.61	13.03	8.22
(3 routes)	Std. [ns]	0.35	2.22	1.72	0.35	14.93	15.57
Road crossings	Median [ns]	0.37	5.92	0.53	0.63	35.55	25.21
(2 routes)	Std. [ns]	0.17	0.13	0.07	0.17	7.88	7.50
Urban environment	Median [ns]	0.72	7.90	2.40	0.28	52.20	36.49
(2 routes)	Std. [ns]	0.11	0.20	0.18	0.11	7.73	9.38
Opposite directions	Median [ns]	0.44	6.37	0.75	0.56	32.94	22.88
(3 routes)	Std. [ns]	0.12	0.11	0.08	0.12	9.83	9.92
Different directions	Median [ns]	0.19	34.78	42.04	0.81	105.13	59.69
(1 route)	Std. [ns]	0.05	18.86	27.44	0.05	21.39	10.80
Static-to-mobile	Median [ns]	0.33	5.96	0.55	0.67	31.62	26.68
(1 route)	Std. [ns]	0.05	0.09	0.06	0.05	6.09	6.97
Same direction + LoS	Median [ns]	0.66	5.67	0.41	0.34	45.62	60.69
(8 routes)	Std. [ns]	0.07	0.04	0.03	0.07	12.92	22.44
Same direction + NLoS	Median [ns]	0.43	5.75	0.47	0.56	18.09	13.78
(7 routes)	Std. [ns]	0.06	0.14	0.06	0.06	2.80	3.37

Table C.2: Rx antennas located on the sides of the array.

		$i=1$			$i=2$		
		$\widehat{\omega}_1$	$\widehat{\mu}_1$	$\widehat{\sigma}_1$	$\widehat{\omega}_2$	$\widehat{\mu}_2$	$\widehat{\sigma}_2$
Underground parkings	Median [ns]	0.36	9.47	3.15	0.64	22.73	15.70
(3 routes)	Std. [ns]	0.31	3.55	2.79	0.31	18.08	16.95
Road crossings	Median [ns]	0.53	5.96	0.56	0.47	25.92	21.24
(2 routes)	Std. [ns]	0.14	0.14	0.06	0.14	7.83	9.51
Urban environment	Median [ns]	0.45	7.70	2.33	0.55	45.94	37.63
(2 routes)	Std. [ns]	0.25	3.02	3.64	0.25	19.69	21.08
Opposite directions	Median [ns]	0.46	6.30	0.71	0.54	29.21	20.36
(3 routes)	Std. [ns]	0.14	0.13	0.08	0.14	8.64	9.17
Different directions	Median [ns]	0.19	6.03	0.61	0.81	82.51	51.04
(1 route)	Std. [ns]	0.08	9.69	15.40	0.08	16.70	10.25
Static-to-mobile	Median [ns]	0.32	6.05	0.60	0.68	33.09	28.03
(1 route)	Std. [ns]	0.50	0.14	0.10	0.05	8.65	7.97
Same direction + LoS	Median [ns]	0.58	5.69	0.41	0.42	38.44	47.37
(8 routes)	Std. [ns]	0.09	0.13	0.08	0.09	15.52	31.38
Same direction + NLoS	Median [ns]	0.35	5.81	0.51	0.65	21.43	18.19
(7 routes)	Std. [ns]	0.08	0.11	0.08	0.08	14.63	16.99

Table C.3: Rx antennas located at the backside of the array.

		$i=1$			$i=2$		
		$\widehat{\omega}_1$	$\widehat{\mu}_1$	$\widehat{\sigma}_1$	$\widehat{\omega}_2$	$\widehat{\mu}_2$	$\widehat{\sigma}_2$
Underground parkings	Median [ns]	0.33	16.93	10.62	0.67	58.58	38.79
(3 routes)	Std. [ns]	0.25	12.45	16.44	0.25	16.80	10.39
Road crossings	Median [ns]	0.64	5.88	0.50	0.36	22.14	17.72
(2 routes)	Std. [ns]	0.08	0.11	0.08	0.08	7.78	14.30
Urban environment	Median [ns]	0.37	11.42	6.31	0.63	84.93	67.38
(2 routes)	Std. [ns]	0.15	13.41	20.31	0.15	25.30	22.23
Opposite directions	Median [ns]	0.52	6.32	0.70	0.47	31.54	27.33
(3 routes)	Std. [ns]	0.08	0.06	0.03	0.08	7.10	10.16
Different directions	Median [ns]	0.24	6.02	0.54	0.76	67.66	51.61
(1 route)	Std. [ns]	0.08	0.11	0.03	0.08	9.87	10.04
Static-to-mobile	Median [ns]	0.33	6.13	0.65	0.67	42.11	34.07
(1 route)	Std. [ns]	0.03	0.09	0.08	0.03	6.00	5.76
Same direction + LoS	Median [ns]	0.42	5.59	0.32	0.58	60.08	88.76
(8 routes)	Std. [ns]	0.12	0.14	0.10	0.12	22.72	36.49
Same direction + NLoS	Median [ns]	0.30	5.81	0.49	0.70	53.53	48.27
(7 routes)	Std. [ns]	0.06	0.07	0.04	0.06	17.91	19.67

Publications

Journals:

- O. Renaudin and C. Oestges, "Analysis of inter-tap correlation for measured mobile radio channels at 1.9 GHz," *Electronics Letters*, vol. 44, no. 16, pp. 945 – 947, July 2008
- O. Renaudin, V. M. Kolmonen, P. Vainikainen, and C. Oestges, "Non-stationary narrowband MIMO inter-vehicle channel characterization in the 5 GHz band," *IEEE Transactions on Vehicular Technology*, vol. 59, no. 4, pp. 2007 – 2015, May 2010
- ——, "Wideband measurement-based modeling of inter-vehicle channels in the 5 GHz band," accepted for publication

Conference proceedings:

- ——, "Wideband MIMO car-to-car radio channel measurements at 5.3 GHz," in *IEEE 68th Vehicular Technology Conference (VTC)*, Calgary (Canada), September 2008
- ——, "Car-to-car channel models based on wideband MIMO measurements at 5.3 GHz," in *9th European Conference on Antennas and Propagation (EUCAP)*, Berlin (Germany), March 2009
- ——, "Impact of the correlation matrix estimation accuracy on the computation of stationarity intervals," in *4th European Conference on Antennas and Propagation (EuCAP)*, Barcelona (Spain), April 2010
- ——, "About the multipath stationarity of car-to-car channels in the 5 GHz band," in *20th International Symposium on Electromagnetic Theory (EMTS 2010)*, Berlin (Germany), August 2010, pp. 1 – 4

Bibliography

[1] M. Peden, R. Scurfield, D. Sleet, D. Mohan, A. A. Hyder, E. Jarawan, and C. Mathers, *World report on road traffic injury prevention*, Geneva: World Health Organization (WHO), 2004.

[2] *Reducing transport greenhouse gas emissions - Trends and data*, Organisation for Economic Cooperation and Development (OECD), International Transport Forum, 2010.

[3] 802.11p, "Draft amendment to wireless LAN medium access control (MAC) and physical layer (PHY) specifications: Wireless access in vehicular environments," *IEEE P802.11p/D0.26*, January 2006.

[4] S. Cherkaoui, "Research on intelligents vehicles and ITS in the Canadian and North-American context," in *9th International Conference on Intelligent Transport Systems Telecommunications (ITST)*, Lille (France), October 2009.

[5] PReVent [Online], www.prevent-ip.org.

[6] Communications for eSafety [Online], www.comesafety.org.

[7] Car 2 Car Communication Consortium [Online], www.car-to-car.org.

[8] M. Fujise, "Communications policy and ITS in Japan," in *9th International Conference on Intelligent Transport Systems Telecommunications (ITST)*, Lille (France), October 2009.

[9] A. F. Molisch, F. Tufvesson, J. Karedal, and C. F. Mecklenbräuker, "A survey on vehicle-to-vehicle propagation channels," *IEEE Transactions on Wireless Communications*, vol. 16, no. 6, pp. 12 – 22, December 2009.

[10] C. F. Mecklenbräuker, A. F. Molisch, J. Karedal, F. Tufvesson, A. Paier, L. Bernadó, T. Zemen, O. Klemp, and N. Czink, "Vehicular channel characterization and its implications for wireless system design and performance," *Proceedings of the IEEE*, vol. 99, no. 7, pp. 1189 – 1212, July 2011.

[11] C. Oestges and B. Clerckx, *MIMO Wireless Communications: From Real-World Propagation to Space-Time Code Design*. Academic Press: Oxford, 2007.

[12] S. Takahashi, A. Kato, K. Sato, and M. Fujise, “Distance dependence of path loss for millimeter wave inter-vehicle communications,” in *IEEE 58th Vehicular Technology Conference (VTC)*, vol. 1, Orlando (Florida, USA), October 2003, pp. 26 – 30.

[13] A. Paier, J. Karedal, N. Czink, H. Hofstetter, C. Dumard, T. Zemen, F. Tufvesson, A. F. Molisch, and C. F. Mecklenbräuker, “Car-to-car radio channel measurements at 5 GHz: Pathloss, power-delay profile and delay-Doppler spectrum,” in *IEEE International Symposium on Wireless Communication Systems (ISWCS)*, Trondheim, (Norway), October 2007, pp. 224 – 228.

[14] J. Kunisch and J. Pamp, “Wideband car-to-car radio channel measurements and model at 5.9 GHz,” in *IEEE 68th Vehicular Technology Conference (VTC)*, Calgary (Canada), September 2008.

[15] J. Karedal, N. Czink, A. Paier, F. Tufvesson, and A. F. Molisch, “Path loss modeling for vehicle-to-vehicle communications,” *IEEE Transactions on Vehicular Technology*, vol. 60, no. 1, pp. 323 – 328, January 2011.

[16] L. Cheng, B. E. Henty, D. D. Stancil, F. Bai, and P. Mudalige, “Mobile vehicle-to-vehicle narrow-band channel measurement and characterization of the 5.9 GHz Dedicated Short Range Communication (DSRC) frequency band,” *IEEE Journal on Selected Areas in Communications*, vol. 25, no. 8, pp. 1501 – 1516, October 2007.

[17] P. Paschalidis, K. Mahler, A. Kortke, M. Peter, and W. Keusgen, “Pathloss and multipath power decay of the wideband car-to-car channel at 5.7 GHz,” in *IEEE 73rd Vehicular Technology Conference (VTC)*, Yokohama (Japan), May 2011, pp. 1 – 5.

[18] T. Abbas, F. Tufvesson, K. Sjöberg, and J. Karedal, “Shadow fading model for vehicle-to-vehicle network simulations, TD(12)05020,” in *Proceedings 5th IC1004 Management Committee Meeting*, Bristol (United Kingdom), October 2012.

[19] J. Maurer, T. Fügen, and W. Wiesbeck, “Narrow-band measurement and analysis of the inter-vehicle transmission channel at 5.2 GHz,” in *IEEE 55th Vehicular Technology Conference (VTC)*, vol. 3, Birmingham (Alabama, USA), 2002, pp. 1274 – 1278.

[20] J. Yin, G. Holland, T. ElBatt, F. Bai, and H. Krishnan, “DSRC channel fading analysis from empirical measurement,” in *1st International Conference on Communications and Networking in China (CHINACOM)*, Hangzhou (China), October 2006, pp. 1 – 5.

[21] D. W. Matolak, I. Sen, and W. Xiong, “Channel modeling for V2V communications,” in *3rd Annual International Conference on Mobile and Ubiquitous Systems: Networking & Services*, San Jose (California, USA), July 2006, pp. 1 – 7.

[22] D. W. Matolak, “Channel modeling for vehicle-to-vehicle communications,” *IEEE Communications Magazine*, vol. 46, no. 5, pp. 84 – 91, May 2008.

[23] L. Correia, *Mobile Broadband Multimedia Networks: Techniques, Models and Tools for 4G*. Academic Press, 2006.

[24] P. Almers, E. Bonek, A. Burr, N. Czink, M. Debbah, V. Degli-esposti, H. Hofstetter, P. Kyösti, D. Laurenson, G. Matz, A. F. Molisch, C. Oestges, and H. Özcelik, “Survey of channel and radio propagation models for wireless MIMO systems,” *EURASIP Journal on Wireless Communications and Networking*, 2007.

[25] P. Bello, “Characterization of randomly time-variant linear channels,” *IEEE Transactions on Communications Systems*, vol. 11, no. 4, pp. 360 – 393, December 1963.

[26] J. G. Proakis, *Digital communications*, 4th ed. New-York, NY: John Wiley & Sons, 2001.

[27] M. Herdin, “Non-stationary indoor MIMO channels,” Ph.D. dissertation, Technischen Universität Wien, 2004.

[28] A. Molisch, *Wireless Communications*. John Wiley & Sons, 2005.

[29] A. S. Akki and F. Haber, “A statistical model of mobile-to-mobile land communication channel,” *IEEE Transactions on Vehicular Technology*, vol. 35, no. 1, pp. 2 – 7, February 1986.

[30] A. S. Akki, “Statistical properties of mobile-to-mobile land communication channels,” *IEEE Transactions on Vehicular Technology*, vol. 43, no. 4, pp. 826 – 831, November 1994.

[31] C. Patel, G. L. Stüber, and T. G. Pratt, "Simulation of Rayleigh-faded mobile-to-mobile communication channels," *IEEE Transactions on Communications*, vol. 53, no. 11, pp. 1876 – 1884, November 2005.

[32] I. Tan, W. Tang, K. Laberteaux, and A. Bahai, "Measurement and analysis of wireless channel impairments in DSRC vehicular communications," in *IEEE International Conference on Communications (ICC)*, Beijing (China), May 2008, pp. 4882 – 4888.

[33] I. Sen and D. W. Matolak, "Vehicle-vehicle channel models for the 5 GHz band," *IEEE Transactions on Intelligent Transportation Systems*, vol. 9, no. 2, pp. 235 – 245, June 2008.

[34] T. Abbas, J. Karedal, F. Tufvesson, A. Paier, L. Bernadó, and A. F. Molisch, "Directional analysis of vehicle-to-vehicle propagation in different traffic environments," in *IEEE 73rd Vehicular Technology Conference (VTC)*, Budapest (Hungary), May 2011, pp. 1 – 5.

[35] A. F. Molisch, "Ultra-wide-band propagation channels," *Proceedings of the IEEE*, vol. 97, no. 2, pp. 353 – 371, February 2009.

[36] A. Gehring, M. Steinbauer, I. Gaspard, and M. Grigat, "Empirical channel stationarity in urban environments," in *4th European Personal Mobile Communications Conference (EPMCC)*, Vienna (Austria), February 2001.

[37] G. Matz, "Doubly underspread non-WSSUS channels: Analysis and estimation of channel statistics," in *4th IEEE Workshop on Signal Processing Advances in Wireless Communications (SPAWC)*, Rome (Italy), June 2003, pp. 190 – 194.

[38] ——, "On non-WSSUS wireless fading channels," *IEEE Transactions on Wireless Communications*, vol. 4, no. 5, pp. 2465 – 2478, September 2005.

[39] A. Paier, T. Zemen, L. Bernadó, G. Matz, J. Karedal, N. Czink, C. Dumard, F. Tufvesson, A. F. Molisch, and C. F. Mecklenbräuker, "Non-WSSUS vehicular channel characterization in highway and urban scenarios at 5.2 GHz using the local scattering function," in *International ITG Workshop on Smart Antennas (WSA)*, Darmstadt (Germany), February 2008, pp. 9 – 15.

[40] L. Bernadó, T. Zemen, A. Paier, G. Matz, J. Karedal, N. Czink, C. Dumard, F. Tufvesson, M. Hagenauer, A. F. Molisch, and C. F. Mecklenbräuker, "Non-WSSUS vehicular channel characterization at 5.2 GHz - Spectral divergence and time-variant coherence parameters," in *XXIX General Assembly of the International Union of Radio Science (URSI)*, Chicago, Illinois (USA), August 2008.

[41] L. Bernadó, T. Zemen, A. Paier, J. Karedal, and B. H. Fleury, "Parametrization of the local scattering function estimator for vehicular to vehicular channels," in *IEEE 70th Vehicular Technology Conference (VTC)*, Anchorage, Alaska (USA), September 2009.

[42] L. Bernadó, T. Zemen, F. Tufvesson, A. F. Molisch, and C. F. Mecklenbräuker, "The (in-)validity of the WSSUS assumption in vehicular radio channels," in *IEEE 70th Vehicular Technology Conference (VTC)*, Sydney, (Australia), September 2012.

[43] U. Chude-Okonkwo, R. Ngah, and T. A. Rahman, "Time-scale domain characterization of non-WSSUS wideband channels," *EURASIP Journal on Advances in Signal Processing*, vol. 2011, no. 1, p. 123, July 2011.

[44] I. Viering, H. Hofstetter, and W. Utschick, "Validity of spatial covariance matrices over time and frequency," in *IEEE Global Telecommunications Conference (GLOBECOM)*, vol. 1, Taipei (Taiwan), November 2002, pp. 851 – 855.

[45] T. J. Willink, "Wide-sense stationarity of mobile MIMO radio channels," *IEEE Transactions on Vehicular Technology*, vol. 57, no. 2, pp. 704 – 714, March 2008.

[46] D. Umansky and M. Pätzold, "Stationarity test for wireless communication channels," in *IEEE Global Telecommunications Conference (GLOBECOM)*, vol. 1, Honolulu (Hawaii, USA), December 2009, pp. 1 – 6.

[47] M. Herdin, N. Czink, H. Özcelik, and E. Bonek, "Correlation matrix distance, a meaningful measure for evaluation of non-stationary MIMO channels," in *IEEE 61st Vehicular Technology Conference (VTC)*, vol. 1, Stockholm (Sweden), 2005, pp. 136 – 140.

[48] M. Herdin and E. Bonek, "A MIMO correlation matrix based for characterizing non-stationarity," in *13th IST Mobile and Wireless Communications Summit*, Lyon (France), June 2004.

[49] H. J. Xiao and A. G. Burr, "Full channel correlation matrix of a time-variant wideband spatial channel model," in *IEEE International Symposium on Personal, Indoor and Mobile Radio Communications (PIMRC)*, Helsinki (Finland), September 2006, pp. 1 – 5.

[50] T. Kürner, D. Cichon, and W. Wiesbeck, "Concepts and results for 3D digital terrain-based wave propagation models: An overview," *IEEE Journal on Selected Areas in Communications*, vol. 11, no. 7, pp. 1002 – 1012, September 1993.

[51] J. Maurer, T. Schafer, and W. Wiesbeck, "A realistic description of the environment for inter-vehicle wave propagation modelling," in *IEEE 54th Vehicular Technology Conference (VTC)*, vol. 3, Atlantic City (New Jersey, USA), July 2001, pp. 1437 – 1441.

[52] J. Maurer, T. Fügen, T. Schafer, and W. Wiesbeck, "A new inter-vehicle communications (IVC) channel model," in *IEEE 60th Vehicular Technology Conference (VTC)*, vol. 1, Los Angeles (California, USA), September 2004, pp. 9 – 13.

[53] V. Degli-Esposti, D. Guiducci, A. de'Marsi, P. Azzi, and F. Fuschini, "An advanced field prediction model including diffuse scattering," *IEEE Transactions on Antennas and Propagation*, vol. 52, no. 7, pp. 1717 – 1728, July 2004.

[54] A. Thiel, O. Klemp, A. Paier, L. Bernadó, N. Czink, J. Karedal, and A. Kwoczek, "In-situ vehicular antenna integration and design aspects for vehicle-to-vehicle communications," in *4th European Conference on Antennas and Propagation (EuCAP)*, Barcelona (Spain), April 2010, pp. 1 – 5.

[55] L. Reichardt, T. Fügen, and T. Zwick, "Influence of antenna placement on car to car communication channel," in *9th European Conference on Antennas and Propagation EuCAP*, Berlin (Germany), March 2009.

[56] J. Pontes, L. Reichardt, and T. Zwick, "Investigation on antenna systems for car-to-car communication," *IEEE Journal on Selected Areas in Communications*, vol. 29, no. 1, pp. 7 – 14, January 2011.

[57] L. Reichardt, J. Maurer, T. Fügen, and T. Zwick, "Virtual Drive: A complete V2X communication and radars system simulator for optimization of multiple antenna systems," *Proceedings of the IEEE*, vol. 99, no. 7, pp. 1295 – 1310, July 2011.

[58] G. Acosta and M. A. Ingram, “Model development for the wideband expressway vehicle-to-vehicle 2.4 GHz channel,” in *IEEE Wireless Communications and Networking Conference (WCNC)*, vol. 3, Las Vegas (Nevada, USA), April 2006, pp. 1283 – 1288.

[59] G. Acosta-Marum and M. A. Ingram, “Six time- and frequency-selective empirical channel models for vehicular wireless LANs,” in *IEEE 66th Vehicular Technology Conference (VTC)*, Baltimore (Maryland, USA), September 2007.

[60] A. Paier, “The vehicular radio channel in the 5 GHz band,” Ph.D. dissertation, Technischen Universität Wien, 2010.

[61] D. W. Matolak, I. Sen, and W. Xiong, “The 5 GHz airport surface area channel - Part I: Measurement and modeling results for large airports,” *IEEE Transactions on Vehicular Technology*, vol. 57, no. 4, pp. 2014 – 2026, July 2008.

[62] G. Acosta-Marum and M. A. Ingram, “A BER-based partitioned model for a 2.4 GHz vehicle-to-vehicle expressway channel,” *Wireless Personal Communications*, vol. 37, pp. 421 – 443, May 2006.

[63] A. G. Zajić and G. L. Stüber, “Space-time correlated mobile-to-mobile channels: Modelling and simulation,” *IEEE Transactions on Vehicular Technology*, vol. 57, no. 2, pp. 715 – 726, March 2008.

[64] X. Cheng, C. X. Wang, D. I. Laurenson, S. Salous, and A. V. Vasilakos, “An adaptive geometry-based stochastic model for non-isotropic MIMO mobile-to-mobile channel,” *IEEE Transactions on Wireless Communications*, vol. 8, no. 9, pp. 4824 – 4835, September 2009.

[65] T. M. Wu and C. M. Kuo, “3-D space-time-frequency correlation functions of mobile-to-mobile radio channels,” in *IEEE 65th Vehicular Technology Conference (VTC)*, Dublin (Ireland), April 2007, pp. 334 – 338.

[66] A. G. Zajić, G. L. Stüber, T. G. Pratt, and S. T. Nguyen, “Statistical modeling with experimental verification for wideband MIMO mobile-to-mobile channels in urban environments,” in *IEEE International Conference on Telecommunications (ICT)*, Lyon (France), June 2008, pp. 1 – 6.

[67] ——, “Statistical modeling with experimental verification for wideband MIMO mobile-to-mobile channels in highway environments,” in *IEEE*

19th International Symposium on Personal, Indoor and Mobile Radio Communications (PIMRC), Cannes (France), September 2008, pp. 1 – 5.

[68] ——, “Envelope level crossing rate and average fade duration in mobile-to-mobile Ricean fading channels,” in *IEEE International Conference on Communications (ICC)*, Beijing (China), May 2008, pp. 1 – 5.

[69] M. Pätzold, B. Hogstad, and N. Youssef, “Modeling, analysis, and simulation of MIMO mobile-to-mobile fading channels,” *IEEE Transactions on Wireless Communications*, vol. 7, no. 2, pp. 510 – 520, February 2008.

[70] A. G. Zajić, G. L. Stüber, T. G. Pratt, and S. T. Nguyen, “Wideband MIMO mobile-to-mobile channels: Geometry-based statistical modeling with experimental validation,” *IEEE Transactions on Vehicular Technology*, vol. 58, no. 2, pp. 517 – 534, February 2009.

[71] A. G. Zajić and G. L. Stüber, “Influence of 3-D spatial correlation on the capacity of MIMO mobile-to-mobile channels,” in *IEEE 65th Vehicular Technology Conference (VTC)*, Dublin (Ireland), April 2007, pp. 461 – 465.

[72] A. Chelli and M. Pätzold, “The impact of fixed and moving scatterers on the statistics of MIMO vehicle-to-vehicle channels,” in *IEEE 73rd Vehicular Technology Conference (VTC)*, May 2009, pp. 1 – 6.

[73] J. Karedal, F. Tufvesson, N. Czink, A. Paier, C. Dumard, T. Zemen, C. F. Mecklenbräuker, and A. F. Molisch, “A geometry-based stochastic MIMO model for vehicle-to-vehicle communications,” *IEEE Transactions on Wireless Communications*, vol. 8, no. 7, pp. 3646 – 3657, July 2009.

[74] J. S. Davis and J. P. M. G. Linnartz, “Vehicle to vehicle RF propagation measurements,” in *28th Asilomar Conference on Signals, Systems and Computers*, vol. 1, Pacific Grove (California, USA), October 1994, pp. 470 – 474.

[75] R. J. Punnoose, P. V. Nikitin, J. Broch, and D. D. Stancil, “Optimizing wireless network protocols using real-time predictive propagation modeling,” in *IEEE Radio and Wireless Conference (RAWCON)*, Denver (Colorado, USA), August 1999, pp. 39 – 44.

[76] F. M. Pallares, F. J. P. Juan, and L. Juan-Llacer, “Analysis of path loss and delay spread at 900 MHz and 2.1 GHz while entering tunnels,” *IEEE Transactions on Vehicular Technology*, vol. 50, no. 3, pp. 767 – 776, May 2001.

[77] G. Acosta, K. Tokuda, and M. A. Ingram, “Measured joint Doppler-delay power profiles for vehicle-to-vehicle communications at 2.4 GHz,” in *IEEE Global Telecommunications Conference (GLOBECOM)*, vol. 6, Miami (Florida, USA), November 2004, pp. 3813 – 3817.

[78] D. W. Matolak, I. Sen, W. Xiong, and N. T. Yaskoff, “5 GHz wireless channel characterization for vehicle to vehicle communications,” in *IEEE Military Communications Conference (MILCOM)*, vol. 5, Atlantic City (New Jersey, USA), 2005, pp. 3016 – 3022.

[79] L. Cheng, B. E. Henty, D. D. Stancil, and F. Bai, “Doppler component analysis of the suburban vehicle-to-vehicle DSRC propagation channel at 5.9 GHz,” in *IEEE Radio and Wireless Symposium*, January 2008, pp. 343 – 346.

[80] P. Paschalidis, M. Wisotzki, A. Kortke, W. Keusgen, and M. Peter, “A wideband channel sounder for car-to-car radio channel measurements at 5.7 GHz and results for an urban scenario,” in *IEEE 68th Vehicular Technology Conference (VTC)*, Calgary (Canada), September 2008.

[81] A. Paier, J. Karedal, N. Czink, H. Hofstetter, C. Dumard, T. Zemen, F. Tufvesson, C. F. Mecklenbräuker, and A. F. Molisch, “First results from car-to-car and car-to-infrastructure radio channel measurements at 5.2 GHz,” in *IEEE 18th International Symposium on Personal, Indoor and Mobile Radio Communications (PIMRC)*, Athens, (Greece), September 2007, pp. 1 – 5.

[82] T. W. C. Brown, P. C. F. Eggers, K. Olesen, and G. F. Pedersen, “Artificial wideband multi-user channels for rural high speed vehicle-to-vehicle links,” *IEEE Journal on Selected Areas in Communications*, vol. 29, no. 1, pp. 29 – 36, January 2011.

[83] A. Paier, J. Karedal, N. Czink, C. Dumard, T. Zemen, F. Tufvesson, A. F. Molisch, and C. F. Mecklenbräuker, “Characterization of vehicle-to-vehicle radio channels from measurements at 5.2 GHz,” *Wireless Personal Communications*, vol. 50, no. 1, pp. 19 – 32, January 2009.

[84] P. C. F. Eggers, T. W. C. Brown, K. Olesen, and G. F. Pedersen, "Assessment of capacity support and scattering in experimental high speed vehicle to vehicle MIMO links," in *IEEE 65th Vehicular Technology Conference (VTC)*, Dublin (Ireland), April 2007, pp. 466 – 470.

[85] S. Kaul, K. Ramachandran, P. Shankar, S. Oh, M. Gruteser, I. Seskar, and T. Nadeem, "Effect of antenna placement and diversity on vehicular network communications," in *IEEE 4th Communications Society Conference on Sensor, Mesh and Ad Hoc Communications and Networks (SECON)*, vol. 1, San Diego (California, USA), June 2007, pp. 112 – 121.

[86] J. Karedal, F. Tufvesson, T. Abbas, O. Klemp, A. Paier, L. Bernadó, and A. F. Molisch, "Radio channel measurements at street intersections for vehicle-to-vehicle safety applications," in *IEEE 71st Conference on Vehicular Technology (VTC)*, Taipei (Taiwan), May 2010, pp. 1 – 5.

[87] L. Bernadó, A. Roma, A. Paier, T. Zemen, N. Czink, J. Karedal, A. Thiel, O. Klemp, F. Tufvesson, A. F. Molisch, and C. F. Mecklenbräuker, "In-tunnel vehicular radio channel characterization," in *IEEE 73rd Vehicular Technology Conference (VTC)*, May 2011, pp. 1 – 5.

[88] L. Bernadó, T. Zemen, J. Karedal, A. Paier, A. Thiel, O. Klemp, N. Czink, F. Tufvesson, A. F. Molisch, and C. F. Mecklenbräuker, "Time-, frequency-, and space-varying K-factor analysis of V2V street crossing radio channels," in *IEEE International Symposium on Personal, Indoor and Mobile Radio Communications (PIMRC)*, September 2010.

[89] H. Zhiyi, C. Wei, Z. Wei, M. Pätzold, and A. Chelli, "Modelling of MIMO vehicle-to-vehicle fading channels in T-junction scattering environments," in *3rd European Conference on Antennas and Propagation (EuCAP)*, Berlin (Germany), March 2009.

[90] A. Paier, L. Bernadó, J. Karedal, O. Klemp, and A. Kwoczek, "Overview of vehicle-to-vehicle radio channel measurements for collision avoidance applications," in *IEEE 71st Vehicular Technology Conference (VTC)*, Taipei (Taiwan), May 2010, pp. 1 – 5.

[91] V. M. Kolmonen, J. Kivinen, L. Vuokko, and P. Vainikainen, "5.3-GHz MIMO radio channel sounder," *IEEE Transactions on Instrumentation and Measurement*, vol. 55, no. 4, pp. 1263–1269, August 2006.

[92] Z. Zhou, B. Vucetic, M. Dohler, and Y. H. Li, "MIMO systems with adaptive modulation," *IEEE Transactions on Vehicular Technology*, vol. 54, no. 5, pp. 1828 – 1842, September 2005.

[93] Y. Ko and C. Tepedelenlioglu, "Orthogonal space-time block coded rate-adaptive modulation with outdated feedback," *IEEE Transactions on Wireless Communications*, vol. 5, no. 2, pp. 290 – 295, February 2006.

[94] H. Zhang, S. Wei, G. Ananthaswamy, and D. L. Goeckel, "Adaptive signaling based on statistical characterizations of outdated feedback in wireless communications," *Proceedings of the IEEE*, vol. 85, no. 12, pp. 2337 – 2353, December 2007.

[95] J. A. Gubner, *Probability and random processes for electrical and computer engineers*. Academic Press: Cambridge, 2006.

[96] L. Bernadó, "Non-stationarity in vehicular wireless channels," Ph.D. dissertation, Technischen Universität Wien, 2012.

[97] W. C. Y. Lee, "Estimate of local average power of a mobile radio channel," *IEEE Transactions on Vehicular Technology*, vol. 34, no. 1, pp. 22– 27, February 1985.

[98] A. F. Molisch and M. Steinbauer, "Condensed parameters for characterizing wideband mobile radio channels," *International Journal of Wireless Information Networks*, vol. 6, no. 3, pp. 133 – 154, July 1999.

[99] A. F. Molisch, "A generic channel model for MIMO wireless propagation channels in macro- and microcells," *IEEE Transactions on Signal Processing*, vol. 52, no. 1, pp. 61 – 71, January 2004.

[100] R. J. M. Cramer, R. A. Scholtz, and M. Z. Win, "Evaluation of an ultra-wide-band propagation channel," *IEEE Transactions on Antennas and Propagation*, vol. 50, no. 5, pp. 541 – 550, May 2002.

[101] T. Santos, J. Karedal, P. Almers, F. Tufvesson, and A. F. Molisch, "Modeling the ultra-wideband outdoor channel: Measurements and parameter extraction method," *IEEE Transactions on Wireless Communications*, vol. 9, no. 1, pp. 282 – 290, January 2010.

[102] A. Richter, "Estimation of radio channel parameters: Models and algorithms," Ph.D. dissertation, Technischen Universität Ilmenau, 2005.

[103] N. Czink, A. Richter, E. Bonek, J. P. Nuutinen, and J. Ylitalo, “Including diffuse multipath parameters in MIMO channel models,” in *IEEE 66th Vehicular Technology Conference (VTC)*, September 2007, pp. 874 – 878.

[104] O. Renaudin and C. Oestges, “Analysis of inter-tap correlation for measured mobile radio channels at 1.9 GHz,” *Electronics Letters*, vol. 44, no. 16, pp. 945 – 947, July 2008.

[105] O. Renaudin, V. M. Kolmonen, P. Vainikainen, and C. Oestges, “Non-stationary narrowband MIMO inter-vehicle channel characterization in the 5 GHz band,” *IEEE Transactions on Vehicular Technology*, vol. 59, no. 4, pp. 2007 – 2015, May 2010.

[106] ——, “Wideband measurement-based modeling of inter-vehicle channels in the 5 GHz band,” accepted for publication.

[107] ——, “Wideband MIMO car-to-car radio channel measurements at 5.3 GHz,” in *IEEE 68th Vehicular Technology Conference (VTC)*, Calgary (Canada), September 2008.

[108] ——, “Car-to-car channel models based on wideband MIMO measurements at 5.3 GHz,” in *9th European Conference on Antennas and Propagation (EUCAP)*, Berlin (Germany), March 2009.

[109] ——, “Impact of the correlation matrix estimation accuracy on the computation of stationarity intervals,” in *4th European Conference on Antennas and Propagation (EuCAP)*, Barcelona (Spain), April 2010.

[110] ——, “About the multipath stationarity of car-to-car channels in the 5 GHz band,” in *20th International Symposium on Electromagnetic Theory (EMTS 2010)*, Berlin (Germany), August 2010, pp. 1 – 4.